Interim + final report WP2: Catalysts characterization

Table of Contents

1.1 SEM, EDX characteristics of Ni deposits obtained in Ethaline-based electrolyte
1.2 Surface morphology, topography and chemical composition of Ni/MoS_2 43
coatings deposited from DES-based electrolyte 43
1.3 Characterization of MoFeNiP catalysts 63
1.4 SEM and EDX characterization of Ni/MXene composite coatings 67
1.5 Morphological and elemental analysis of $Ni_{1-x}Co_xS$ catalysts 102

1.1 SEM, EDX characteristics of Ni deposits obtained in Ethaline-based electrolyte

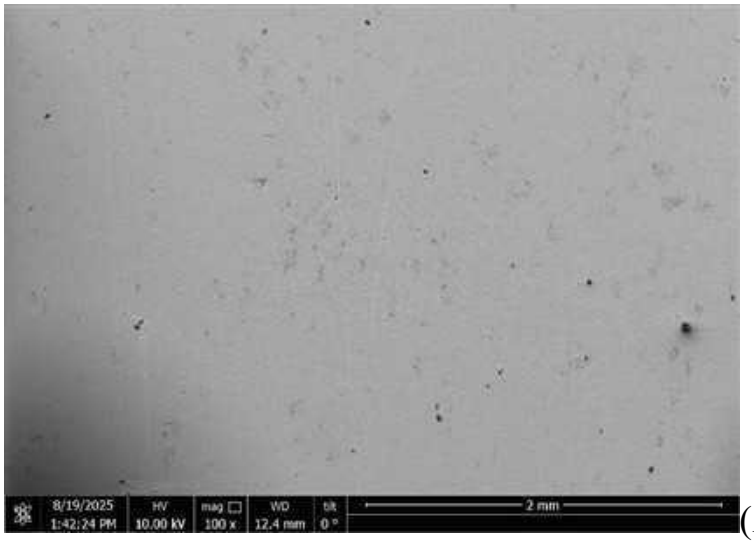
In the development of catalysts for efficient green hydrogen production, it is essential to design catalytically active surfaces with a high surface area while ensuring long-term stability under operating conditions. Therefore, surface morphology, topography, and chemical composition are key parameters for evaluating catalyst performance and durability. A series of Ni deposits was examined to assess the influence of different deposition conditions on their resulting properties. The specific deposition conditions used for each sample are summarized in Table 1.

Table 1. Experimental conditions for Ni electrodeposition from an Ethaline-based electrolyte.

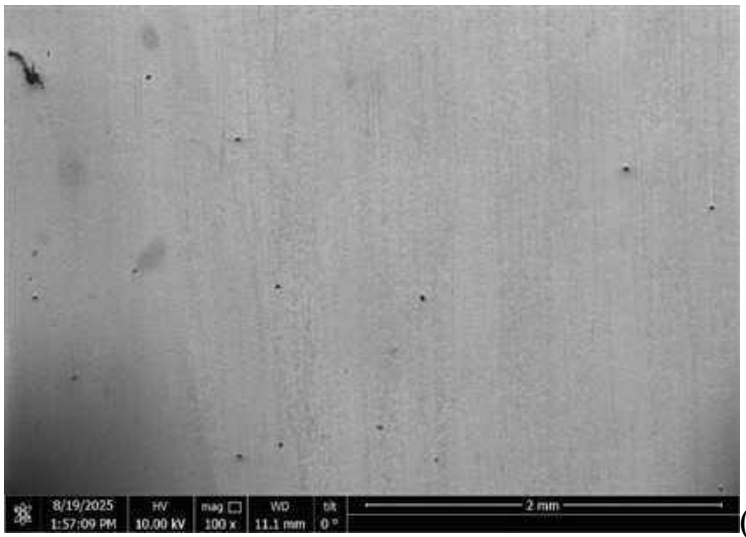
Sample	j, mA/cm^2	t, ^{o}C	τ, min
1	2	40	20
2	5		
3	10		
4	15		
5	20		
6	30		

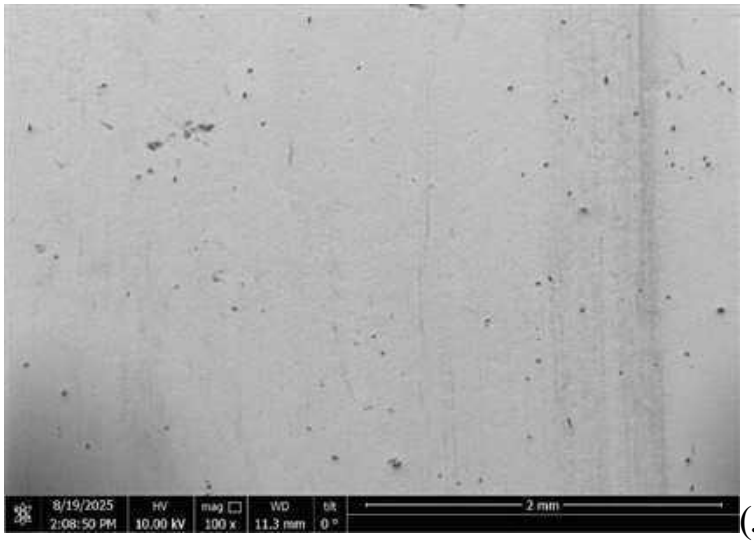
7	50		
8	5	50	
9	10		
10	15		
11	20		
12	5	60	
13	10		
14	15		
15	20		
16	5	30	
17	10		
18	15		
19	20		

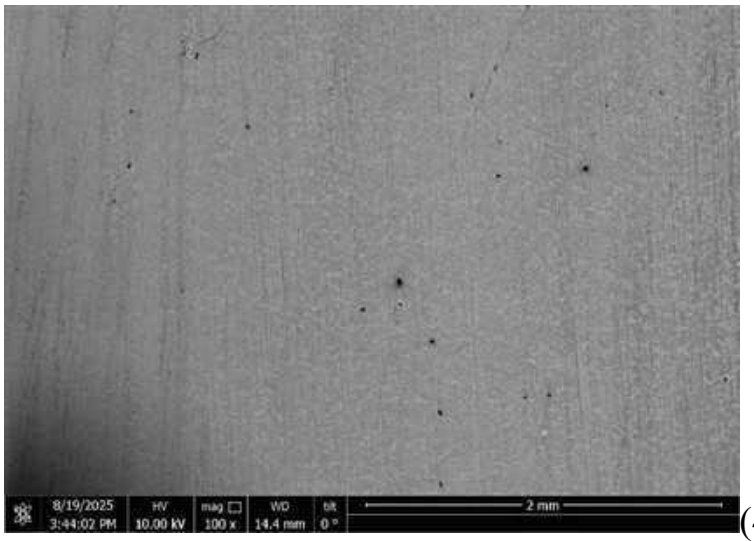
The surfaces of Ni deposits obtained from the Ethaline-based electrolyte were characterized using SEM and EDX techniques. For general observations of Ni coatings, a low magnification (100×, Figure 1) was used, while higher magnifications were utilized to examine micro- and nano-scale surface textures in more detail (Figures 2 and 3).

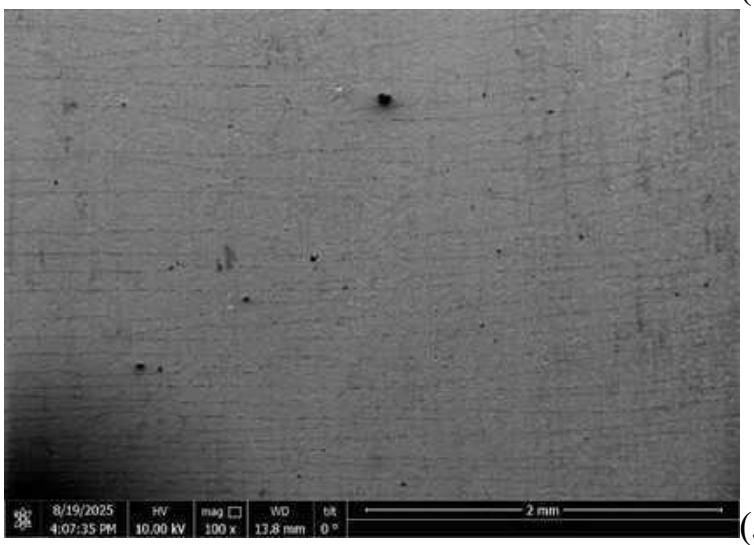


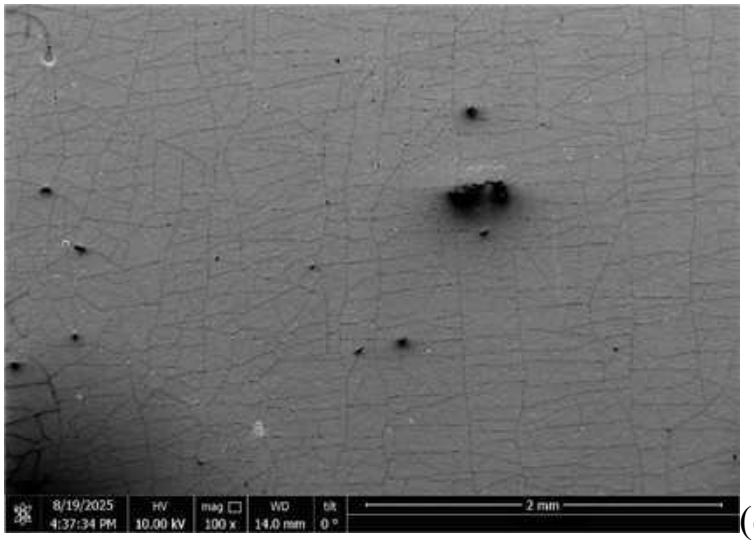
(***1***)

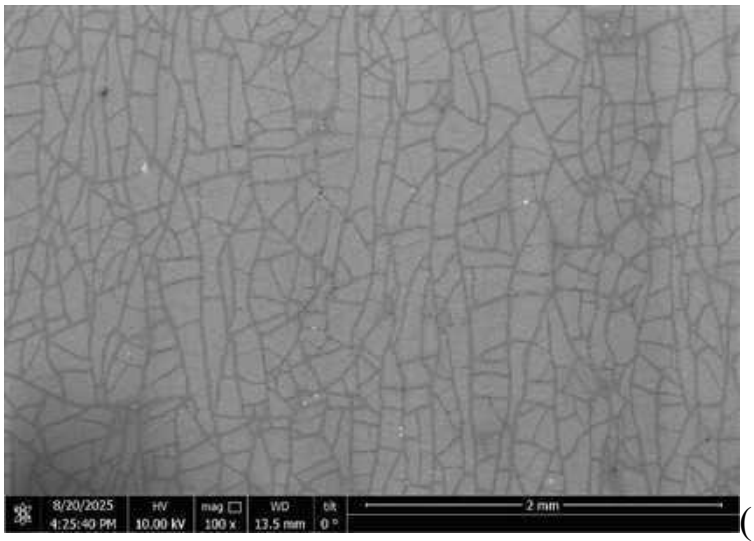

8/19/2025
1:57:09 PM
HV
10.00 kV
mag
100 x
WD
11.1 mm
tilt
0 °
2 mm
(*2*)

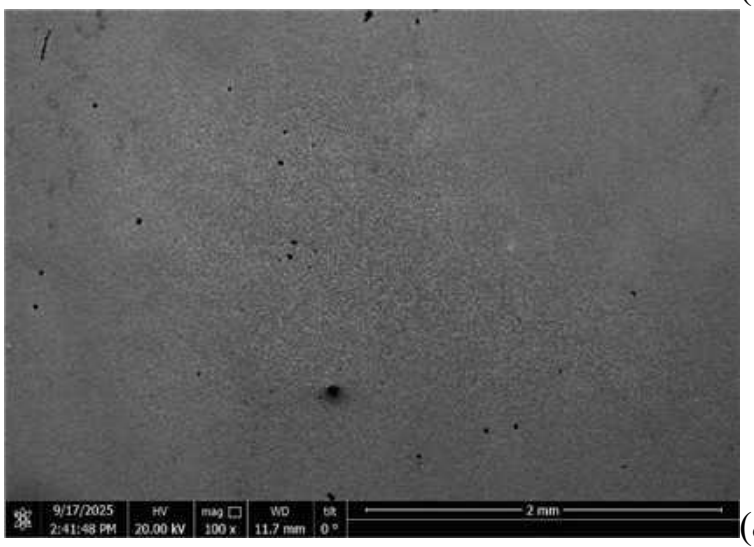

8/19/2025
2:08:50 PM
HV
10.00 kV
mag
100 x
WD
11.3 mm
tilt
0 °
2 mm
(*3*)

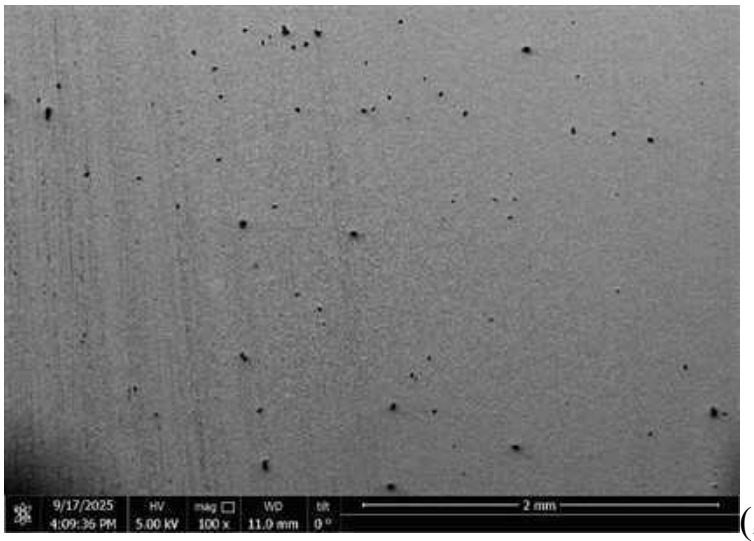

8/19/2025
3:44:02 PM
HV
10.00 kV
mag
100 x
WD
14.4 mm
tilt
0 °
2 mm
(*4*)

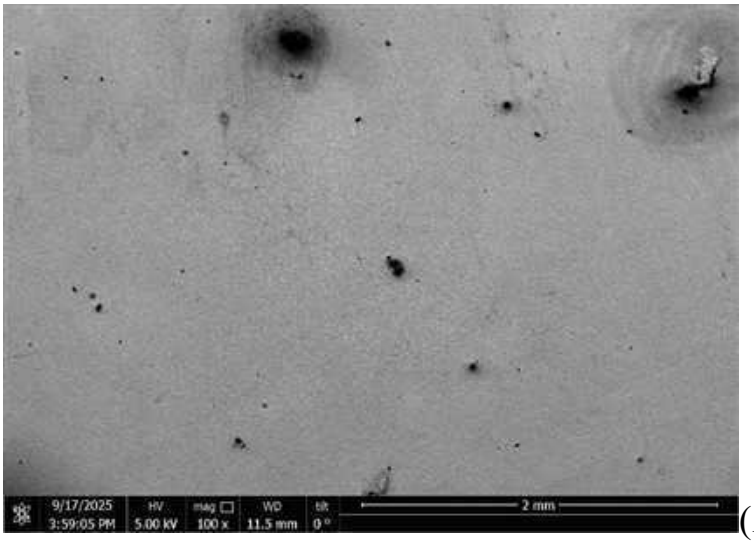

8/19/2025
4:07:35 PM
HV
10.00 kV
mag
100 x
WD
13.8 mm
tilt
0 °
2 mm
(*5*)

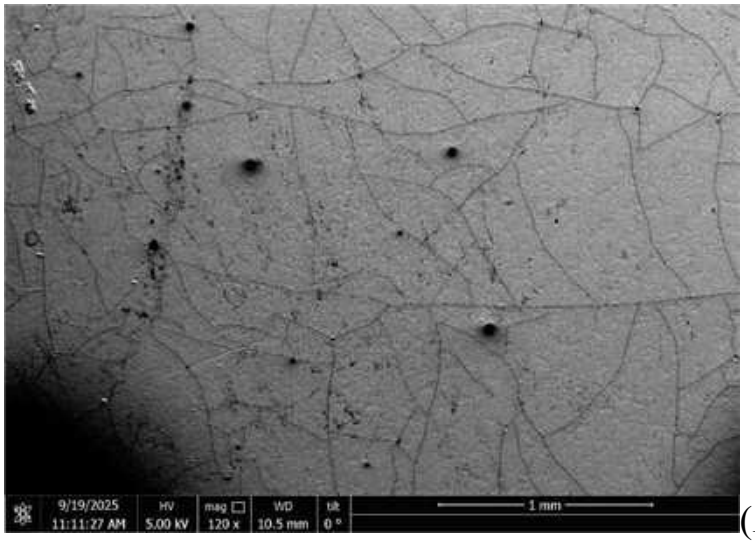

8/19/2025
4:37:34 PM
HV
10.00 kV
mag
100 x
WD
14.0 mm
tilt
0 °
2 mm
(*6*)

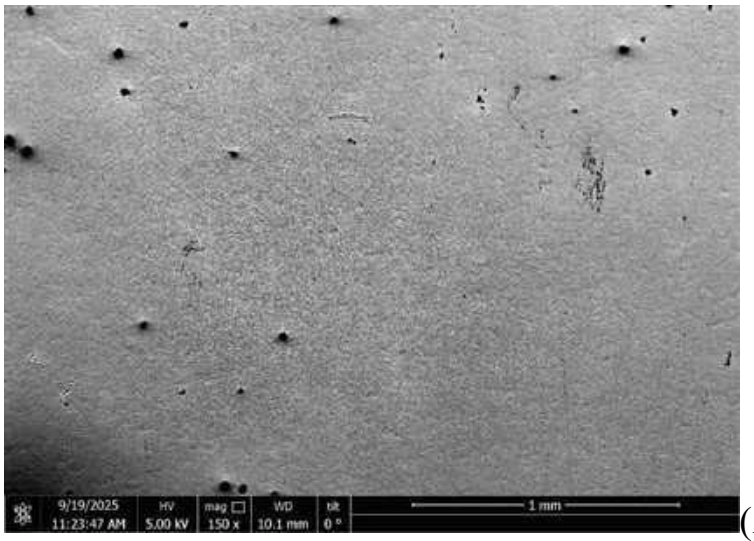

8/20/2025
4:25:40 PM
HV
10.00 kV
mag
100 x
WD
13.5 mm
tilt
0 °
2 mm
(*7*)

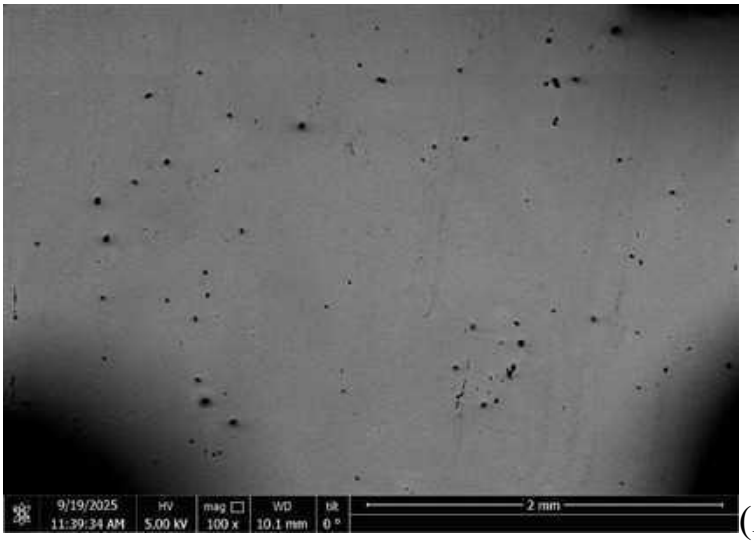

9/17/2025
2:41:48 PM
HV
20.00 kV
mag
100 x
WD
11.7 mm
tilt
0 °
2 mm
(***8***)

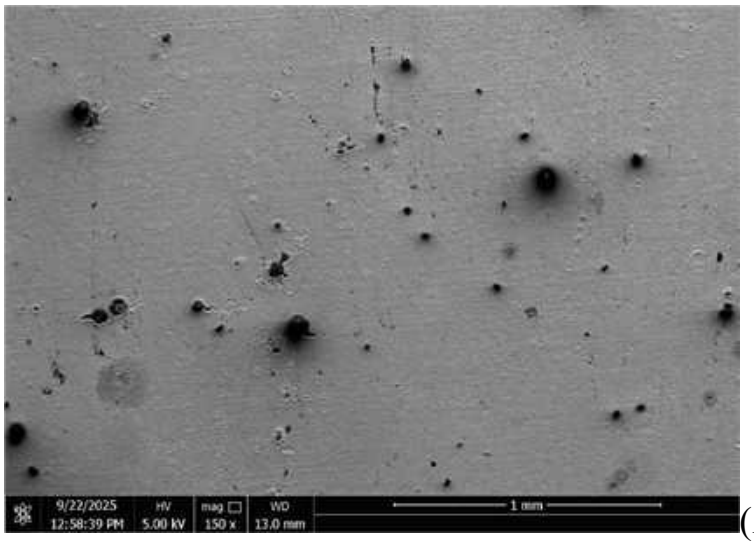

9/17/2025
4:09:36 PM
HV
5.00 kV
mag
100 x
WD
11.0 mm
tilt
0 °
2 mm
(***9***)

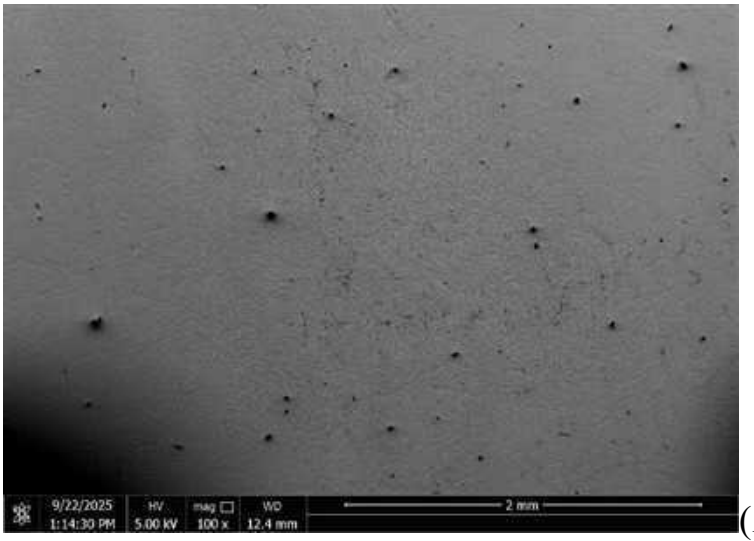

9/17/2025
3:59:05 PM
HV
5.00 kV
mag
100 x
WD
11.5 mm
tilt
0 °
2 mm
(***10***)

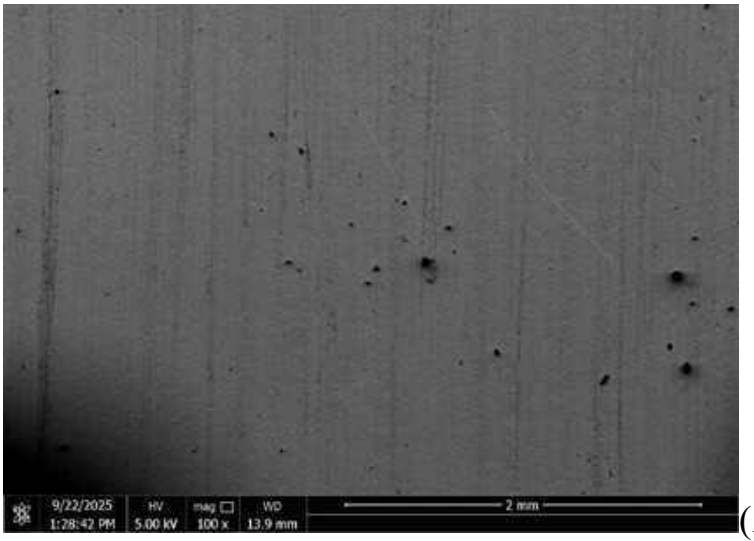

9/19/2025
11:11:27 AM
HV
5.00 kV
mag
120 x
WD
10.5 mm
tilt
0 °
1 mm
(***11***)*

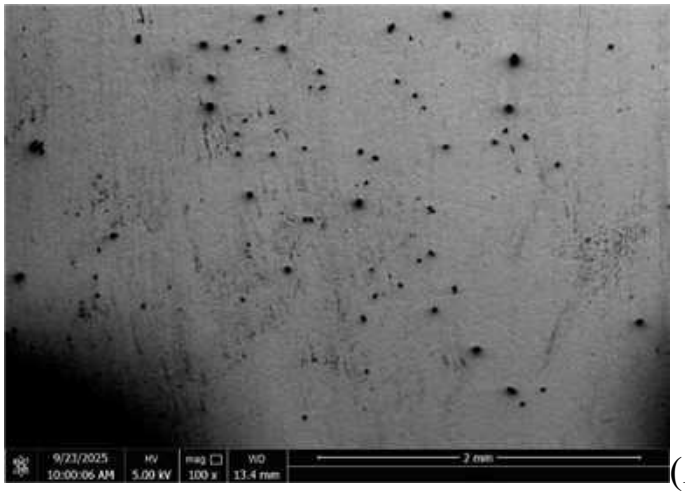

9/19/2025
11:23:47 AM
HV
5.00 kV
mag
150 x
WD
10.1 mm
tilt
0 °
1 mm
(*12*)**

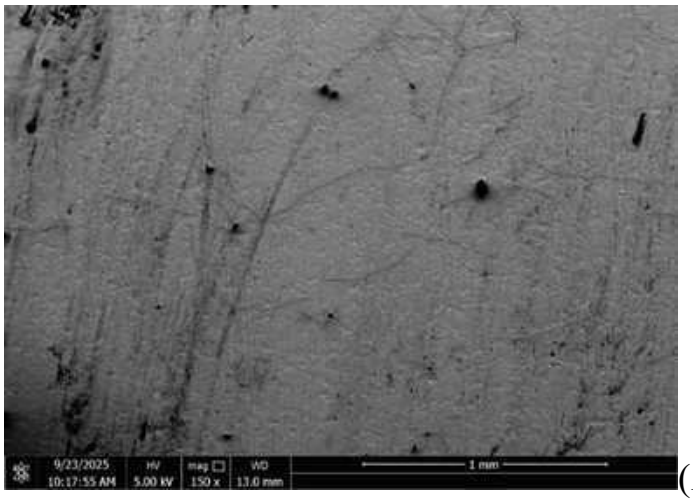

9/19/2025
11:39:34 AM
HV
5.00 kV
mag
100 x
WD
10.1 mm
tilt
0 °
2 mm
(*13*)


9/22/2025
12:58:39 PM
HV
5.00 kV
mag
150 x
WD
13.0 mm
1 mm
(*14*)**


9/22/2025
1:14:30 PM
HV
5.00 kV
mag
100 x
WD
12.4 mm
2 mm
(*15*)


9/22/2025
1:28:42 PM
HV
5.00 kV
mag
100 x
WD
13.9 mm
2 mm
(*16*)


9/23/2025
10:00:06 AM
HV
5.00 kV
mag
100 x
WD
13.4 mm
2 mm
(***17***)


9/23/2025
10:17:55 AM
HV
5.00 kV
mag
150 x
WD
13.0 mm
1 mm
(***18***)**

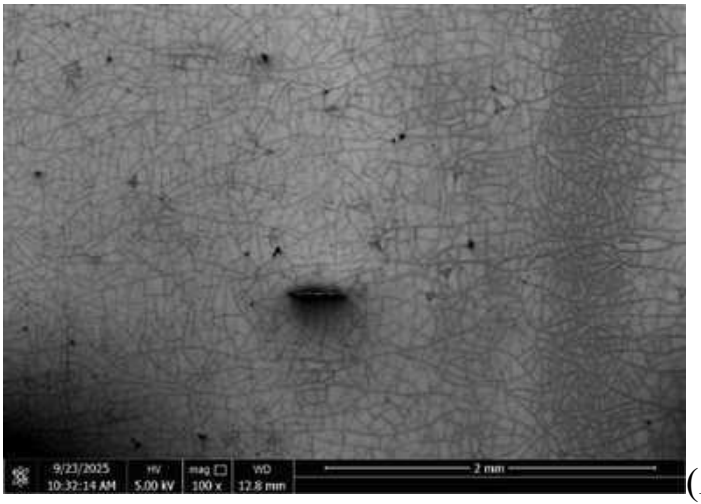

9/23/2025
10:32:14 AM
HV
5.00 kV
mag
100 x
WD
12.8 mm
2 mm
(***19***)

Figure 1. SEM images of Ni coatings electrodeposited from the Ethaline-based electrolyte under various conditions. Magnification: 100×; scale bar: 2 mm. *Magnification: 120×; scale bar: 1 mm. **Magnification: 150×; scale bar: 1 mm. Sample numbers correspond to the electrodeposition parameters listed in Table 1.

The obtained results revealed that increasing the deposition current density and coating thickness led to the formation of surface cracks, which can be attributed to the well-known internal stresses that develop in electrodeposited Ni layers. These stresses arise from factors such as hydrogen incorporation, lattice mismatch, and rapid grain growth during deposition.

It is noteworthy that at the lowest investigated temperature (30 °C), cracks appeared at relatively low current densities, i.e., at or above 15 mA cm^{-2}. As the temperature increased, the onset of cracking shifted to higher current densities. For example, at 40 °C and 50 °C, surface cracking was first observed at 20 mA cm^{-2}. Interestingly, at 60 °C, no cracks were detected across the entire range of applied current densities, indicating that elevated temperature reduces internal stress formation and improves coating ductility.

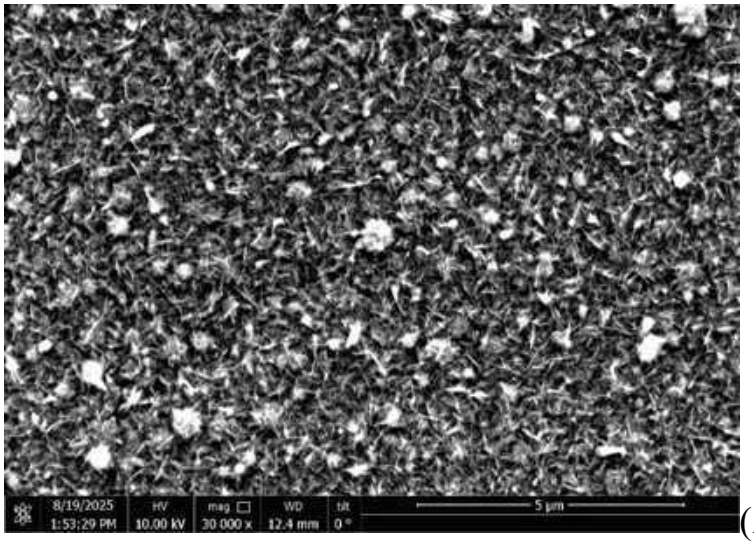
Admit that the most homogeneous and compact Ni surfaces were obtained under moderate deposition conditions, specifically, at temperatures of 40–50 °C and current densities of 10–15 mA cm^{-2}, where the balance between nucleation rate, grain growth, and stress relaxation appears optimal.

Figures 2 and 3 clearly reveal the presence of micro- and nano-scale structures on the surfaces of Ni coatings deposited from Ethaline-based electrolytes. It is evident that both the electrolyte temperature and deposition current density significantly influence surface morphology and topography.

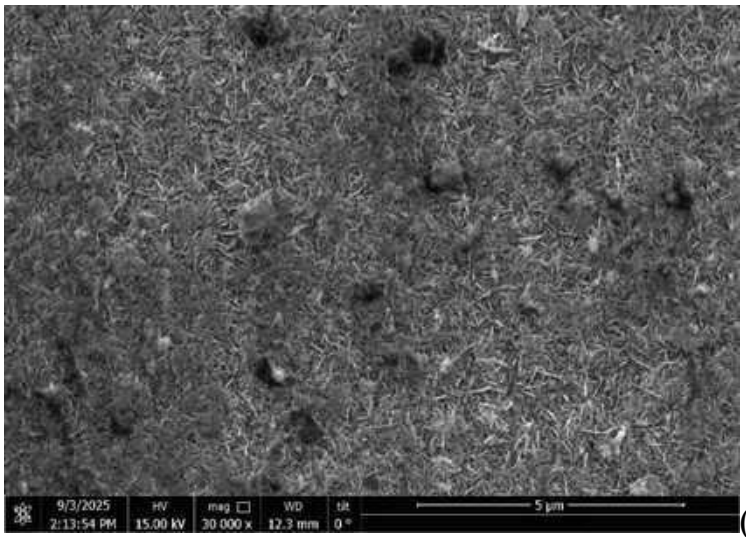
At low to moderate temperatures (30 and 40 °C), the coating surfaces exhibit a homogeneous lamellar texture composed of nano-sized lamellae. As the temperature

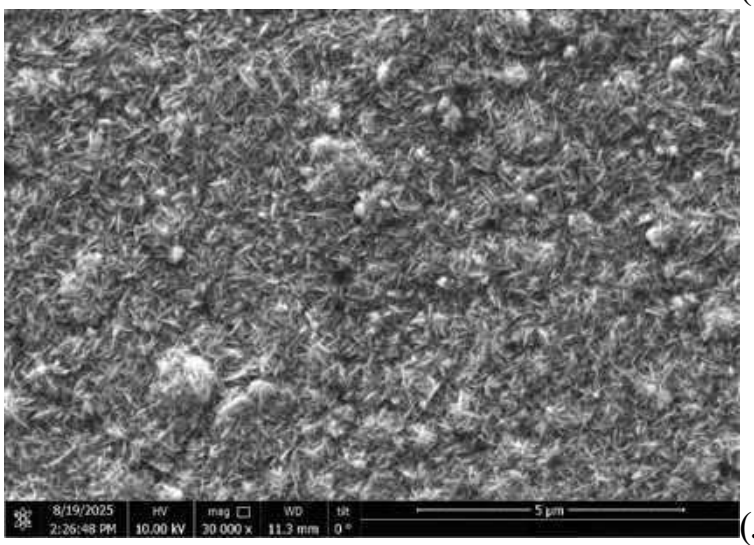
increases (50 and 60 °C), the surface morphology changes to feature micro-sized hemispherical hills. These effects are particularly pronounced at low current densities (5–10 mA cm^{-2}), suggesting that lower nucleation rates combined with higher atomic mobility at elevated temperatures favor the growth of larger microstructures.

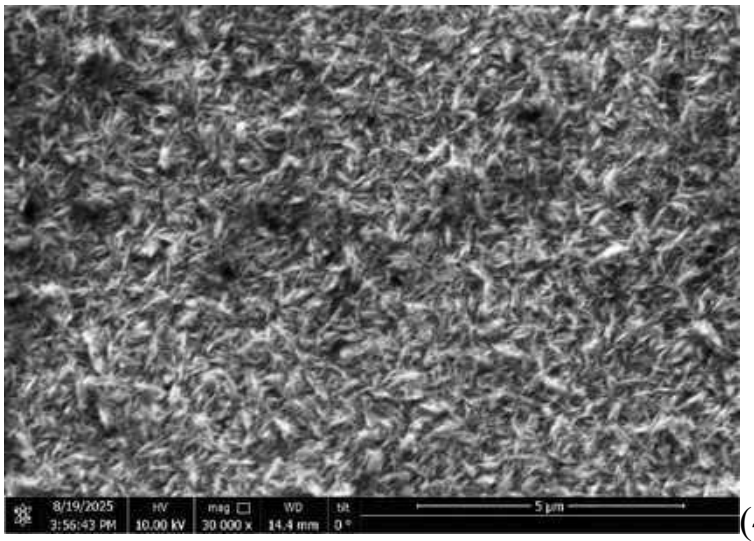
By varying the deposition current density and electrolyte temperature, it is possible to tailor the surface structure, producing either purely nano-textured coatings or combined micro–nano-textured surfaces. Such controlled texturing is of great interest for catalytic applications, as both surface area and hierarchical structures can significantly enhance catalytic activity and mass transport during reactions.

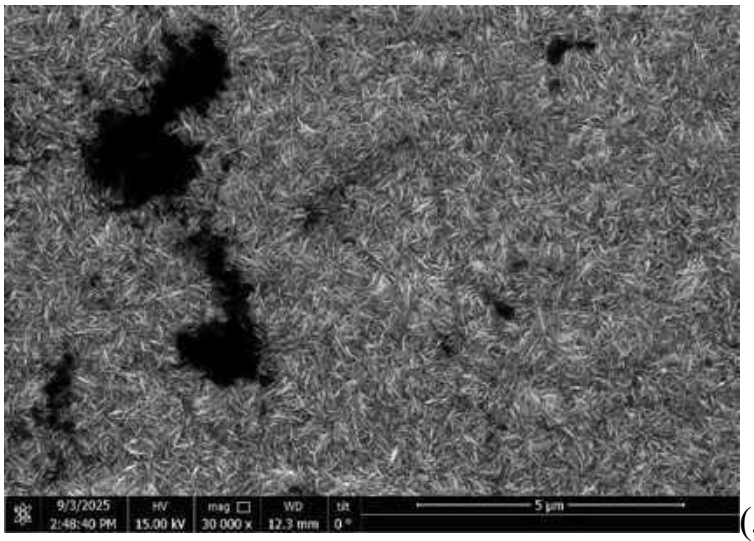


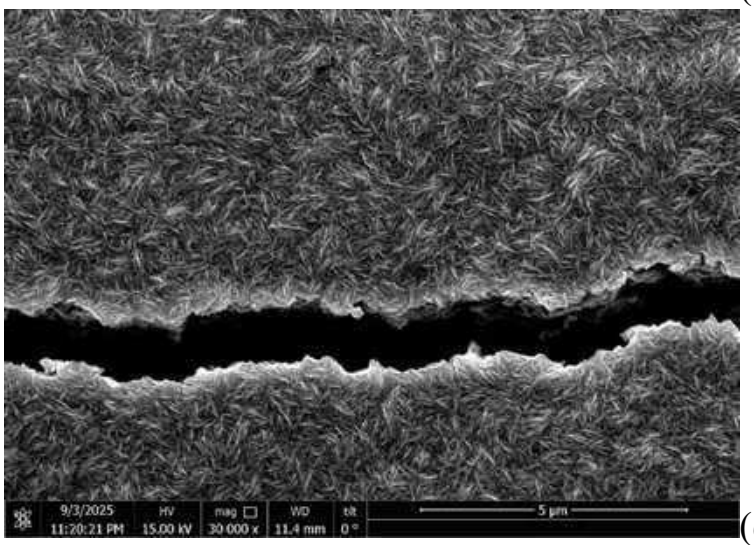
(***1***)

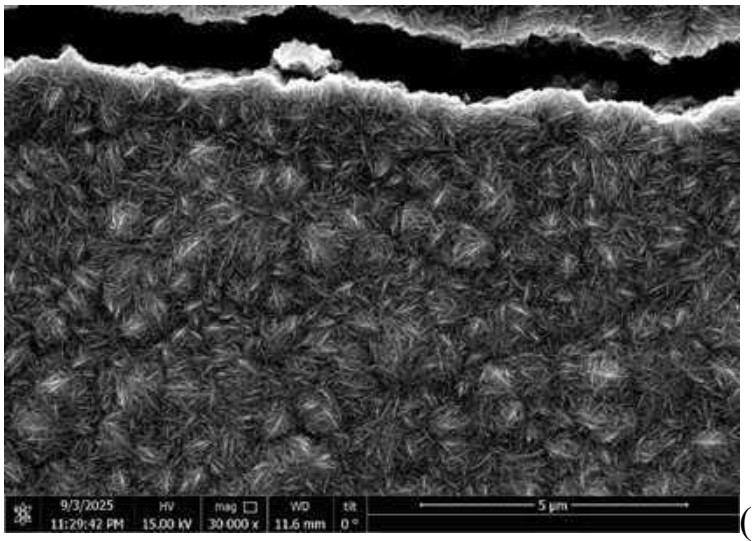

9/3/2025
2:13:54 PM
HV
15.00 kV
mag
30 000 x
WD
12.3 mm
tilt
0 °
5 µm
(*2*)

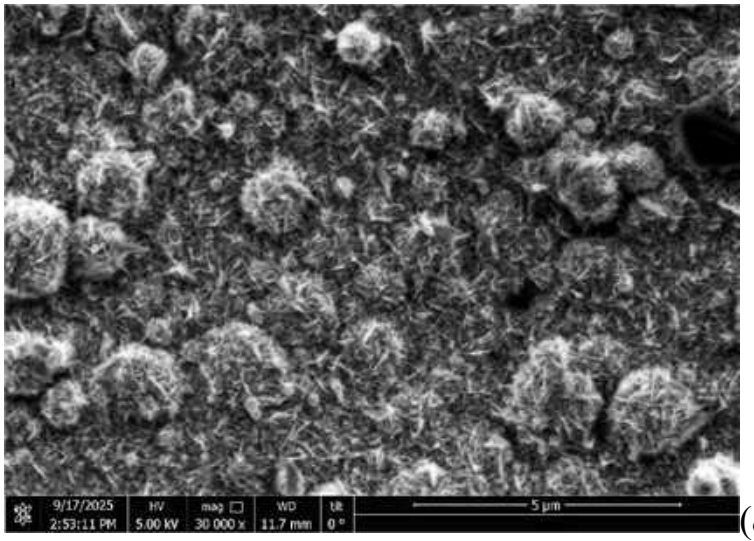

8/19/2025
2:26:48 PM
HV
10.00 kV
mag
30 000 x
WD
11.3 mm
tilt
0 °
5 µm
(*3*)

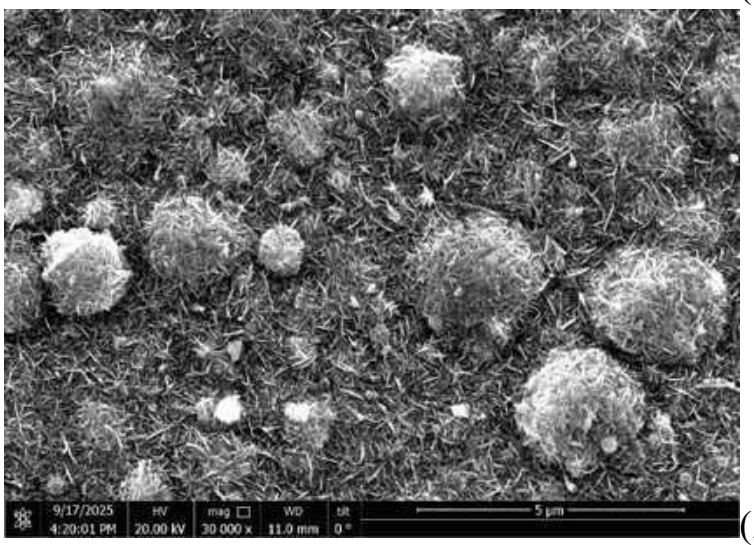

8/19/2025
3:56:43 PM
HV
10.00 kV
mag
30 000 x
WD
14.4 mm
tilt
0 °
5 µm
(*4*)

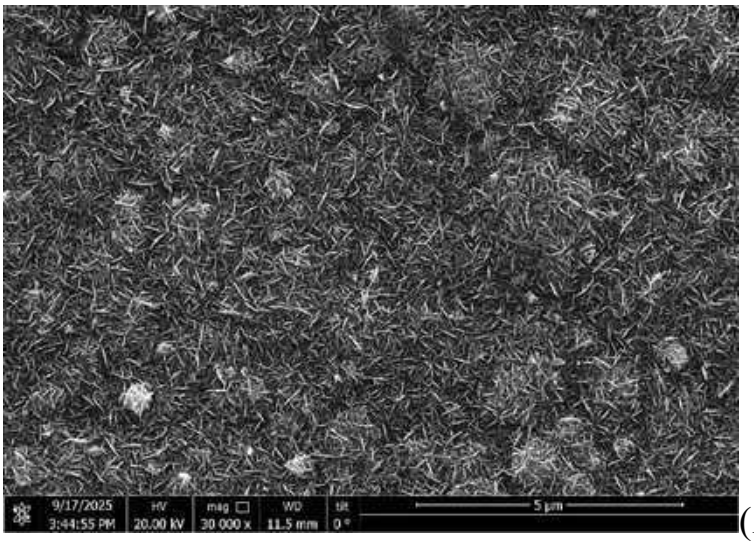

9/3/2025
2:48:40 PM
HV
15.00 kV
mag
30 000 x
WD
12.3 mm
tilt
0 °
5 µm
(***5***)

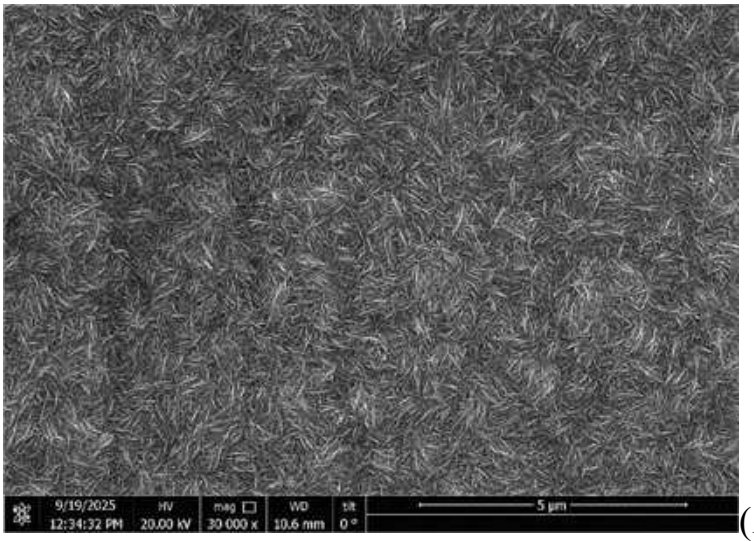

9/3/2025
11:20:21 PM
HV
15.00 kV
mag
30 000 x
WD
11.4 mm
tilt
0 °
5 µm
(***6***)

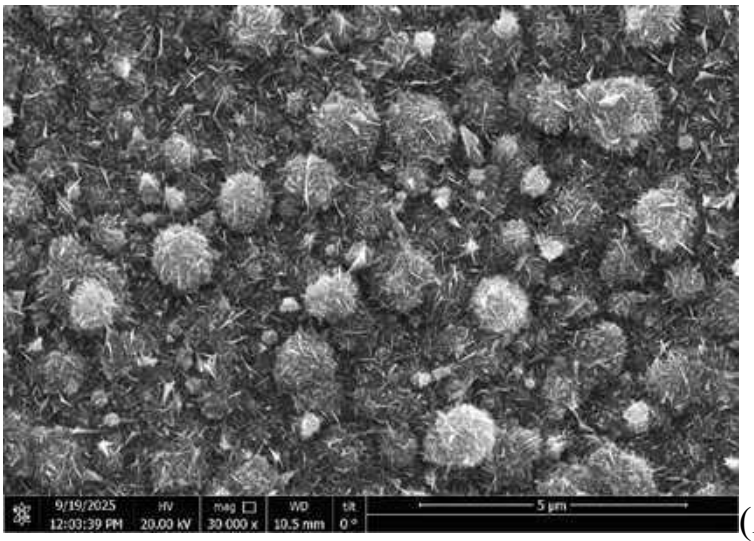

9/3/2025
11:20:42 PM
HV
15.00 kV
mag
30 000 x
WD
11.6 mm
tilt
0 °
5 µm
(*7*)

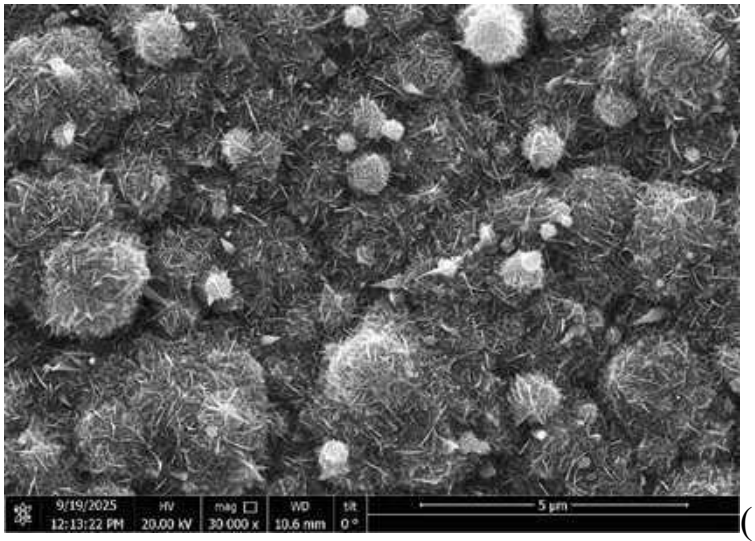

9/17/2025
2:53:11 PM
HV
5.00 kV
mag
30 000 x
WD
11.7 mm
tilt
0 °
5 µm
(*8*)

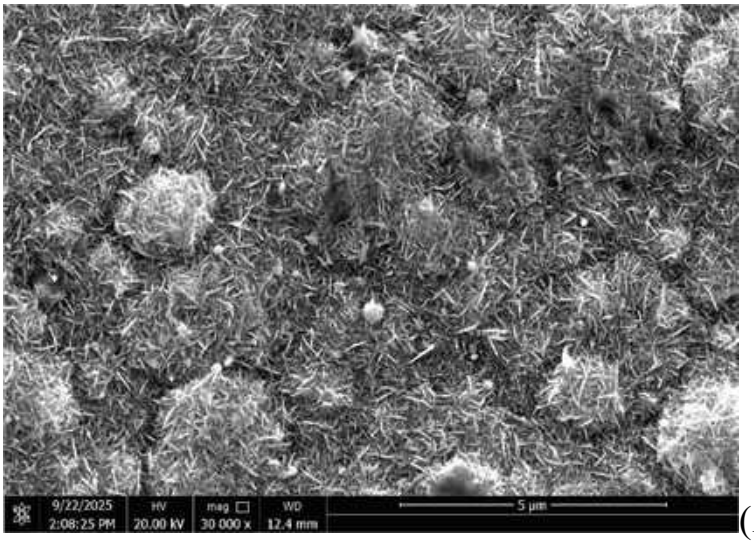

9/17/2025
4:20:01 PM
HV
20.00 kV
mag
30 000 x
WD
11.0 mm
tilt
0 °
5 µm
(*9*)

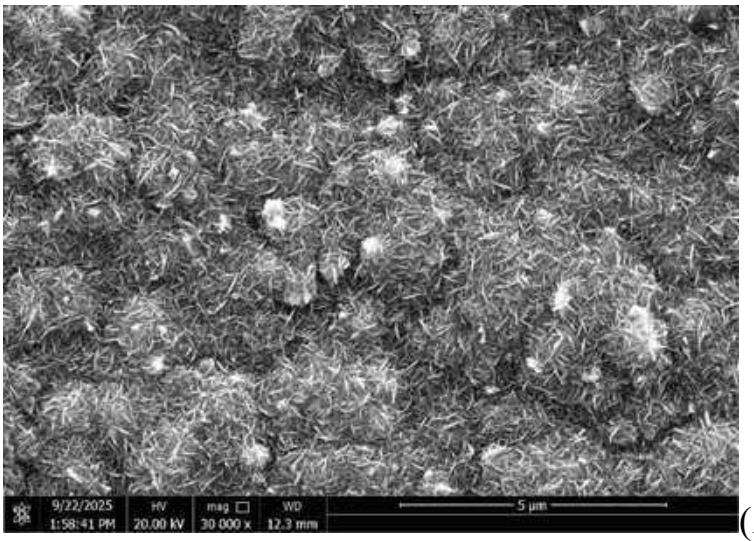

9/17/2025
3:44:55 PM
HV
20.00 kV
mag
30 000 x
WD
11.5 mm
tilt
0 °
5 µm
(*10*)

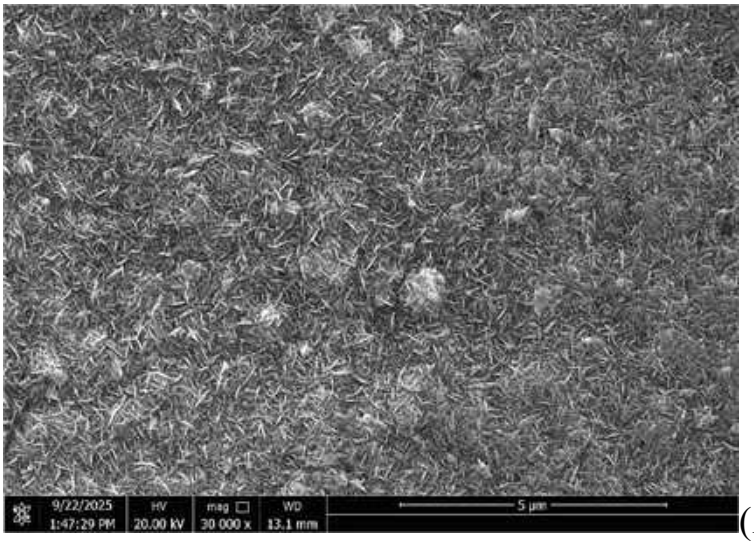

9/19/2025
12:34:32 PM
HV
20.00 kV
mag
30 000 x
WD
10.6 mm
tilt
0 °
5 µm
(*11*)

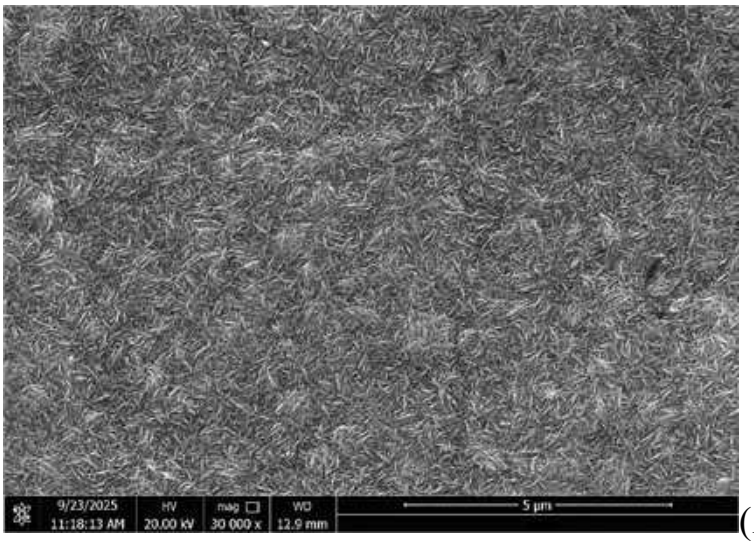

9/19/2025
12:03:39 PM
HV
20.00 kV
mag
30 000 x
WD
10.5 mm
tilt
0 °
5 µm
(***12***)

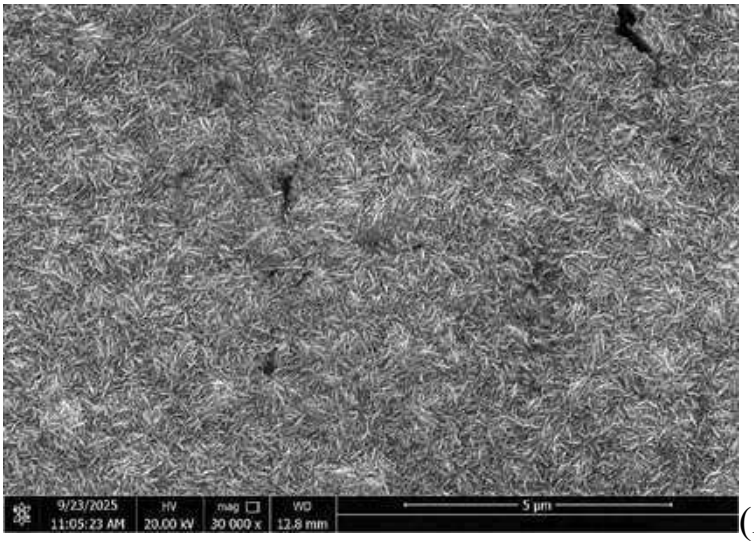

9/19/2025
12:13:22 PM
HV
20.00 kV
mag
30 000 x
WD
10.6 mm
tilt
0 °
5 µm
(13)


9/22/2025
2:08:25 PM
HV
20.00 kV
mag
30 000 x
WD
12.4 mm
5 µm
(***14***)


9/22/2025
1:58:41 PM
HV
20.00 kV
mag
30 000 x
WD
12.3 mm
5 µm
(***15***)


9/22/2025
1:47:29 PM
HV
20.00 kV
mag
30 000 x
WD
13.1 mm
5 µm
(***16***)


9/23/2025
11:18:13 AM
HV
20.00 kV
mag
30 000 x
WD
12.9 mm
5 µm
(*17*)


9/23/2025
11:05:23 AM
HV
20.00 kV
mag
30 000 x
WD
12.8 mm
5 µm
(*18*)

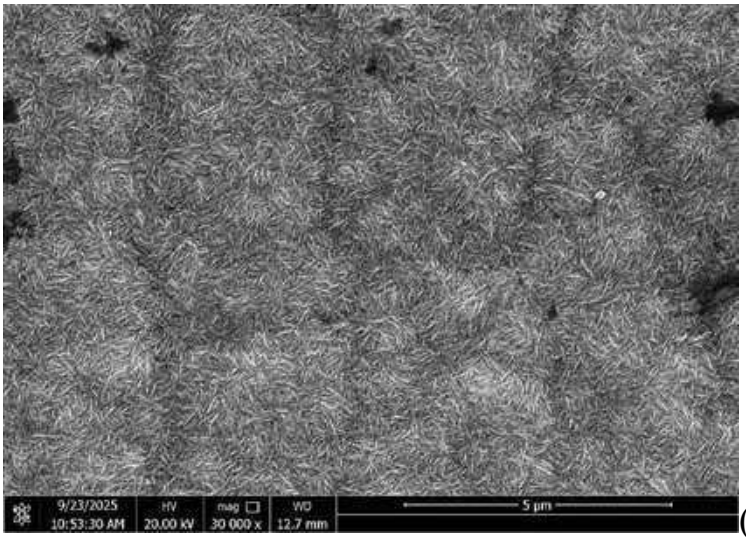
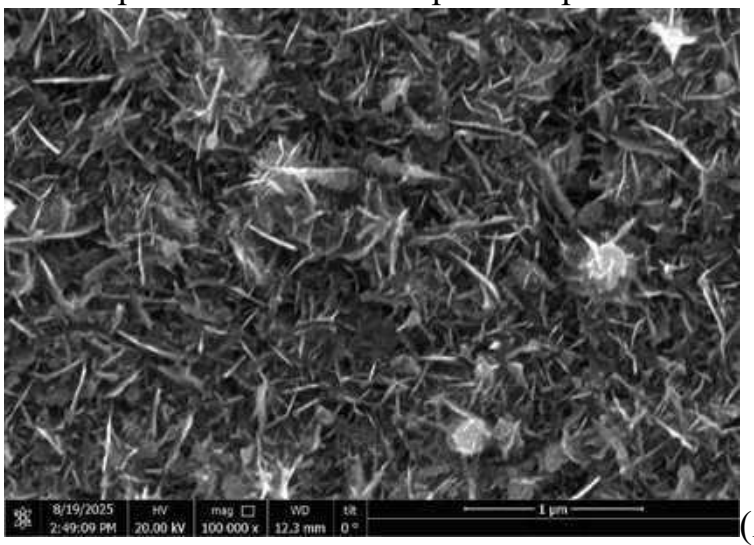
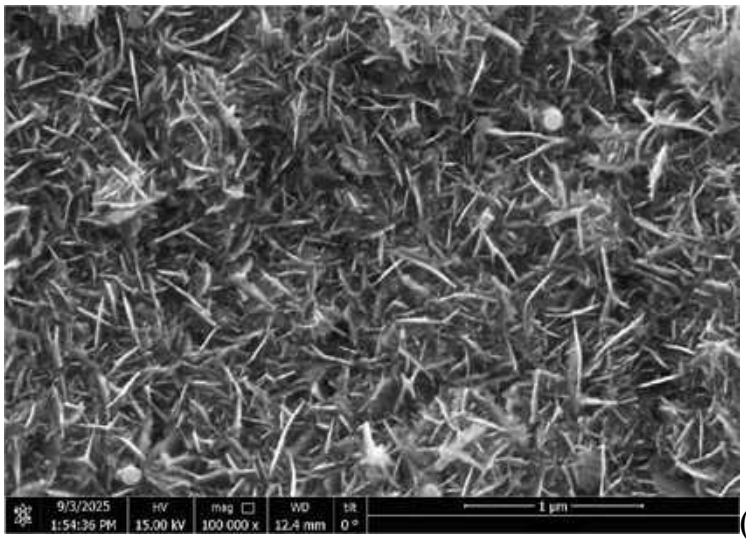

9/23/2025
10:53:30 AM
HV
20.00 kV
mag
30 000 x
WD
12.7 mm
5 µm
(*20*)

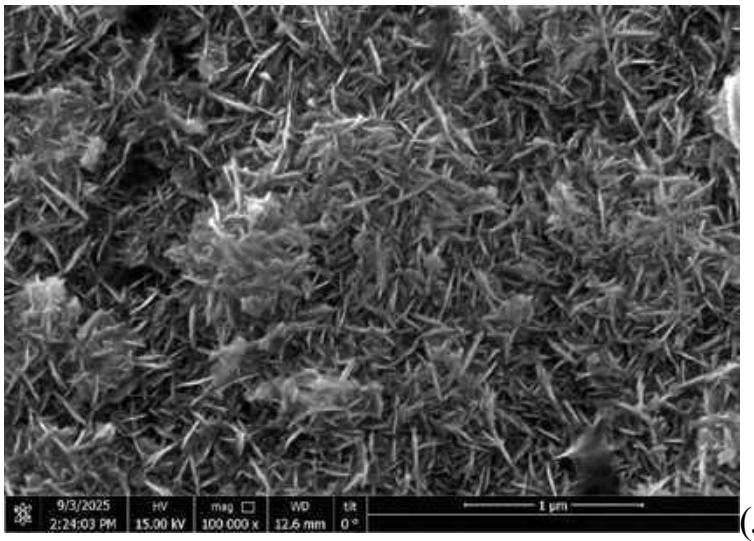
Figure 2. SEM images of Ni coatings electrodeposited from the Ethaline-based electrolyte under various conditions. Magnification: 30k×; scale bar: 5 μm.
Sample numbers correspond to the electrodeposition parameters listed in Table 1.

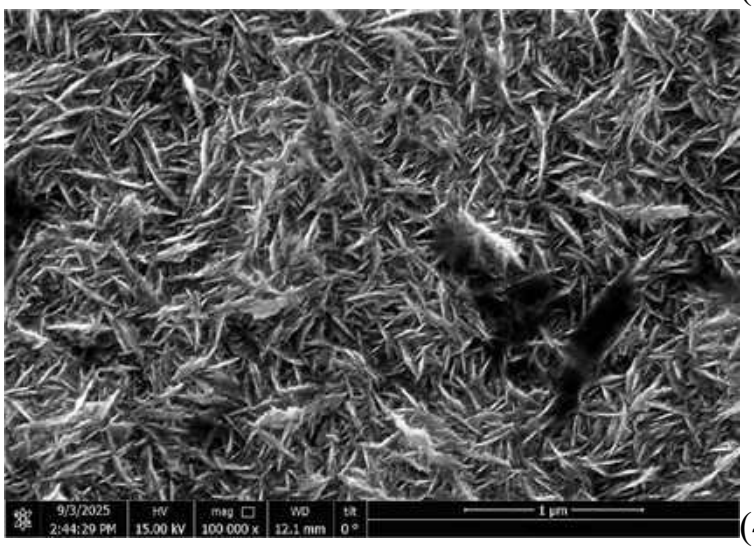


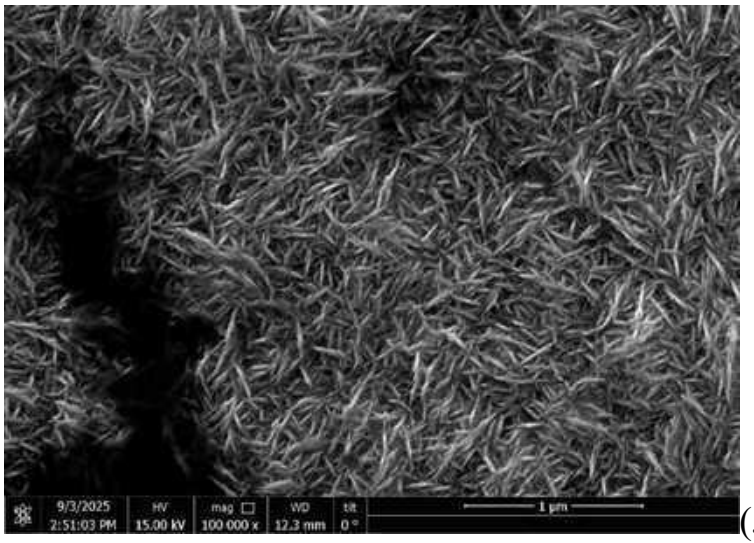
(*1*)

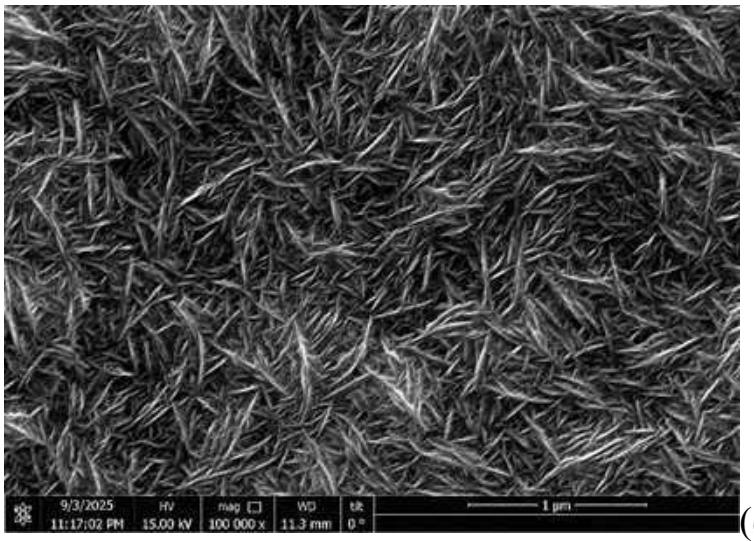


(*2*)

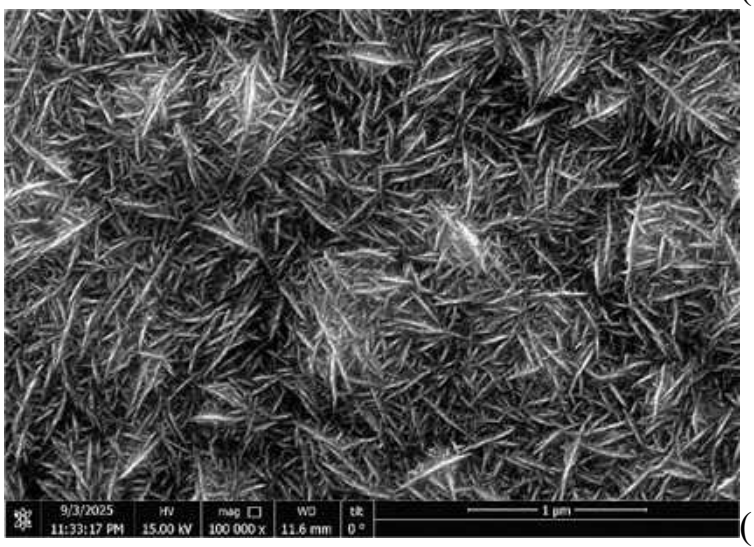

9/3/2025
2:24:03 PM
HV
15.00 kV
mag
100 000 x
WD
12.6 mm
tilt
0 °
1 µm
(*3*)


9/3/2025
2:44:29 PM
HV
15.00 kV
mag
100 000 x
WD
12.1 mm
tilt
0 °
1 µm
(*4*)

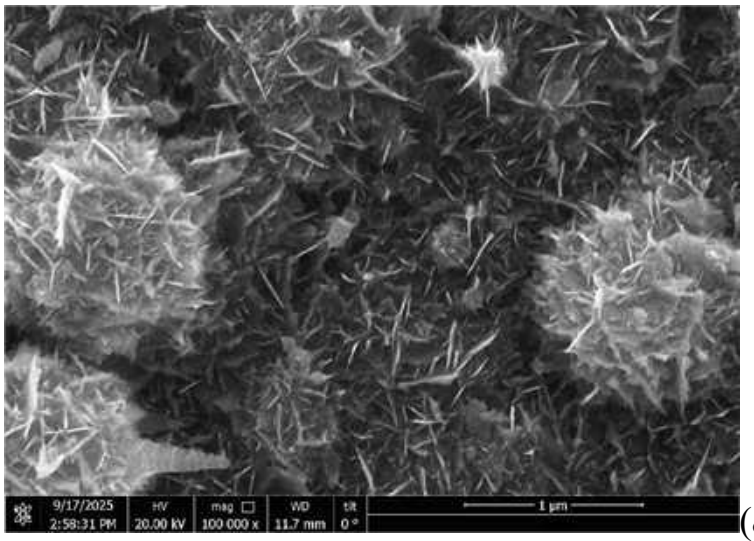

9/3/2025
2:51:03 PM
HV
15.00 kV
mag
100 000 x
WD
12.3 mm
tilt
0 °
1 µm
(*5*)

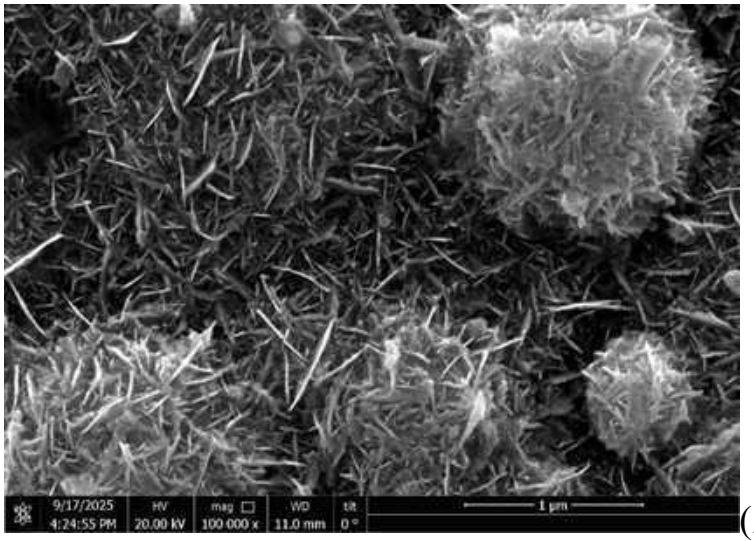

9/3/2025
11:17:02 PM
HV
15.00 kV
mag
100 000 x
WD
11.3 mm
tilt
0 °
1 µm

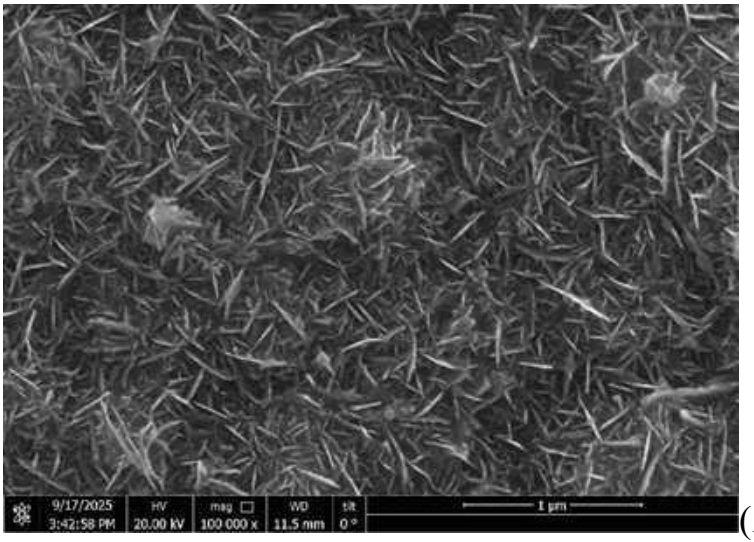
(***6***)

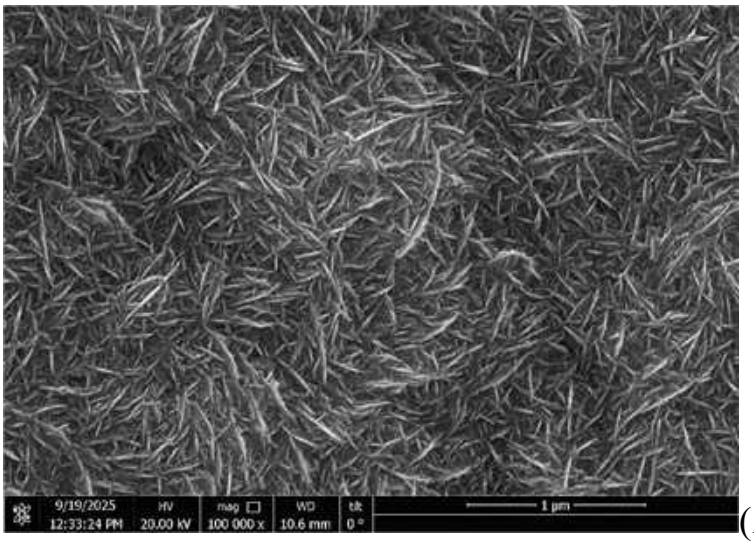

9/3/2025
11:33:17 PM
HV
15.00 kV
mag
100 000 x
WD
11.6 mm
tilt
0 °
1 µm

(***7***)

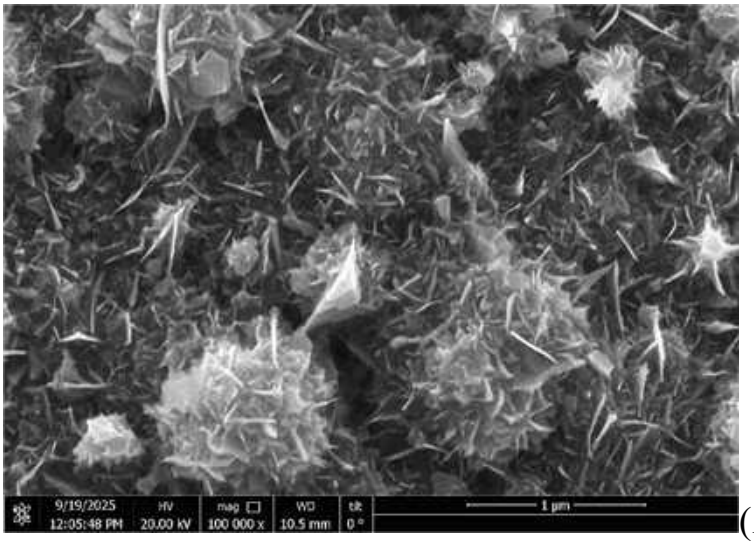

9/17/2025
2:58:31 PM
HV
20.00 kV
mag
100 000 x
WD
11.7 mm
tilt
0 °
1 µm
(***8***)


9/17/2025
4:24:55 PM
HV
20.00 kV
mag
100 000 x
WD
11.0 mm
tilt
0 °
1 µm
(***9***)

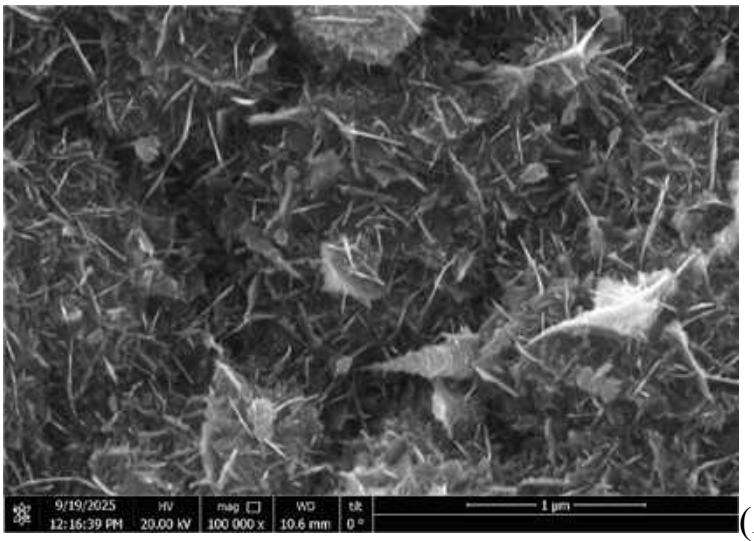

9/17/2025
3:42:58 PM
HV
20.00 kV
mag
100 000 x
WD
11.5 mm
tilt
0 °
1 µm
(***10***)

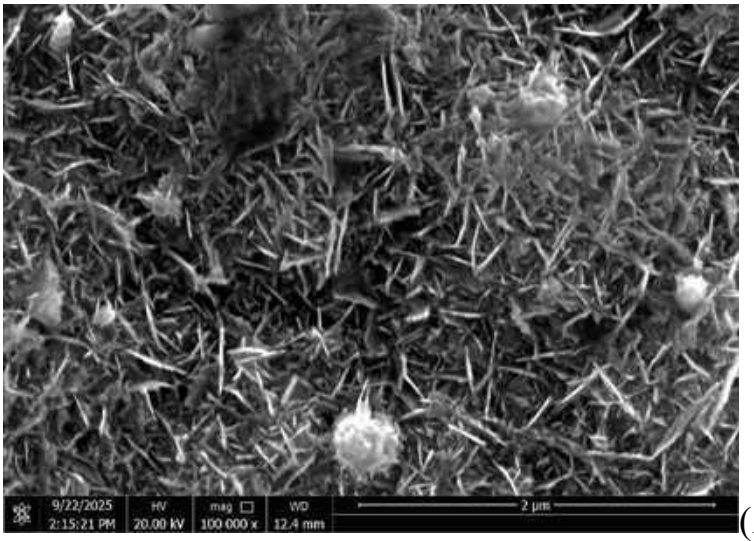

9/19/2025
12:33:24 PM
HV
20.00 kV
mag
100 000 x
WD
10.6 mm
tilt
0 °
1 µm

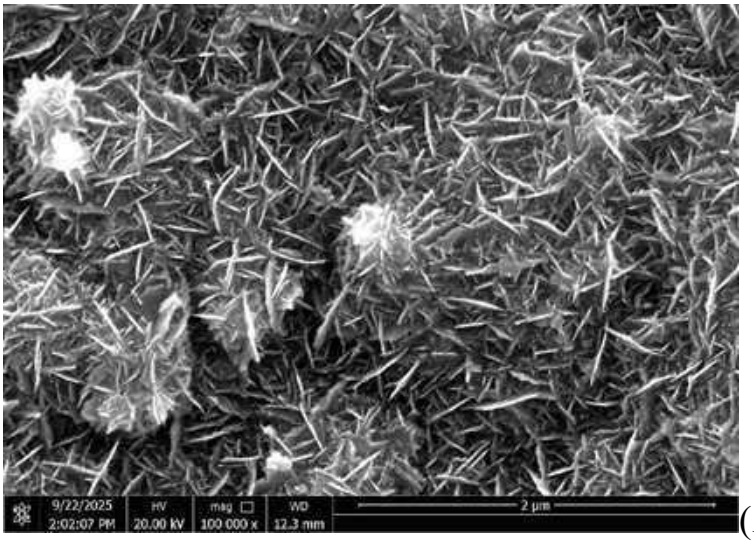
(***11***)

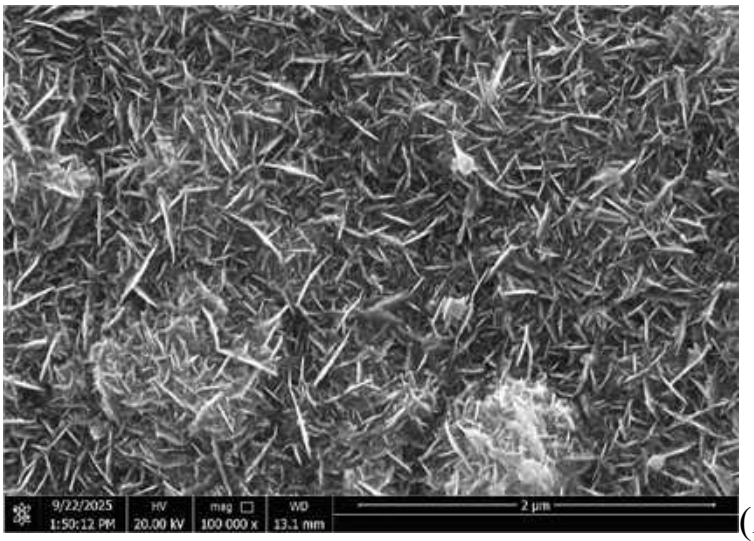

9/19/2025
12:05:48 PM
HV
20.00 kV
mag
100 000 x
WD
10.5 mm
tilt
0 °
1 µm

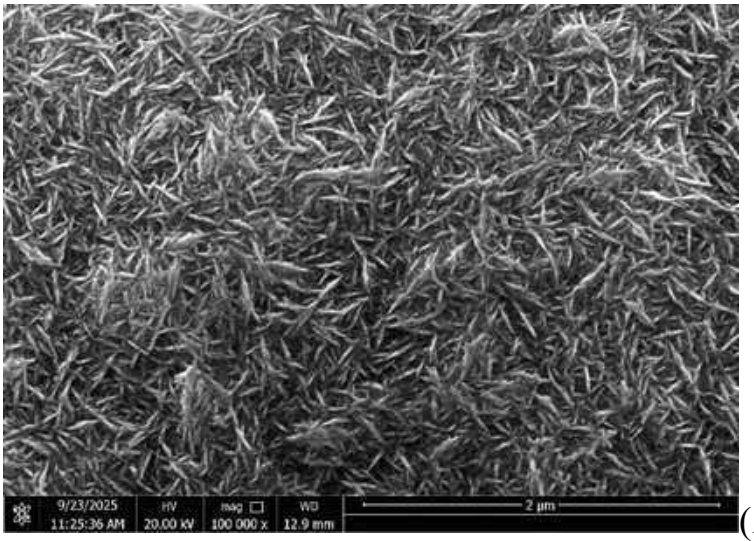
(***12***)

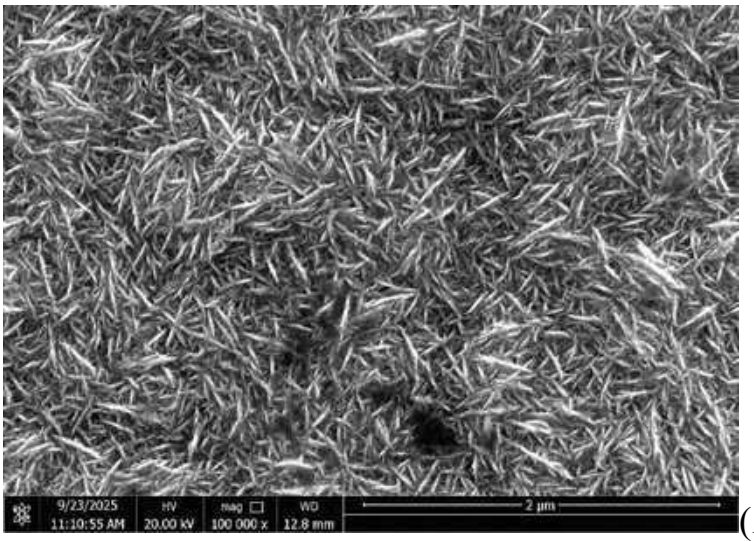

9/19/2025
12:16:39 PM
HV
20.00 kV
mag
100 000 x
WD
10.6 mm
tilt
0 °
1 µm
(*13*)


9/22/2025
2:15:21 PM
HV
20.00 kV
mag
100 000 x
WD
12.4 mm
2 µm
(*14*)

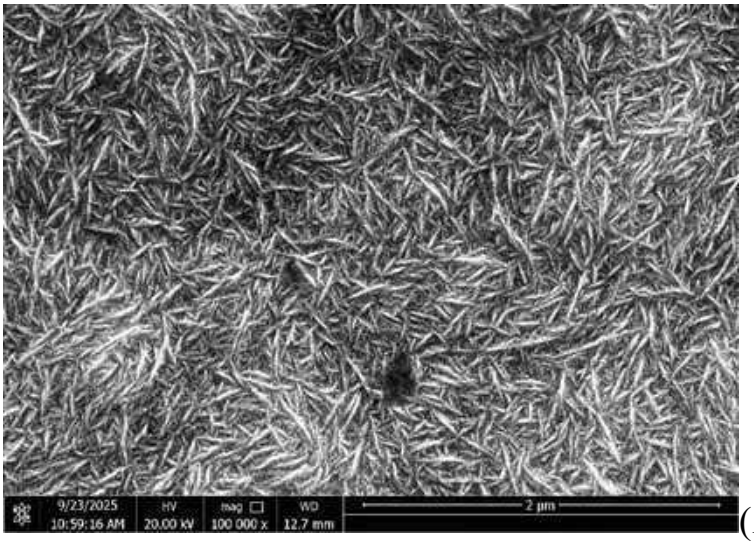

9/22/2025
2:02:07 PM
HV
20.00 kV
mag
100 000 x
WD
12.3 mm
2 µm
(*15*)


9/22/2025
1:50:12 PM
HV
20.00 kV
mag
100 000 x
WD
13.1 mm
2 µm
(*16*)


9/23/2025
11:25:36 AM
HV
20.00 kV
mag
100 000 x
WD
12.9 mm
2 µm
(*17*)



(*18*)

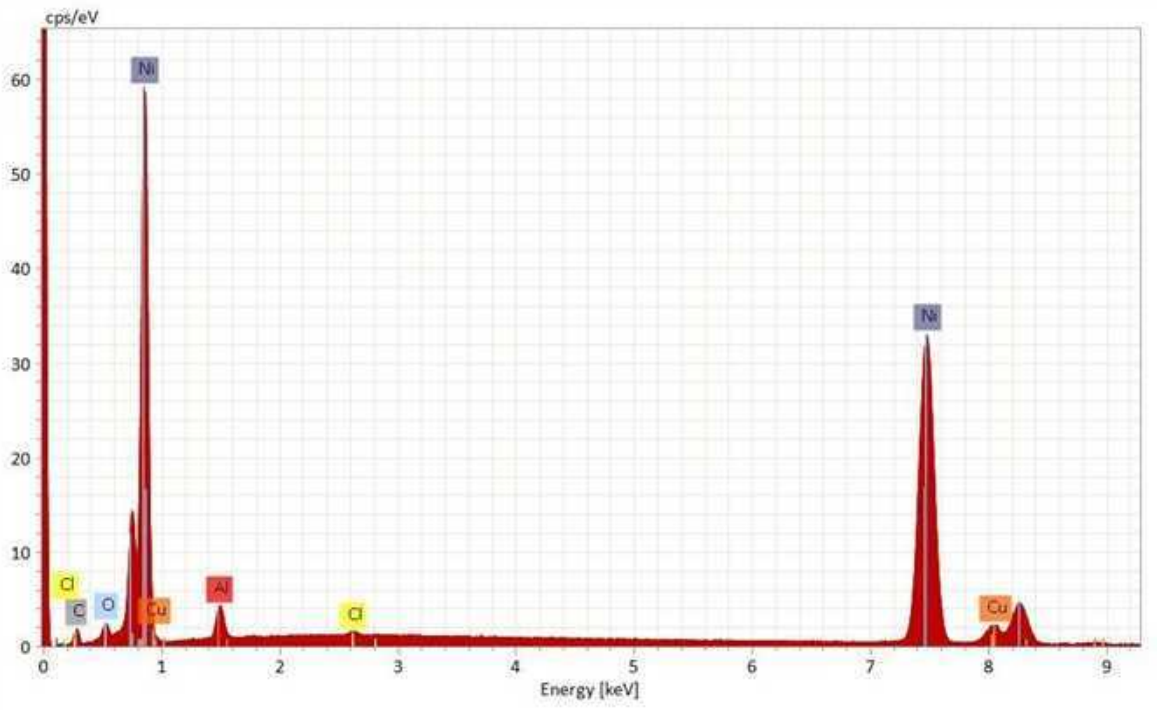


(*19*)

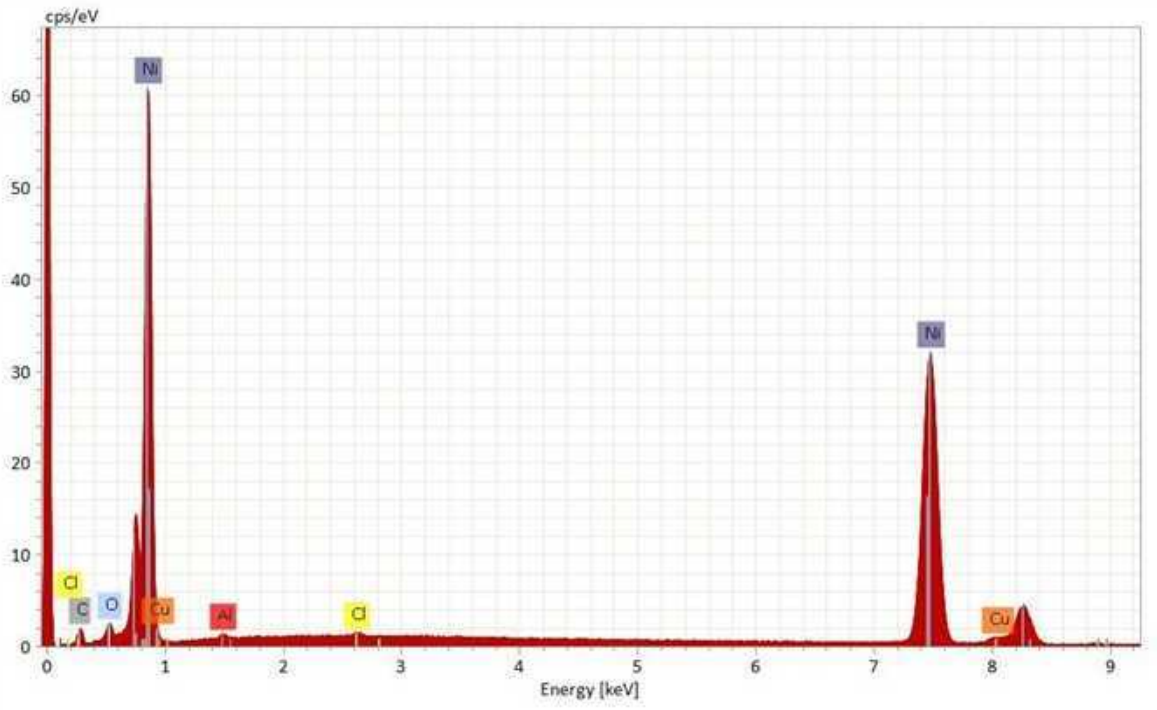
Figure 3. SEM images of Ni coatings electrodeposited from the Ethaline-based electrolyte under various conditions. Magnification: 100k×; scale bar: 1 µm. Sample numbers correspond to the electrodeposition parameters listed in Table 1.

Surface composition is another key factor that can significantly influence the catalytic activity of the coating, as the presence of specific elements or impurities may affect adsorption, reaction kinetics, and overall stability. The EDX spectra of the obtained coatings are shown in Figure 4, while the corresponding tables

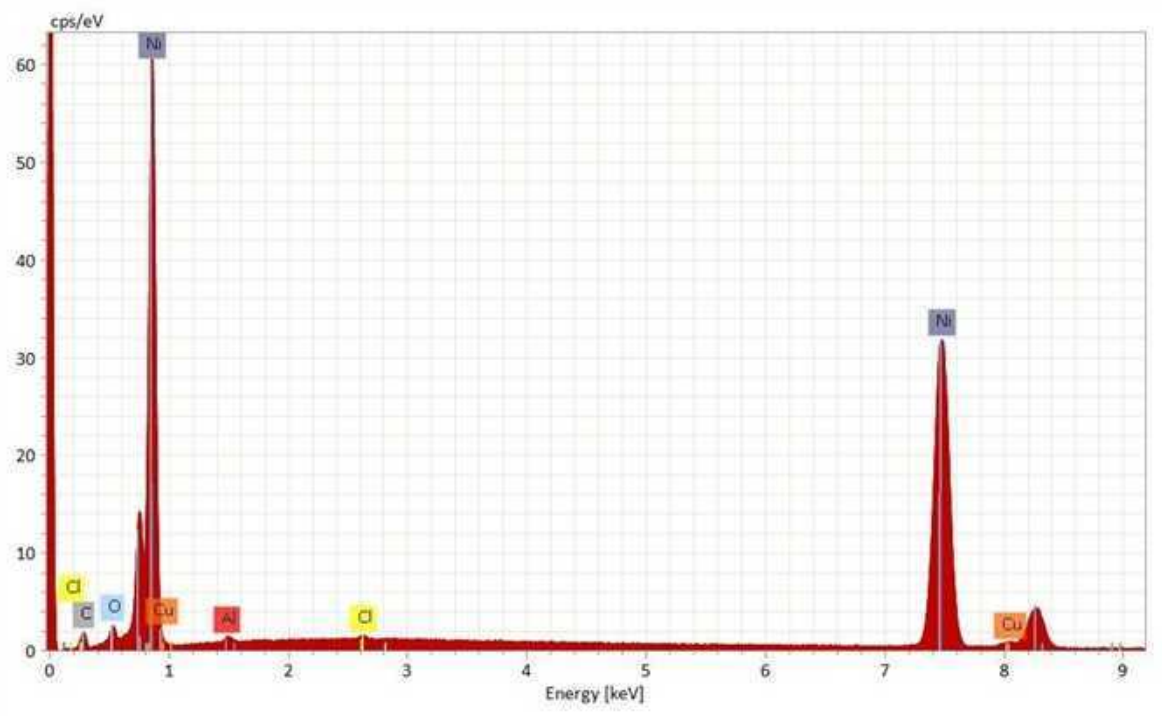
presenting the elemental composition of the deposited coatings are provided in Figure 5.



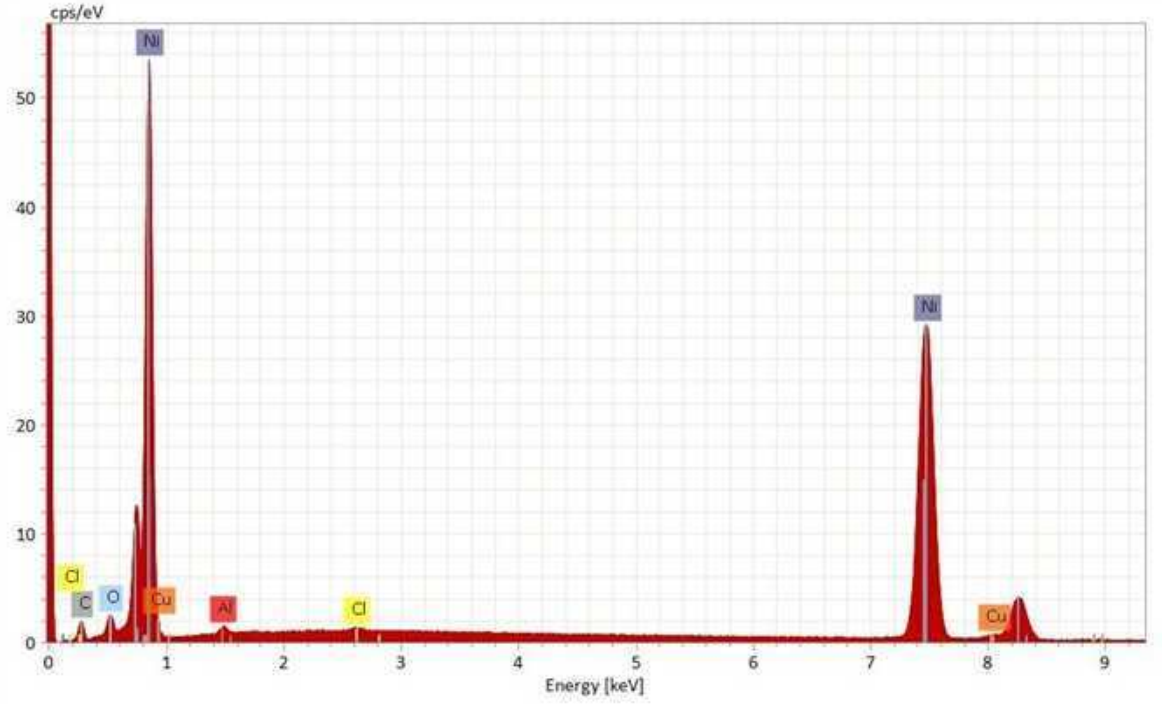
(*1*)



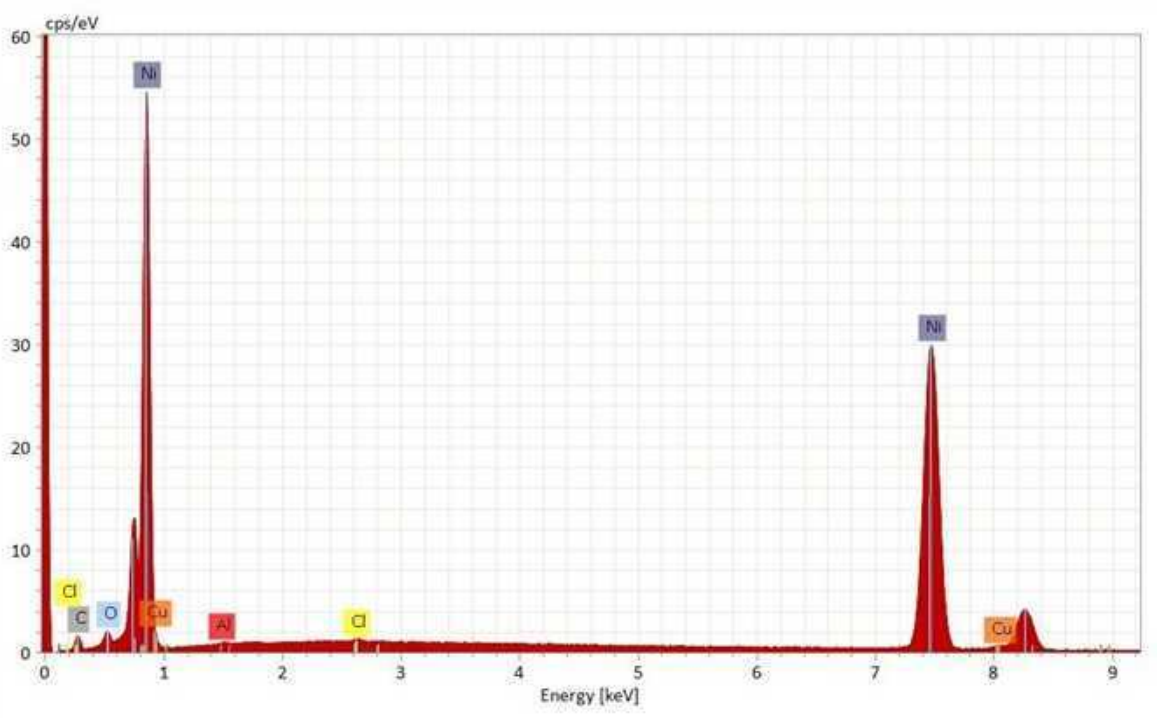
(*2*)


cps/eV
Ni
Ni
Cl
C
O
Cu
Al
Cl
Cu
Energy [keV]

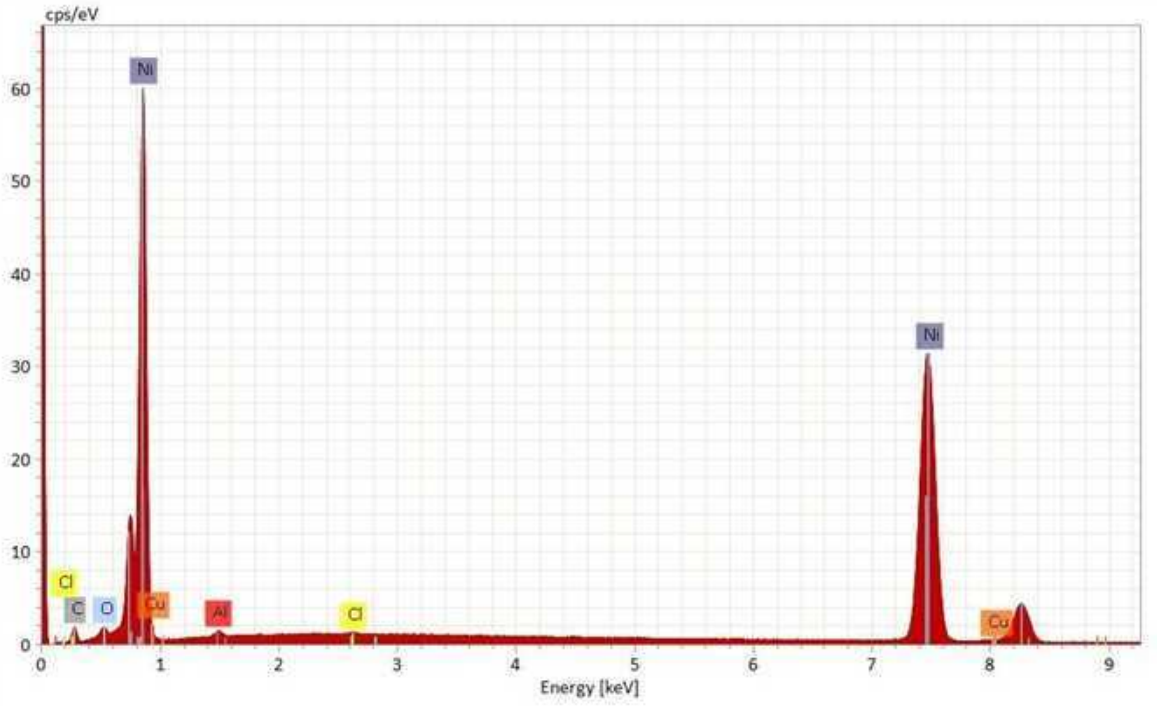
(*3*)


cps/eV
Ni
Ni
Cl
C
O
Cu
Al
Cl
Cu
Energy [keV]

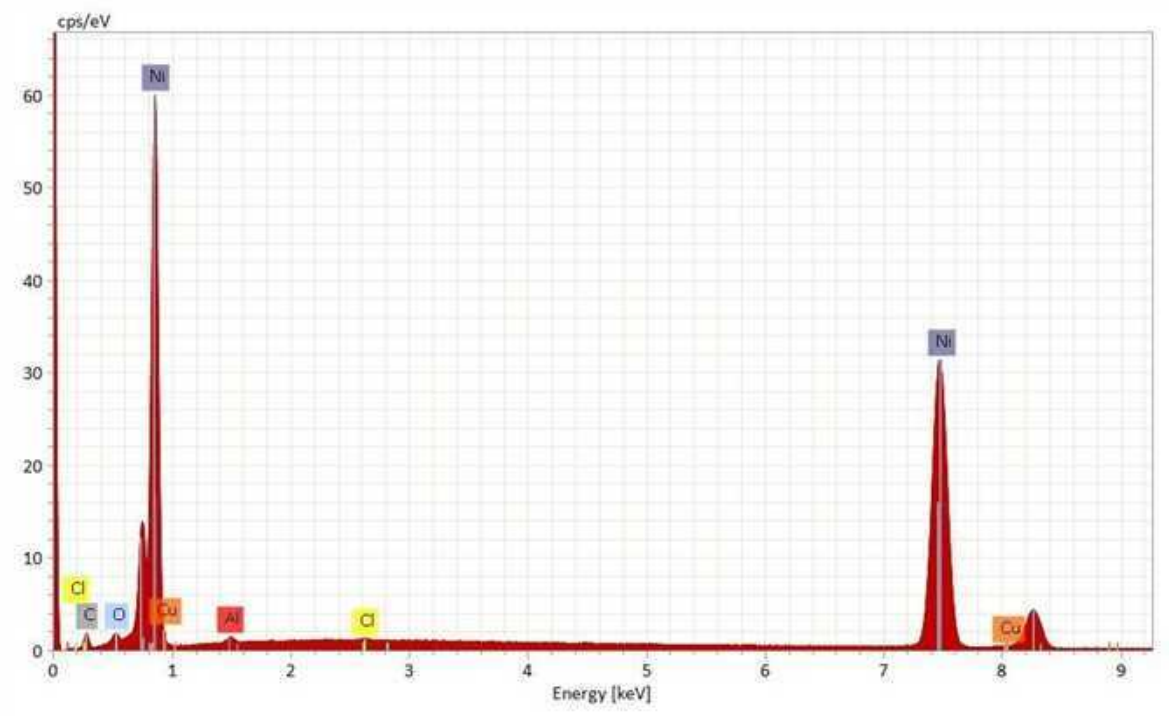
(*4*)


cps/eV
Ni
Ni
Cl
C
O
Cu
Al
Cl
Cu
Energy [keV]

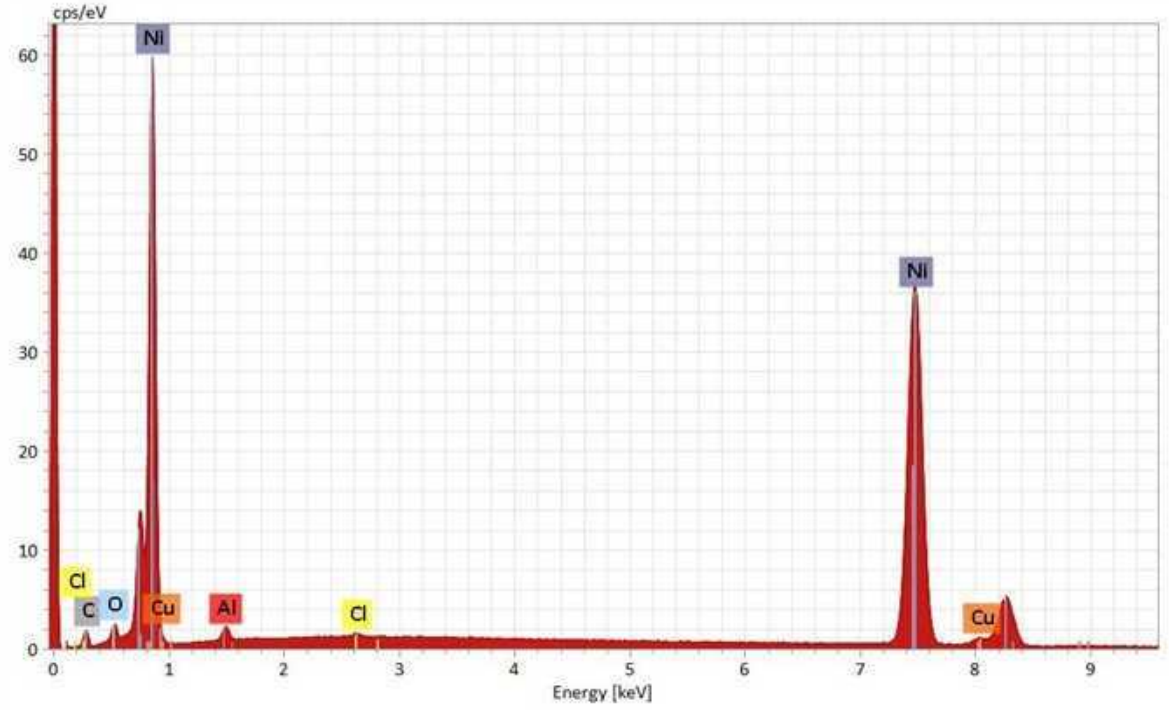
(***5***)


cps/eV
Ni
Ni
Cl
C
O
Cu
Al
Cl
Cu
Energy [keV]

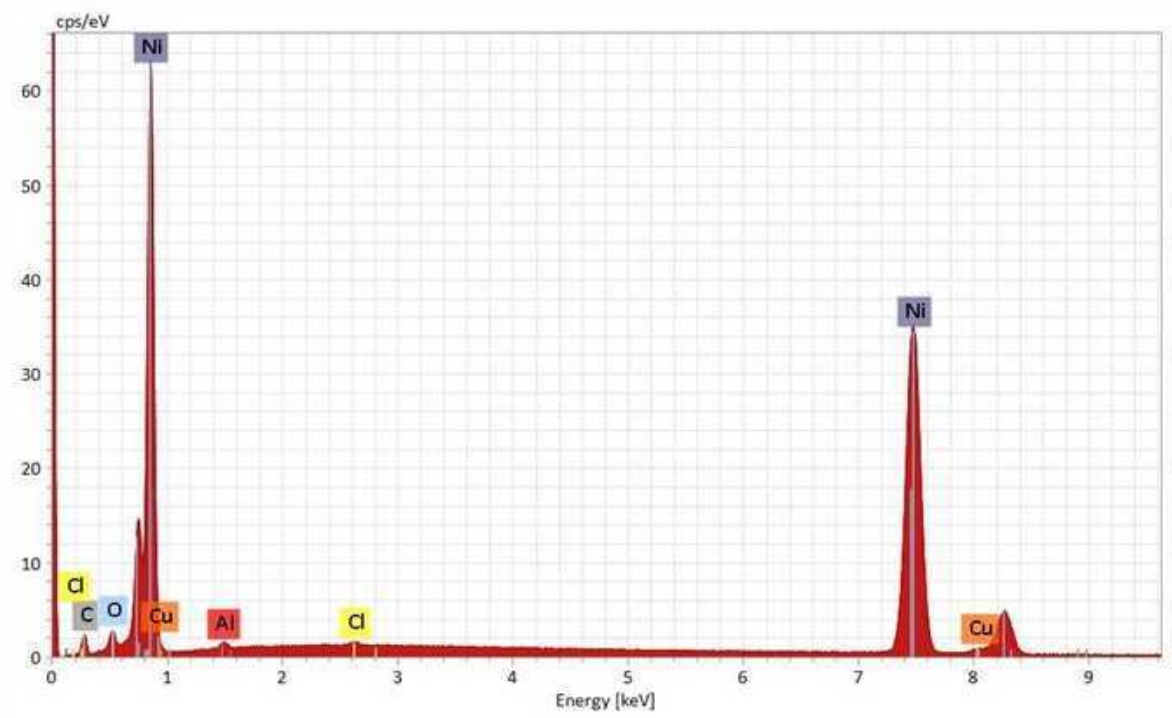
(***6***)


cps/eV
Ni
Ni
Cl
C
O
Cu
Al
Cl
Cu
Energy [keV]

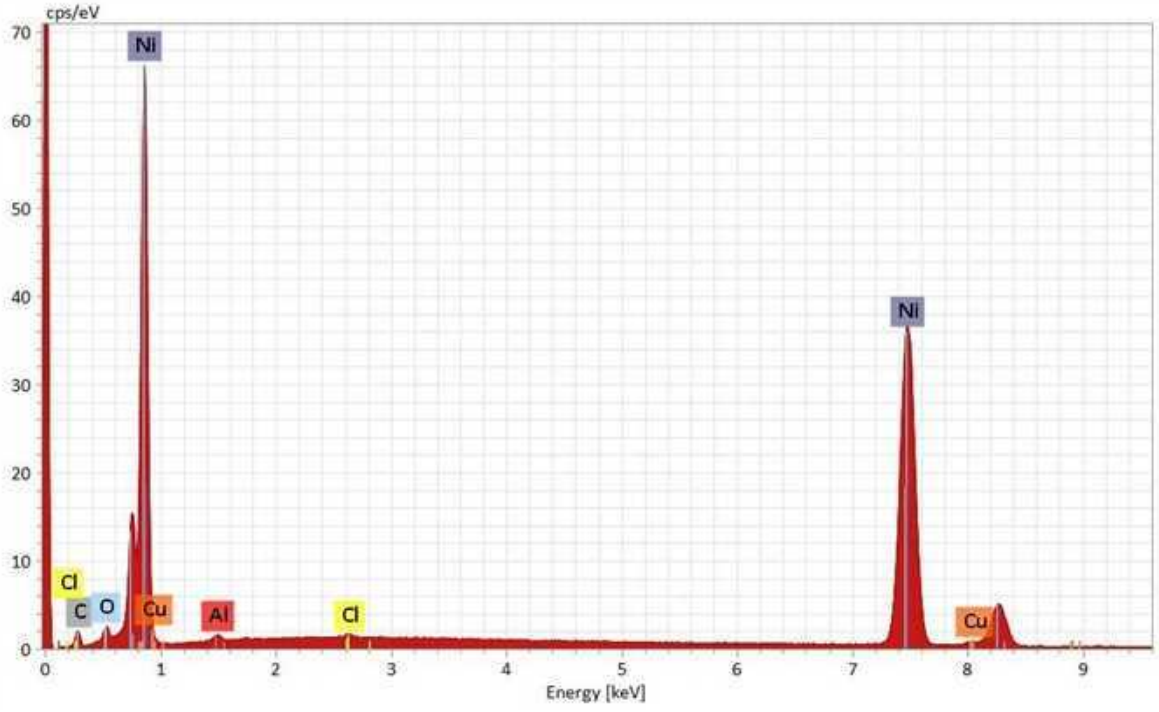
(*7*)


cps/eV
Ni
Ni
Cl
C
O
Cu
Al
Cl
Cu
Energy [keV]

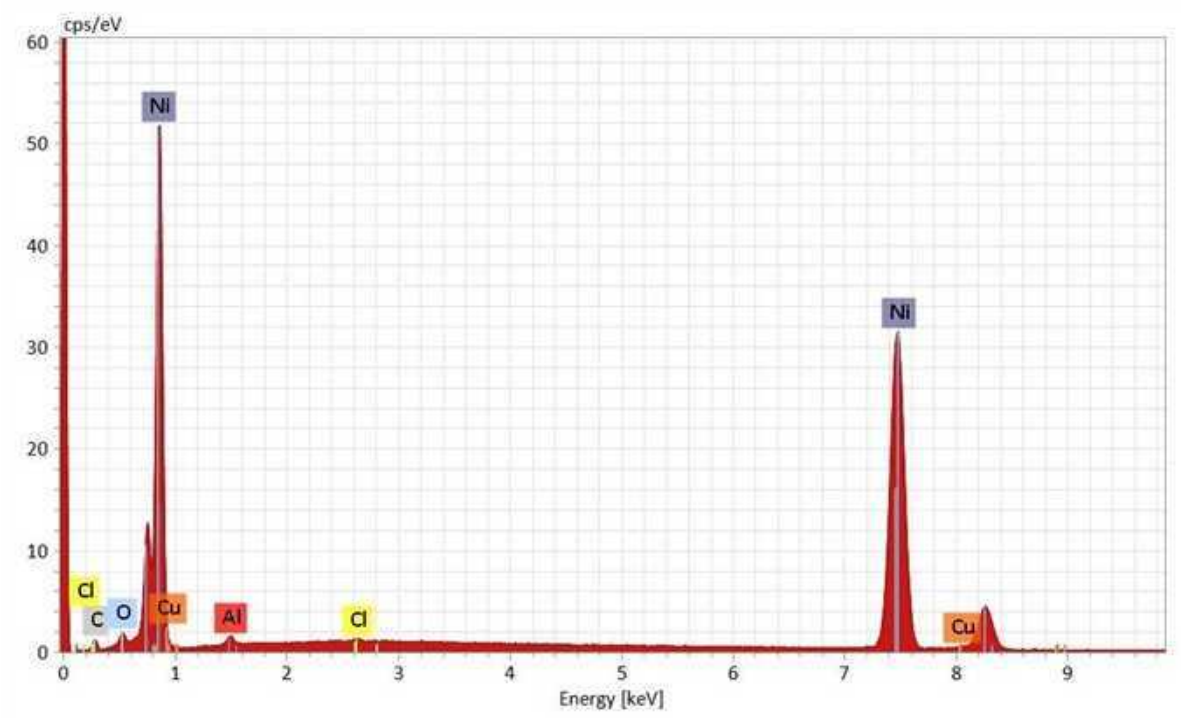
(*8*)


cps/eV
Ni
Ni
Cl
C
O
Cu
Al
Cl
Cu
Energy [keV]

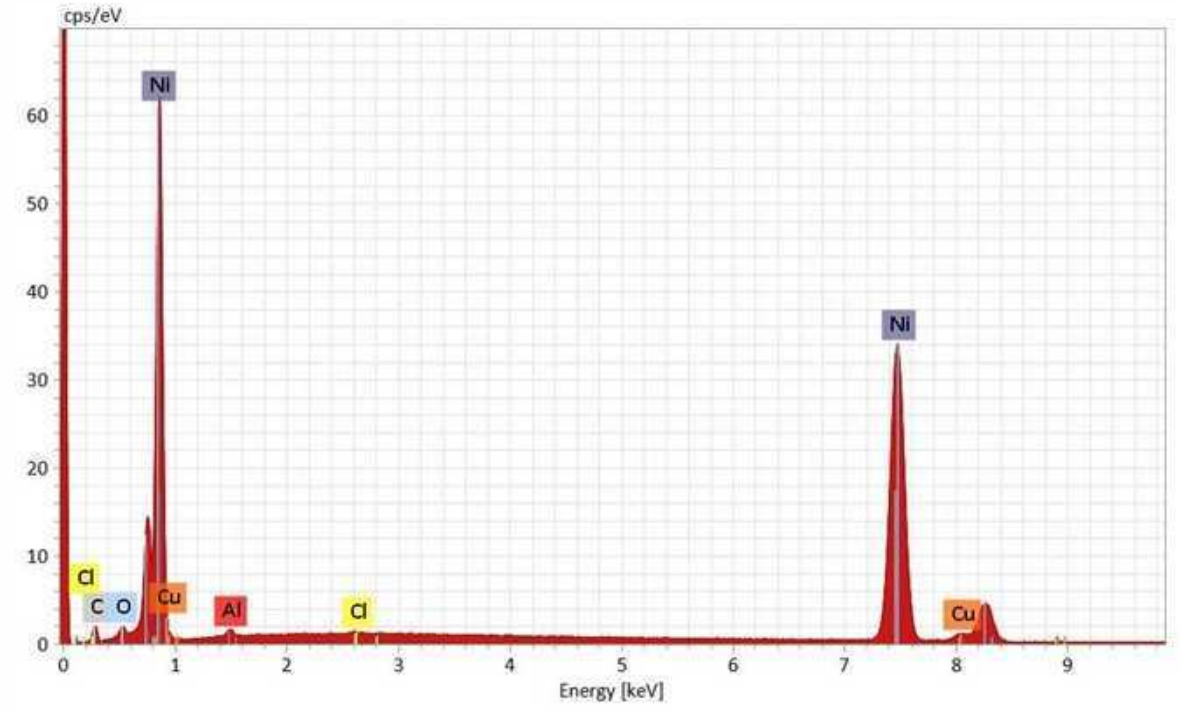
(***9***)


cps/eV
Ni
Ni
Cl
C
O
Cu
Al
Cl
Cu
Energy [keV]

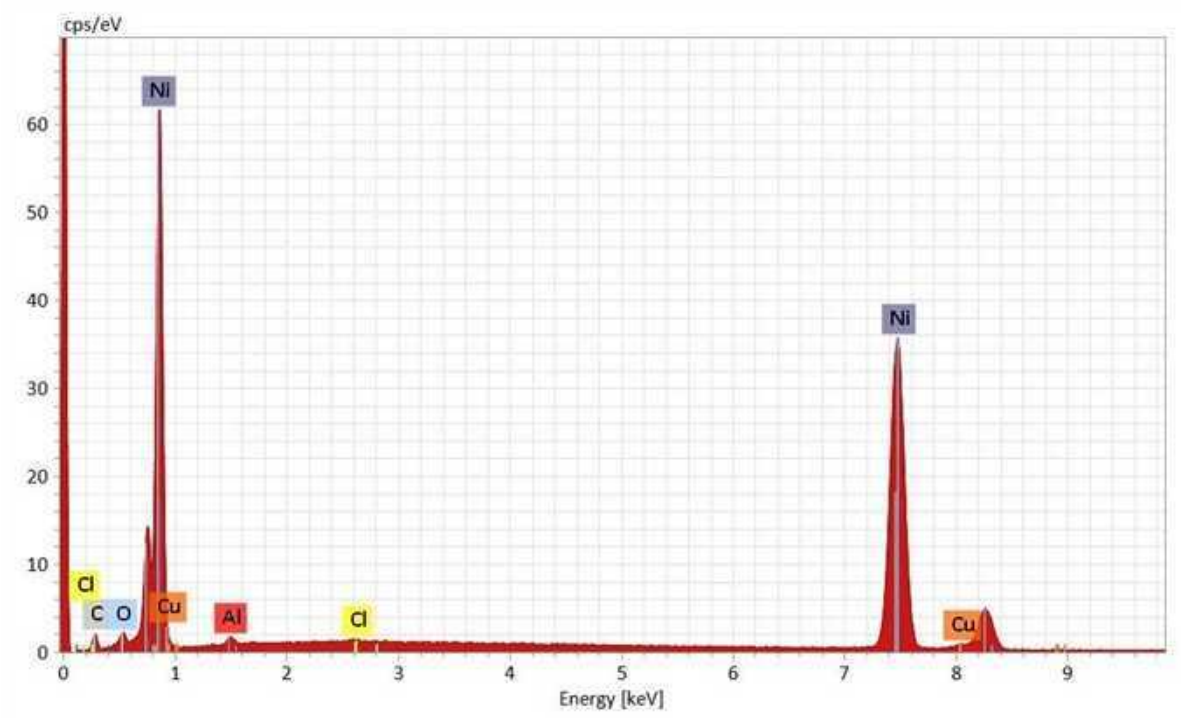
(***10***)


cps/eV
60
50
40
30
20
10
0
Ni
Ni
Cl
C
O
Cu
Al
Cl
Cu
0
1
2
3
4
5
6
7
8
9
Energy [keV]

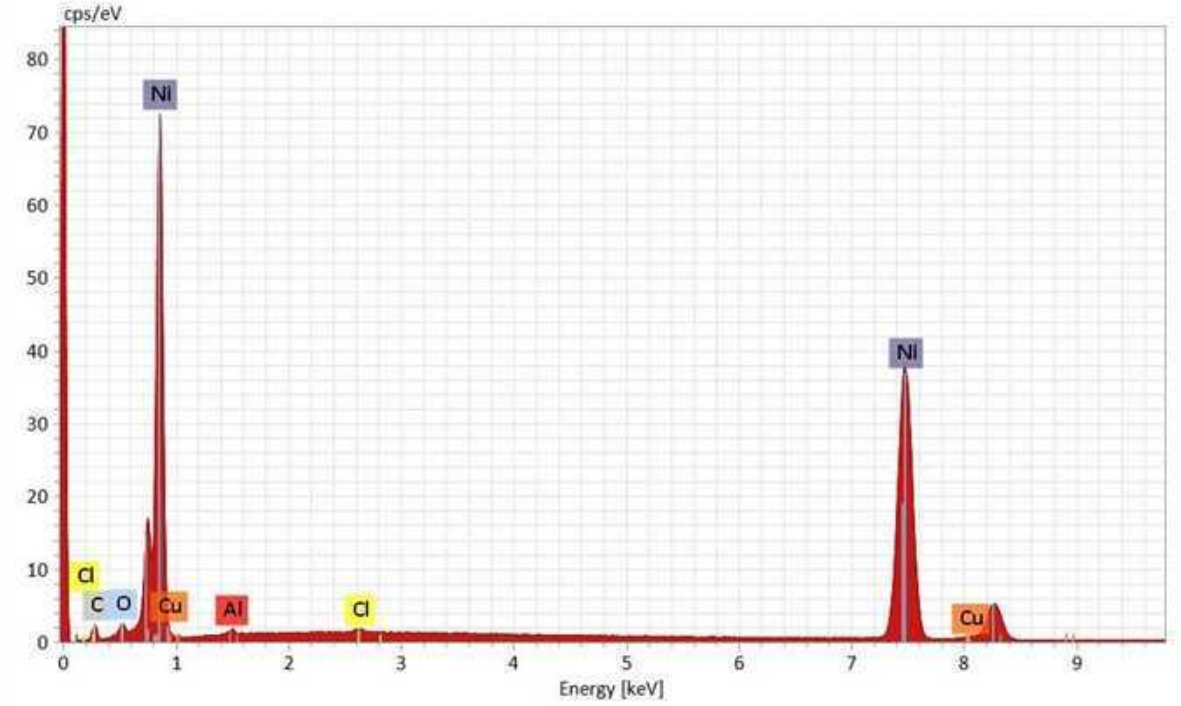
(***11***)


cps/eV
60
50
40
30
20
10
0
Ni
Ni
Cl
C
O
Cu
Al
Cl
Cu
0
1
2
3
4
5
6
7
8
9
Energy [keV]

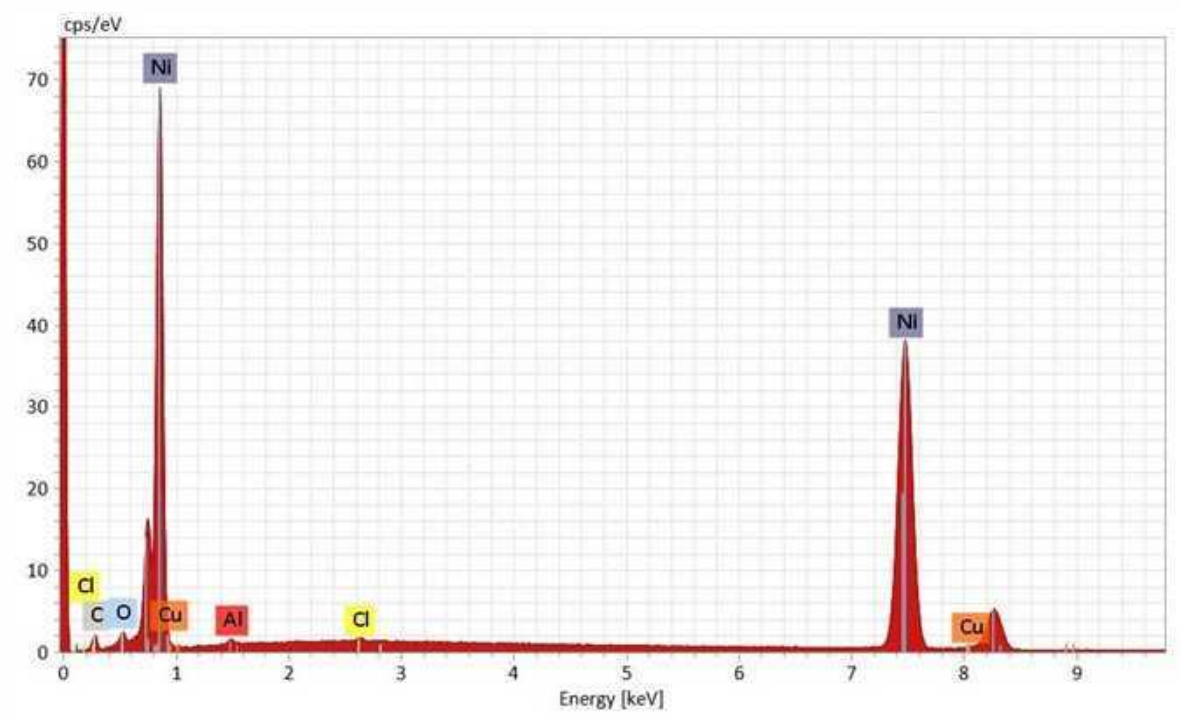
(***12***)


cps/eV
Ni
Ni
Cl
C O
Cu
Al
Cl
Cu
Energy [keV]

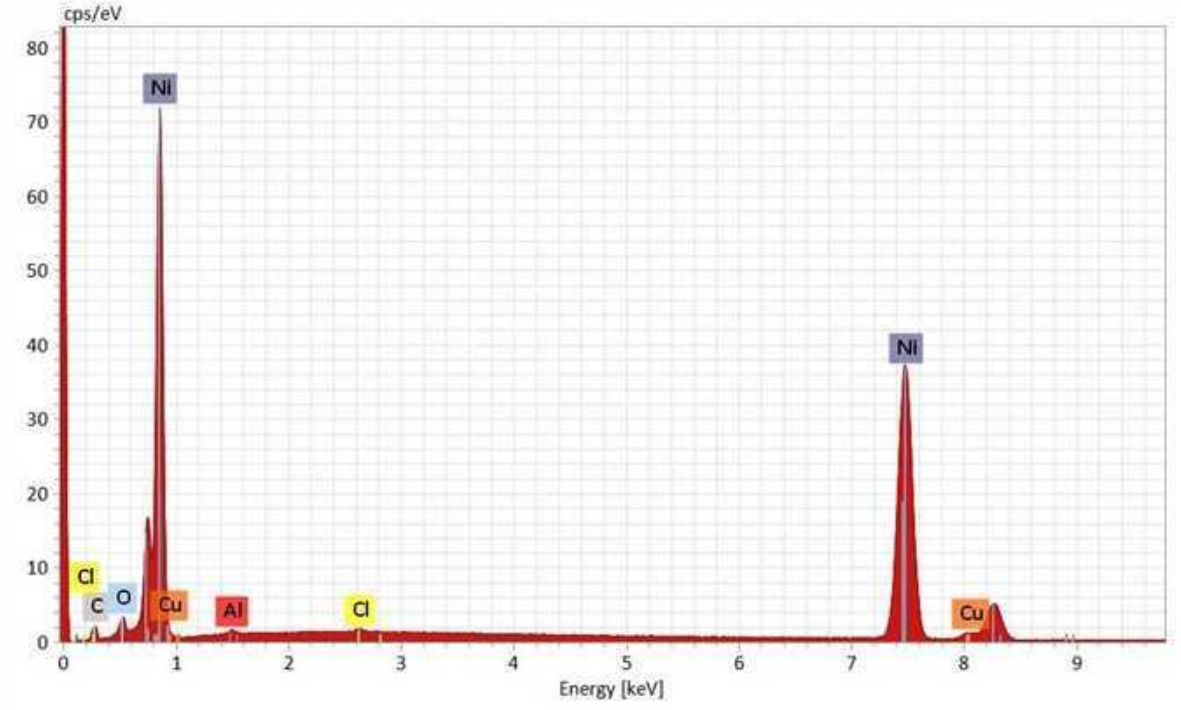
(***13***)


cps/eV
Ni
Ni
Cl
C O
Cu
Al
Cl
Cu
Energy [keV]

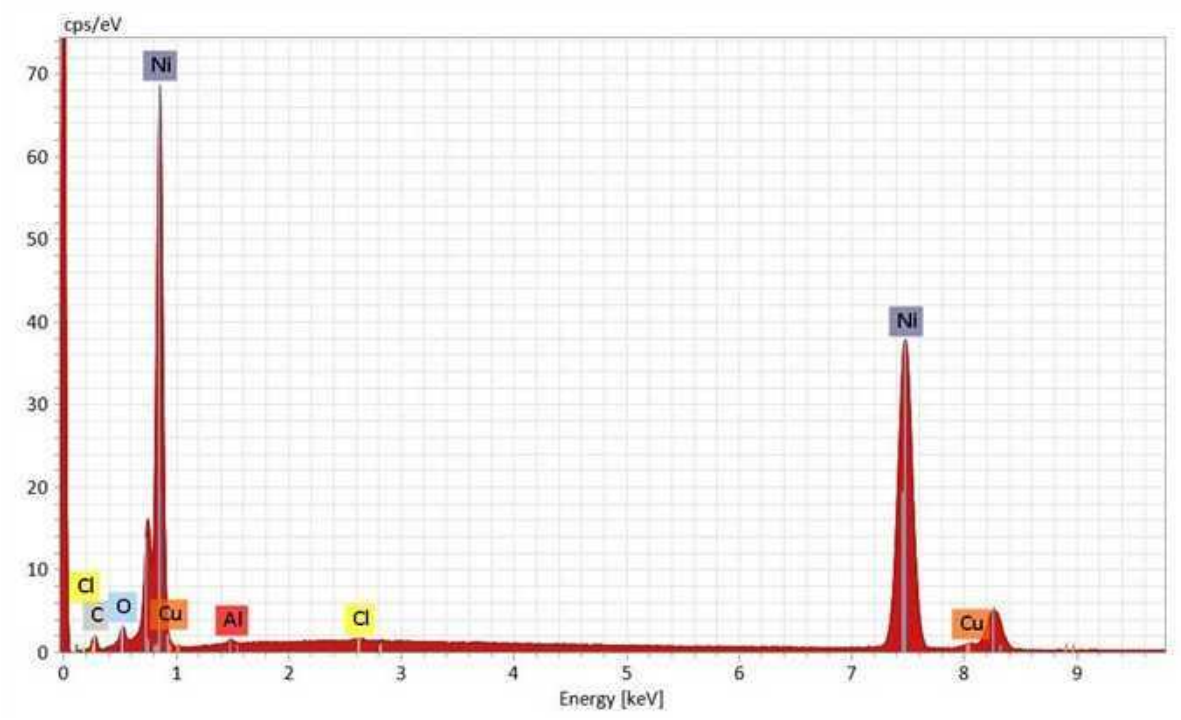
(***14***)


cps/eV
Ni
Ni
Cl
C
O
Cu
Al
Cl
Cu
Energy [keV]

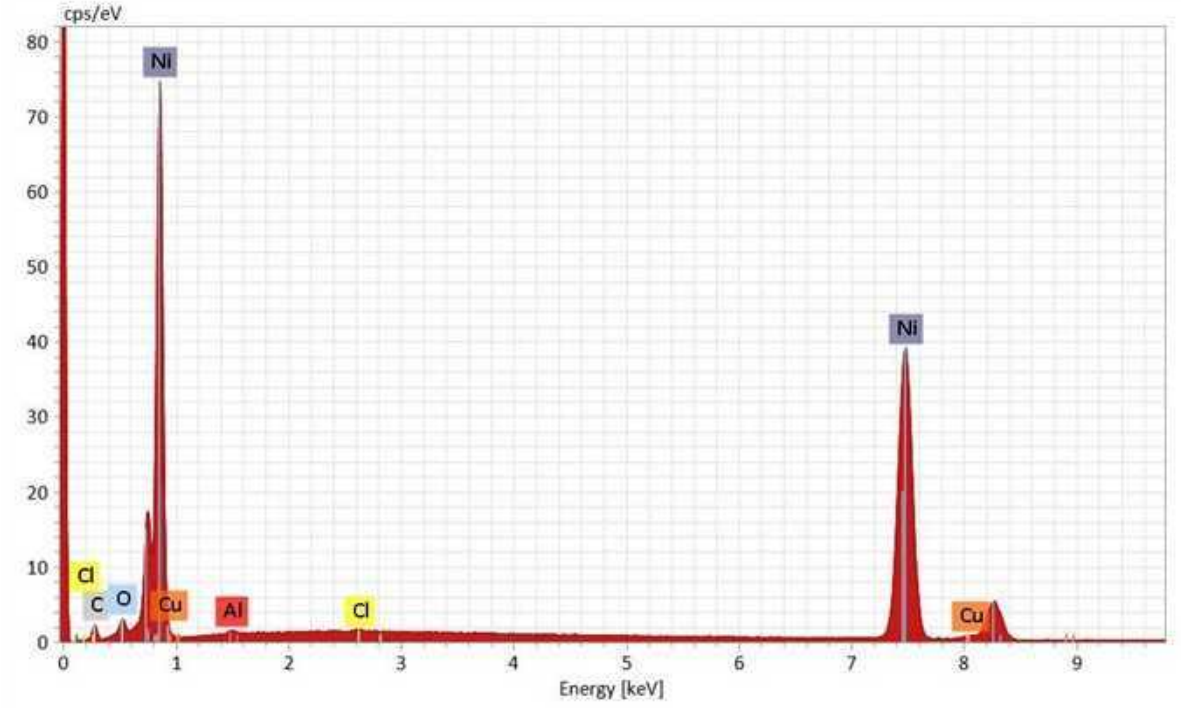
(***15***)


cps/eV
Ni
Ni
Cl
C
O
Cu
Al
Cl
Cu
Energy [keV]

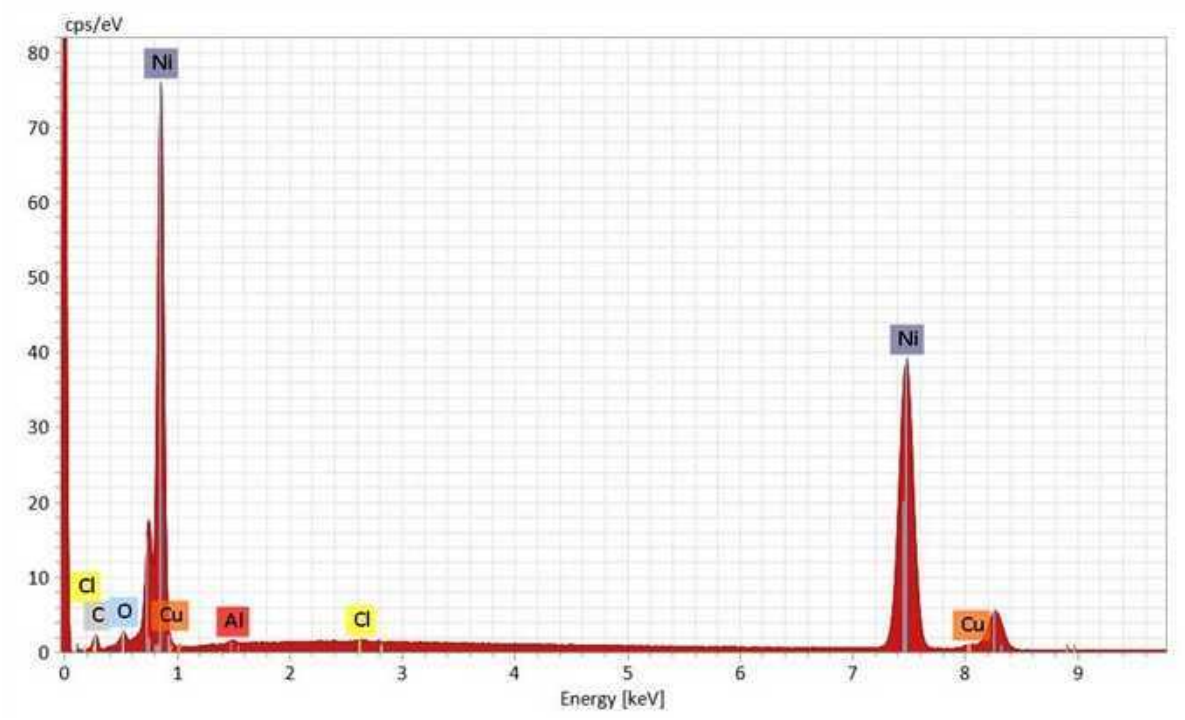
(***16***)


cps/eV
Ni
Ni
Cl
C
O
Cu
Al
Cl
Cu
Energy [keV]

(*17*)


cps/eV
Ni
Ni
Cl
C
O
Cu
Al
Cl
Cu
Energy [keV]

(*18*)



(*19*)

Figure 4. EDX spectra of Ni coatings electrodeposited from the Ethaline-based electrolyte under various conditions. Sample numbers correspond to the electrodeposition parameters listed in Table 1.

1_20kV

Element	At. No.	Netto	Mass [%]	Mass Norm. [%]	Atom [%]	abs. error [%] (1 sigma)	rel. error [%] (1 sigma)
Carbon	6	3619	4.94	5.16	19.91	0.29	5.81
Oxygen	8	3715	1.34	1.40	4.05	0.07	5.52
Aluminium	13	13796	2.58	2.69	4.63	0.11	4.36
Chlorine	17	1856	0.20	0.21	0.27	0.01	7.50
Nickel	28	295347	80.64	84.12	66.46	1.49	1.85
Copper	29	17601	6.16	6.42	4.69	0.14	2.25
		Sum	**95.86**	**100.00**	**100.00**		

(*1*)

2_20kV

Element	At. No.	Netto	Mass [%]	Mass Norm. [%]	Atom [%]	abs. error [%] (1 sigma)	rel. error [%] (1 sigma)
Carbon	6	4238	5.84	6.08	23.16	0.34	5.83
Oxygen	8	4129	1.56	1.62	4.64	0.08	5.45
Aluminium	13	1778	0.32	0.34	0.57	0.03	7.92
Chlorine	17	1974	0.21	0.22	0.28	0.02	7.19
Nickel	28	300456	85.57	89.04	69.40	1.61	1.88
Copper	29	7110	2.59	2.70	1.94	0.07	2.84
		Sum	**96.10**	**100.00**	**100.00**		

(***2***)

3_20kV

Element	At. No.	Netto	Mass [%]	Mass Norm. [%]	Atom [%]	abs. error [%] (1 sigma)	rel. error [%] (1 sigma)
Carbon	6	3952	5.47	5.72	21.99	0.32	5.87
Oxygen	8	4092	1.54	1.61	4.64	0.08	5.46
Aluminium	13	2243	0.41	0.43	0.74	0.03	7.03
Chlorine	17	1720	0.18	0.19	0.25	0.01	7.98
Nickel	28	302615	86.15	90.04	70.91	1.62	1.88
Copper	29	5329	1.93	2.02	1.47	0.06	3.15
		Sum	**95.69**	**100.00**	**100.00**		

(***3***)

4_20kV

Element	At. No.	Netto	Mass [%]	Mass Norm. [%]	Atom [%]	abs. error [%] (1 sigma)	rel. error [%] (1 sigma)
Carbon	6	4425	5.87	6.24	23.43	0.34	5.80
Oxygen	8	5069	1.85	1.97	5.54	0.10	5.28
Aluminium	13	2985	0.55	0.58	0.97	0.03	6.25
Chlorine	17	2000	0.21	0.22	0.29	0.02	7.15
Nickel	28	306991	84.24	89.62	68.81	1.57	1.86
Copper	29	3716	1.28	1.37	0.97	0.05	3.83
		Sum	**94.00**	**100.00**	**100.00**		

(***4***)

5_20kV

Element	At. No.	Netto	Mass [%]	Mass Norm. [%]	Atom [%]	abs. error [%] (1 sigma)	rel. error [%] (1 sigma)
Carbon	6	4009	5.40	5.73	22.24	0.32	5.97
Oxygen	8	3376	1.24	1.31	3.83	0.07	5.62
Aluminium	13	533	0.10	0.10	0.18	0.02	17.47
Chlorine	17	1342	0.14	0.15	0.20	0.01	9.69
Nickel	28	310907	86.25	91.63	72.76	1.61	1.86
Copper	29	2845	1.01	1.07	0.79	0.05	4.51
		Sum	**94.14**	**100.00**	**100.00**		

(***5***)

6_20kV

Element	At. No.	Netto	Mass [%]	Mass Norm. [%]	Atom [%]	abs. error [%] (1 sigma)	rel. error [%] (1 sigma)
Carbon	6	3713	5.14	5.49	21.55	0.30	5.86
Oxygen	8	2363	0.88	0.94	2.78	0.05	6.20
Aluminium	13	2385	0.44	0.47	0.82	0.03	6.85
Chlorine	17	982	0.11	0.11	0.15	0.01	11.59
Nickel	28	305062	86.36	92.21	74.12	1.61	1.87
Copper	29	2005	0.73	0.78	0.58	0.04	5.59
		Sum	**93.66**	**100.00**	**100.00**		

(***6***)

7_20kV

Element	At. No.	Netto	Mass [%]	Mass Norm. [%]	Atom [%]	abs. error [%] (1 sigma)	rel. error [%] (1 sigma)
Carbon	6	2873	3.73	3.99	16.42	0.22	6.00
Oxygen	8	2877	0.97	1.04	3.21	0.06	5.77
Aluminium	13	1984	0.42	0.45	0.82	0.03	7.31
Chlorine	17	520	0.06	0.06	0.08	0.01	20.01
Nickel	28	334423	87.64	93.88	79.02	1.59	1.82
Copper	29	1603	0.54	0.57	0.45	0.04	6.84
		Sum	**93.35**	**100.00**	**100.00**		

(***7***)

8_20kV

Element	At. No.	Netto	Mass [%]	Mass Norm. [%]	Atom [%]	abs. error [%] (1 sigma)	rel. error [%] (1 sigma)
Carbon	6	3635	4.64	5.01	19.69	0.27	5.88
Oxygen	8	3764	1.28	1.38	4.07	0.07	5.47
Aluminium	13	5128	1.03	1.11	1.95	0.05	5.20
Chlorine	17	1790	0.19	0.21	0.28	0.01	7.68
Nickel	28	321828	83.18	89.89	72.24	1.51	1.82
Copper	29	6662	2.21	2.39	1.77	0.06	2.90
		Sum	**92.53**	**100.00**	**100.00**		

(***8***)

9_20kV

Element	At. No.	Netto	Mass [%]	Mass Norm. [%]	Atom [%]	abs. error [%] (1 sigma)	rel. error [%] (1 sigma)
Carbon	6	4696	6.11	6.53	24.46	0.35	5.78
Oxygen	8	4462	1.61	1.72	4.83	0.09	5.37
Aluminium	13	2419	0.46	0.49	0.82	0.03	6.78
Chlorine	17	1931	0.20	0.22	0.28	0.01	7.31
Nickel	28	309368	83.46	89.26	68.36	1.54	1.85
Copper	29	4853	1.66	1.77	1.25	0.05	3.29
		Sum	**93.49**	**100.00**	**100.00**		

(***9***)

10_20kV

Element	At. No.	Netto	Mass [%]	Mass Norm. [%]	Atom [%]	abs. error [%] (1 sigma)	rel. error [%] (1 sigma)
Carbon	6	3678	4.96	5.32	20.87	0.29	5.89
Oxygen	8	3126	1.13	1.21	3.58	0.06	5.73
Aluminium	13	2413	0.47	0.50	0.87	0.03	6.76
Chlorine	17	1801	0.19	0.21	0.28	0.01	7.70
Nickel	28	309659	85.23	91.37	73.38	1.58	1.85
Copper	29	3722	1.30	1.39	1.03	0.05	3.83
		Sum	**93.28**	**100.00**	**100.00**		

(***10***)

11_20kV

Element	At. No.	Netto	Mass [%]	Mass Norm. [%]	Atom [%]	abs. error [%] (1 sigma)	rel. error [%] (1 sigma)
Carbon	6	2730	3.68	3.94	16.14	0.22	5.96
Oxygen	8	2981	1.04	1.12	3.43	0.06	5.75
Aluminium	13	3484	0.70	0.75	1.38	0.04	5.84
Chlorine	17	1133	0.12	0.13	0.18	0.01	11.65
Nickel	28	322031	87.18	93.38	78.34	1.60	1.84
Copper	29	1861	0.64	0.69	0.53	0.04	6.03
		Sum	**93.37**	**100.00**	**100.00**		

(***11***)

12_20kV

Element	At. No.	Netto	Mass [%]	Mass Norm. [%]	Atom [%]	abs. error [%] (1 sigma)	rel. error [%] (1 sigma)
Carbon	6	4151	5.55	5.92	22.95	0.33	5.91
Oxygen	8	2410	0.88	0.94	2.73	0.05	6.15
Aluminium	13	2993	0.57	0.61	1.05	0.04	6.19
Chlorine	17	1252	0.14	0.14	0.19	0.02	15.27
Nickel	28	305567	83.71	89.41	70.90	1.56	1.86
Copper	29	7889	2.78	2.97	2.18	0.08	2.72
		Sum	**93.62**	**100.00**	**100.00**		

(***12***)

13_20kV

Element	At. No.	Netto	Mass [%]	Mass Norm. [%]	Atom [%]	abs. error [%] (1 sigma)	rel. error [%] (1 sigma)
Carbon	6	4059	5.38	5.70	22.13	0.31	5.84
Oxygen	8	3068	1.10	1.17	3.41	0.06	5.75
Aluminium	13	2952	0.58	0.61	1.06	0.04	6.21
Chlorine	17	1490	0.16	0.17	0.23	0.01	8.81
Nickel	28	314347	85.28	90.49	71.82	1.57	1.84
Copper	29	5027	1.75	1.85	1.36	0.06	3.23
		Sum	**94.25**	**100.00**	**100.00**		

(***13***)

14_20kV

Element	At. No.	Netto	Mass [%]	Mass Norm. [%]	Atom [%]	abs. error [%] (1 sigma)	rel. error [%] (1 sigma)
Carbon	6	4266	6.18	6.45	24.48	0.36	5.88
Oxygen	8	2833	1.14	1.19	3.38	0.07	5.97
Aluminium	13	2120	0.41	0.43	0.72	0.03	7.20
Chlorine	17	2181	0.25	0.26	0.33	0.02	6.61
Nickel	28	290426	86.77	90.55	70.28	1.64	1.89
Copper	29	2823	1.08	1.12	0.81	0.05	4.44
		Sum	**95.82**	**100.00**	**100.00**		

(***14***)

15_20kV

Element	At. No.	Netto	Mass [%]	Mass Norm. [%]	Atom [%]	abs. error [%] (1 sigma)	rel. error [%] (1 sigma)
Carbon	6	3810	5.44	5.75	22.30	0.32	5.91
Oxygen	8	2856	1.11	1.18	3.42	0.07	5.91
Aluminium	13	1767	0.35	0.37	0.64	0.03	7.83
Chlorine	17	1371	0.15	0.16	0.22	0.01	9.36
Nickel	28	295982	86.73	91.64	72.76	1.63	1.88
Copper	29	2276	0.85	0.90	0.66	0.04	5.09
		Sum	**94.64**	**100.00**	**100.00**		

(***15***)

16_20kV

Element	At. No.	Netto	Mass [%]	Mass Norm. [%]	Atom [%]	abs. error [%] (1 sigma)	rel. error [%] (1 sigma)
Carbon	6	4121	5.93	6.18	23.25	0.34	5.73
Oxygen	8	5052	2.00	2.09	5.90	0.11	5.26
Aluminium	13	1697	0.32	0.33	0.55	0.03	8.12
Chlorine	17	1896	0.21	0.22	0.28	0.02	7.34
Nickel	28	284156	84.76	88.42	68.05	1.60	1.89
Copper	29	6991	2.65	2.76	1.96	0.08	2.84
		Sum	**95.86**	**100.00**	**100.00**		

(***16***)

17_20kV

Element	At. No.	Netto	Mass [%]	Mass Norm. [%]	Atom [%]	abs. error [%] (1 sigma)	rel. error [%] (1 sigma)
Carbon	6	4012	5.65	5.93	22.66	0.33	5.78
Oxygen	8	4150	1.60	1.68	4.83	0.09	5.39
Aluminium	13	1751	0.35	0.37	0.62	0.03	7.89
Chlorine	17	927	0.10	0.11	0.14	0.01	12.10
Nickel	28	294166	85.60	89.91	70.31	1.60	1.87
Copper	29	5131	1.91	2.00	1.45	0.06	3.22
		Sum	**95.21**	**100.00**	**100.00**		

(***17***)

18_20kV

Element	At. No.	Netto	Mass [%]	Mass Norm. [%]	Atom [%]	abs. error [%] (1 sigma)	rel. error [%] (1 sigma)
Carbon	6	4052	5.86	6.14	23.32	0.34	5.78
Oxygen	8	4021	1.61	1.68	4.79	0.09	5.44
Aluminium	13	1359	0.26	0.27	0.46	0.03	9.97
Chlorine	17	894	0.10	0.10	0.13	0.01	12.42
Nickel	28	287680	86.33	90.33	70.24	1.64	1.89
Copper	29	3673	1.42	1.48	1.07	0.05	3.78
		Sum	**95.58**	**100.00**	**100.00**		

(***18***)

19_20kV

Element	At. No.	Netto	Mass [%]	Mass Norm. [%]	Atom [%]	abs. error [%] (1 sigma)	rel. error [%] (1 sigma)
Carbon	6	3944	5.75	6.05	23.32	0.35	6.07
Oxygen	8	2685	1.08	1.13	3.28	0.06	5.96
Aluminium	13	1191	0.22	0.23	0.40	0.02	10.00
Chlorine	17	935	0.11	0.11	0.14	0.01	11.81
Nickel	28	286310	86.14	90.64	71.52	1.63	1.90
Copper	29	4529	1.74	1.83	1.34	0.06	3.43
		Sum	**95.03**	**100.00**	**100.00**		

(***19***)

Figure 5. Elemental composition of Ni coatings electrodeposited from the Ethalinebased electrolyte under different conditions. Sample numbers correspond to the electrodeposition parameters listed in Table 1.

Surface analysis indicated that variations in temperature and current density had almost no effect on the chemical composition of the coating surfaces. As expected, nickel was identified as the main component. In addition, the coatings contained approximately 5–6 wt.% carbon, 1–2 wt.% oxygen, some amount of copper originating from the substrate, and trace amounts of chlorine derived from the choline chloride present in the electrolyte. The detected carbon is also attributed to the organic components of the Ethaline-based electrolyte. Importantly, no significant influence of the deposition parameters on the elemental composition of the coating surfaces was observed.

An efficient strategy to modify the surface composition of Ni coatings for improved HER catalysis is the incorporation of nanoparticles of transition metal sulfides, phosphides, or nitrides during electrodeposition, resulting in composite coatings with a nickel matrix. In the present work, MoS_2 and M-Xene nanoparticles were selected as the catalytic additive due to their well-known high activity toward HER. Additionally, C-MoFeNiP catalysts were examined.

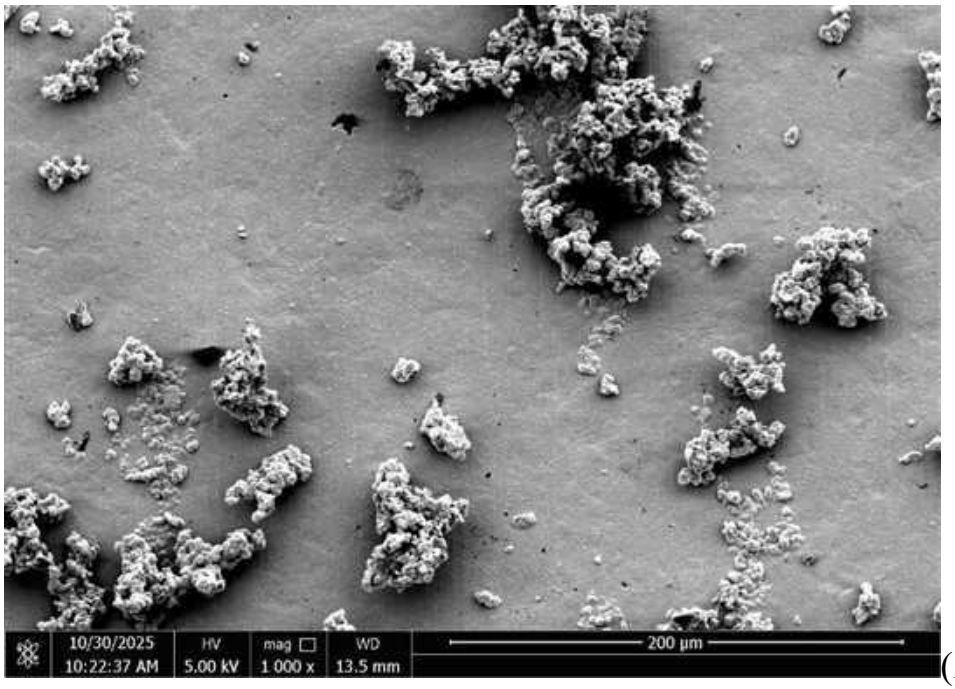
1.2 Surface morphology, topography and chemical composition of Ni/MoS_2 coatings deposited from DES-based electrolyte

The electrodeposition conditions employed for the preparation of Ni/MoS_2 composite coatings are summarized in Table 2. The coatings were deposited at different current densities (i), ranging from 5 to 25 mA/cm², while the deposition temperature (t) and duration (τ) were maintained constant at 40 °C and 20 min, respectively. These conditions were selected to evaluate the influence of current density on the formation and properties of the resulting Ni/MoS_2 composite coatings.

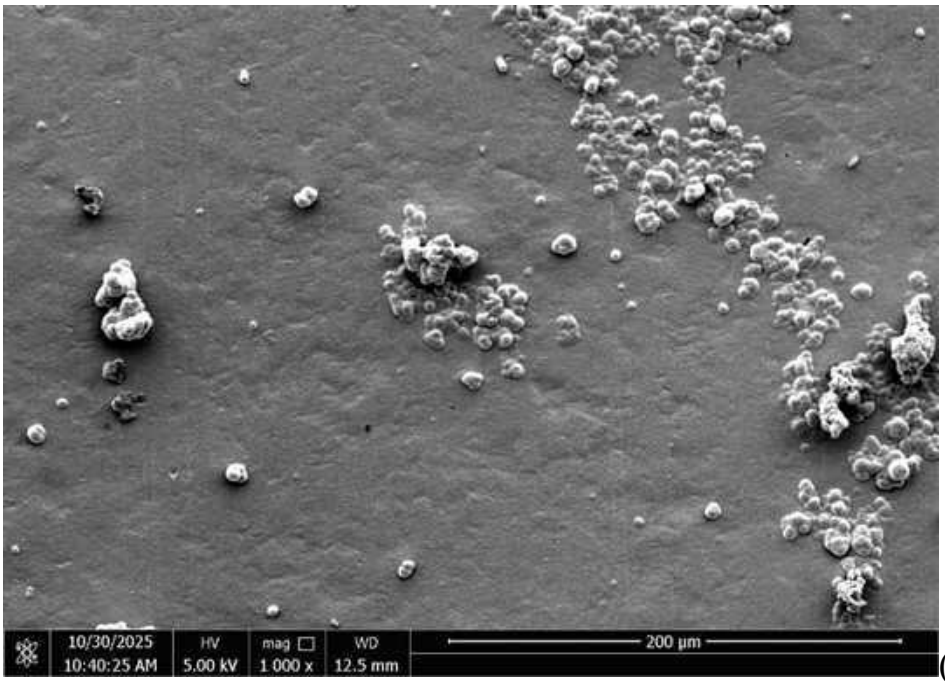
SEM images of samples (***1***) – (***5***) are presented in Figures 6-8 that represent surfaces under different magnifications.

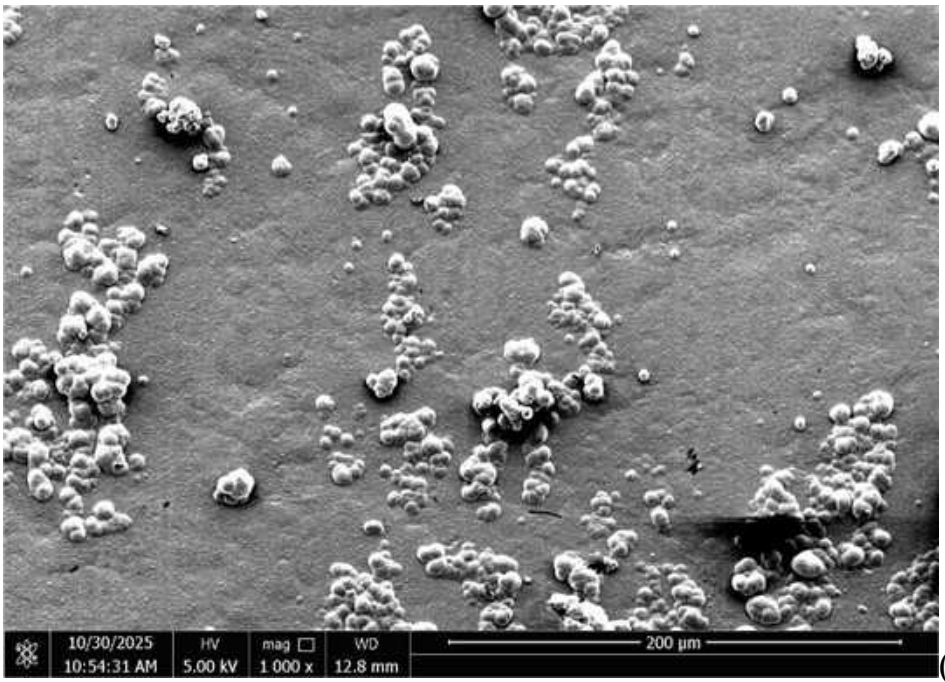
Table 2. Electrodeposition conditions for Ni/MoS_2 composite coatings.

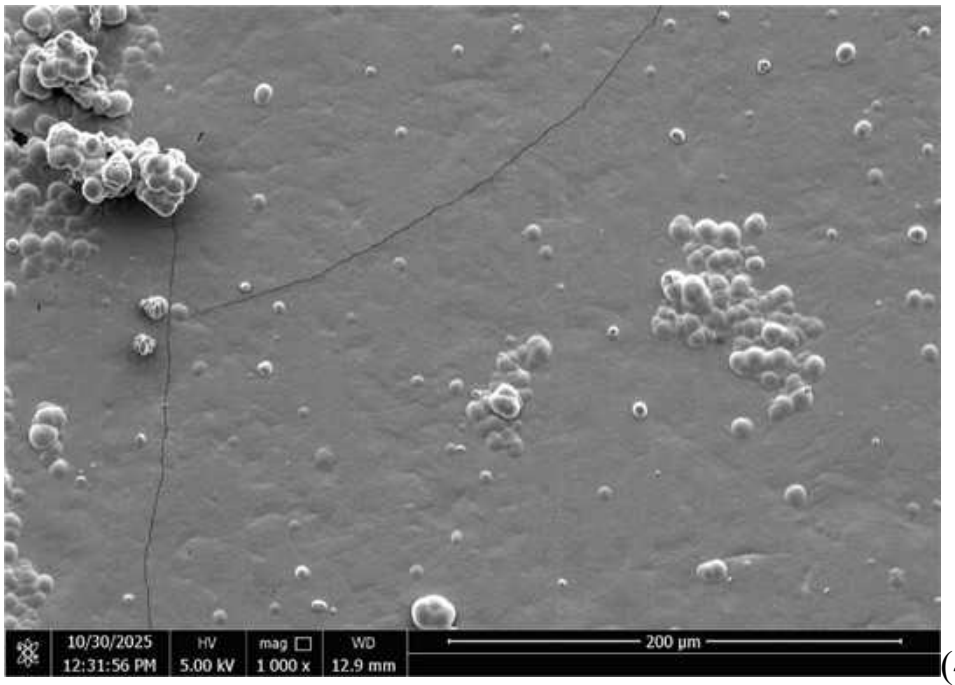
Sample	**j, mA/cm^2**	**t, ^{o}C**	**τ, min**
1	5	40	20
2	10		
3	15		
4	20		
5	25		



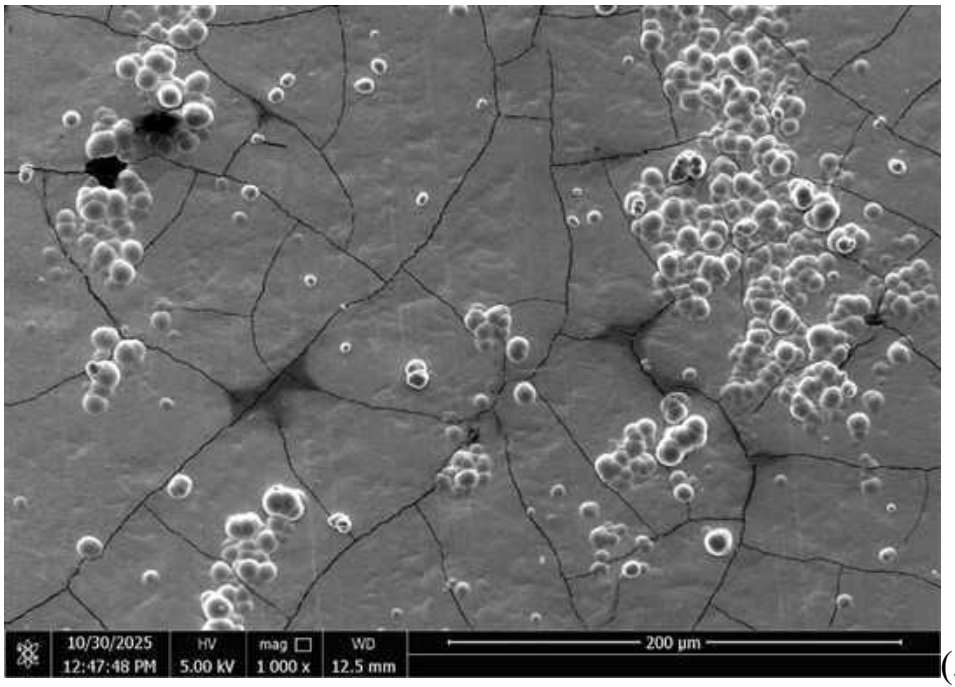
(***1***)


10/30/2025
10:40:25 AM
HV
5.00 kV
mag
1 000 x
WD
12.5 mm
200 µm
(*2*)


10/30/2025
10:54:31 AM
HV
5.00 kV
mag
1 000 x
WD
12.8 mm
200 µm
(*3*)



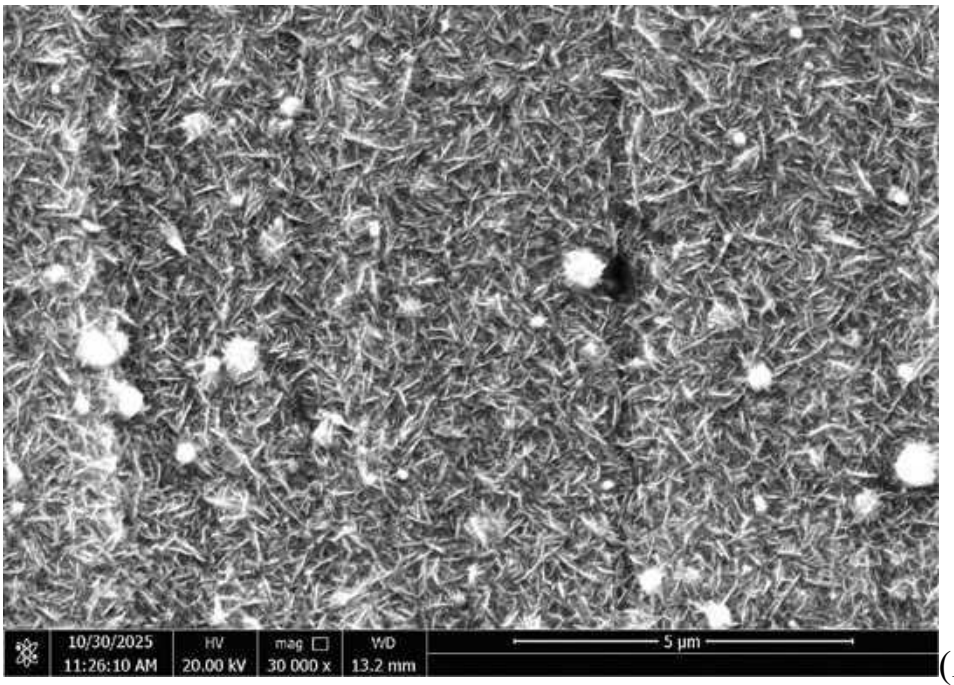
(*4*)

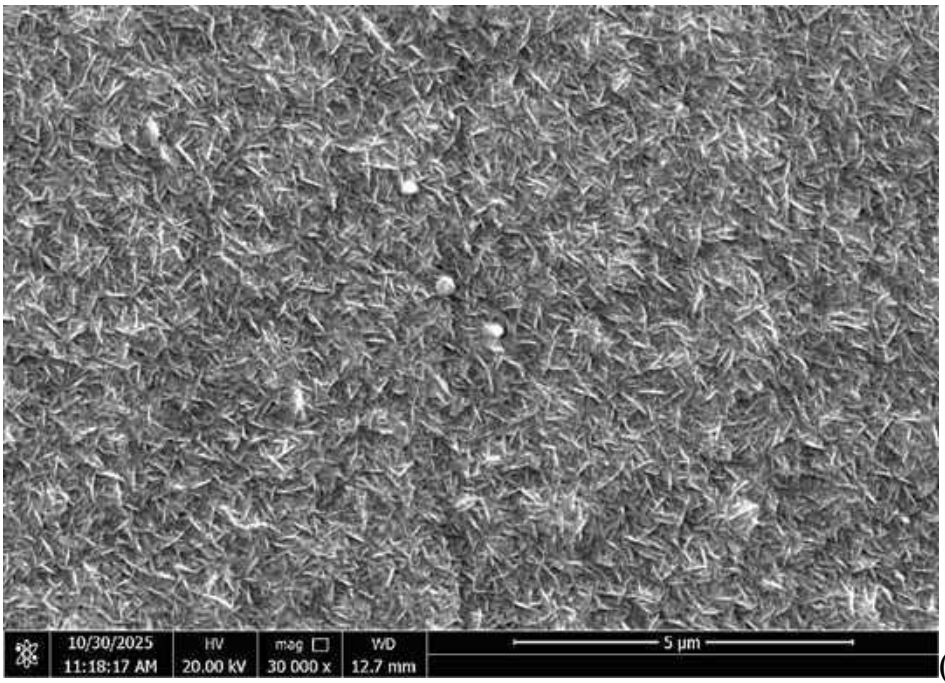


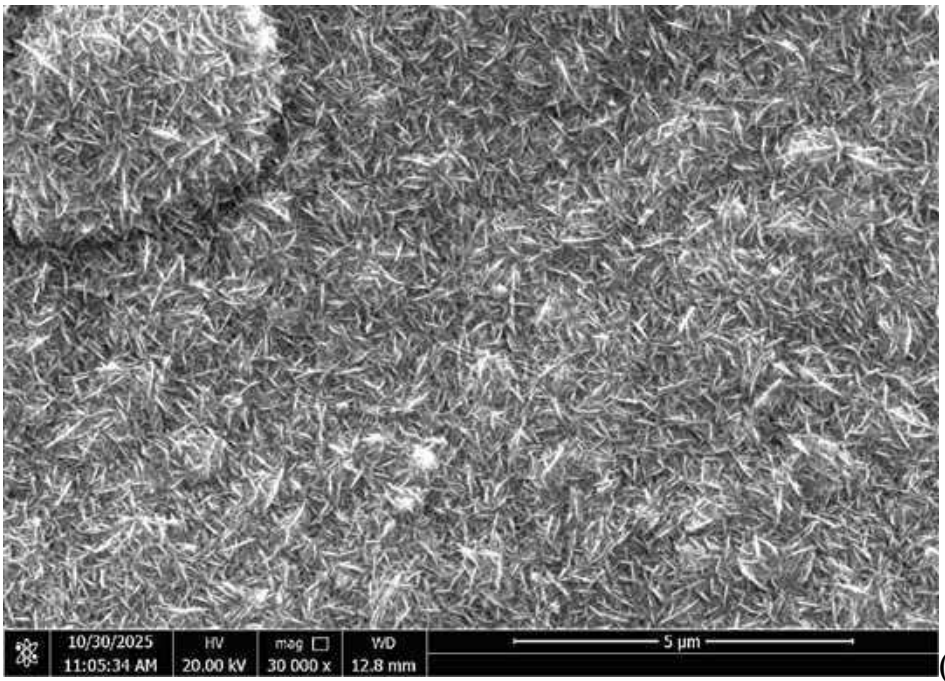
(*5*)

Figure 6. SEM images of Ni/MoS_2 coatings electrodeposited from the Ethalinebased electrolyte at 40 °C for 20 min under different current densities.

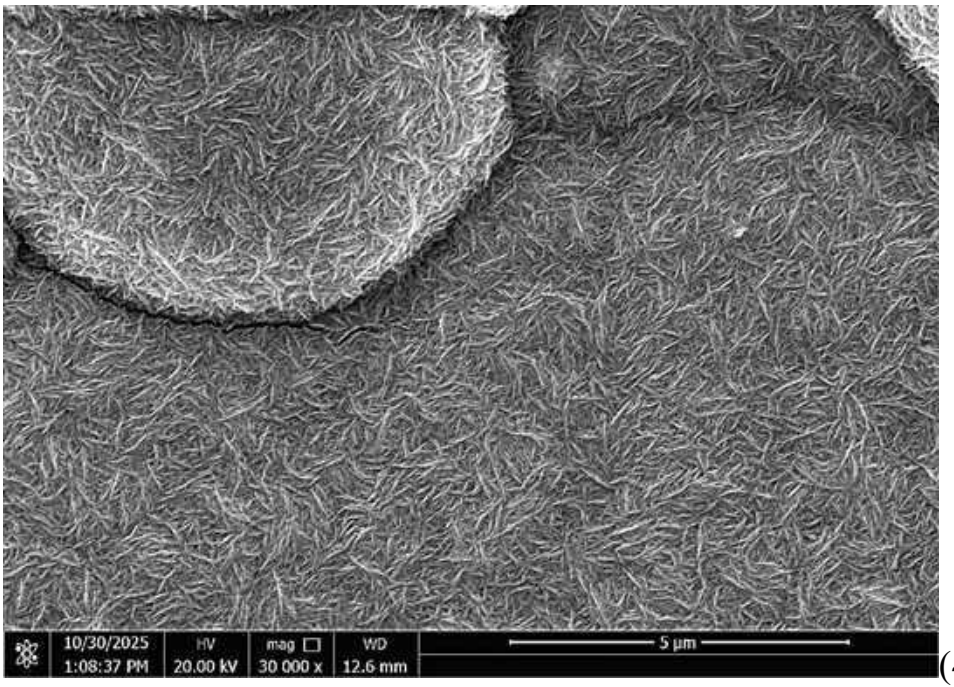
Magnification: 1k×; scale bar: 200 µm. Sample numbers correspond to the electrodeposition parameters listed in Table 2.


10/30/2025
11:26:10 AM
HV
20.00 kV
mag
30 000 x
WD
13.2 mm
5 µm
(*1*)

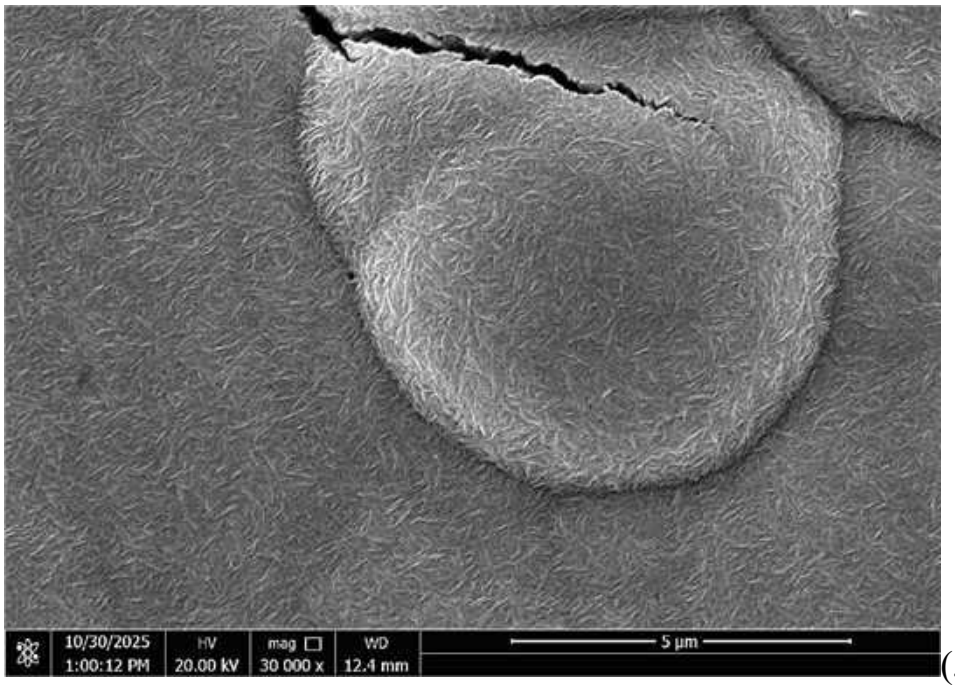

10/30/2025
11:18:17 AM
HV
20.00 kV
mag
30 000 x
WD
12.7 mm
5 µm
(*2*)


10/30/2025
11:05:34 AM
HV
20.00 kV
mag
30 000 x
WD
12.8 mm
5 µm

(***3***)


10/30/2025
1:08:37 PM
HV
20.00 kV
mag
30 000 x
WD
12.6 mm
5 µm

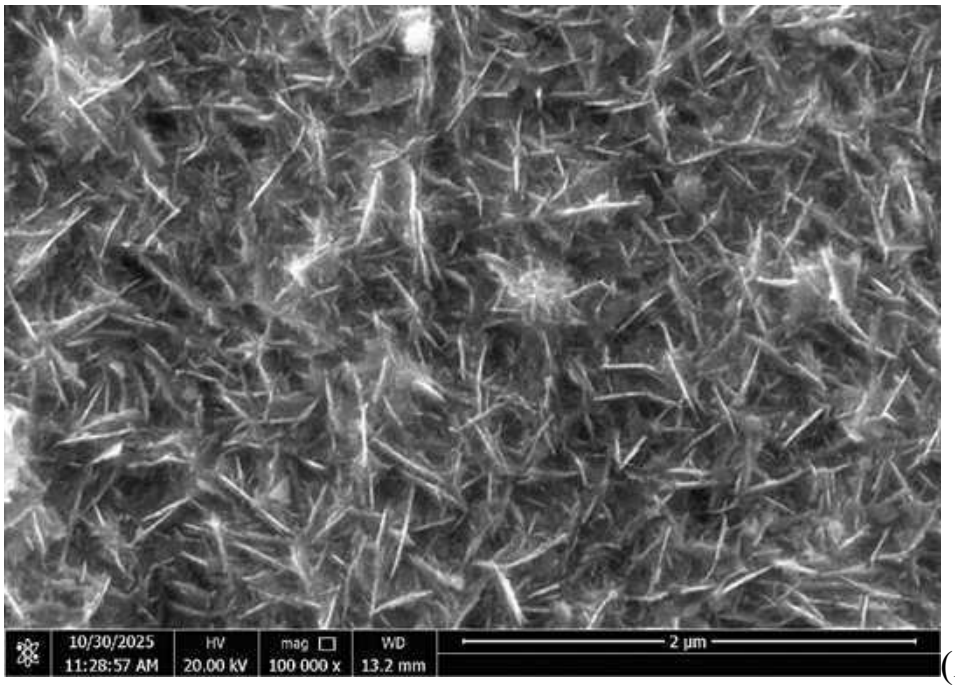
(***4***)

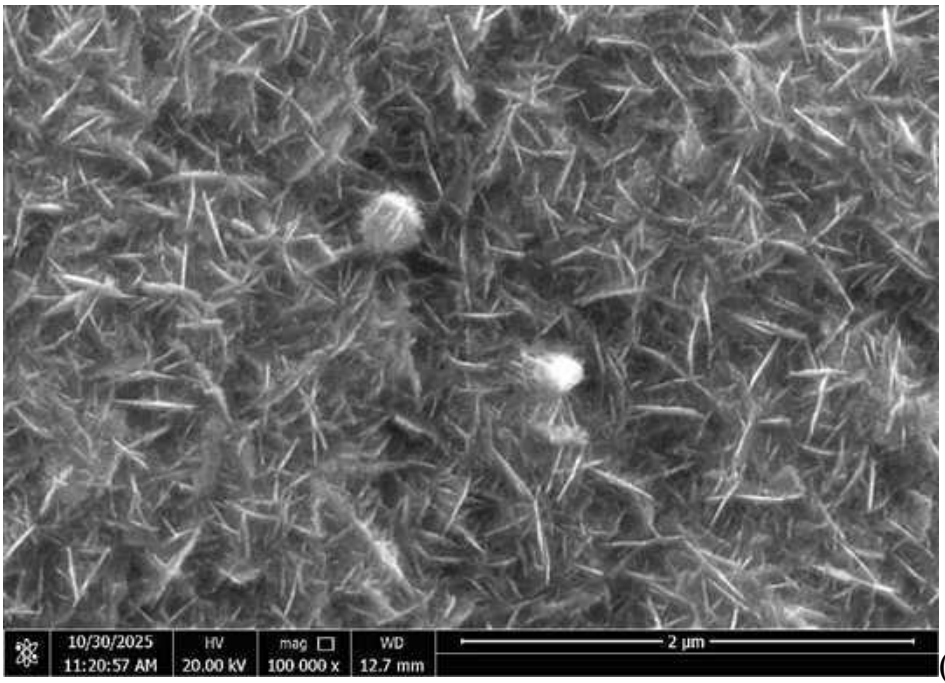


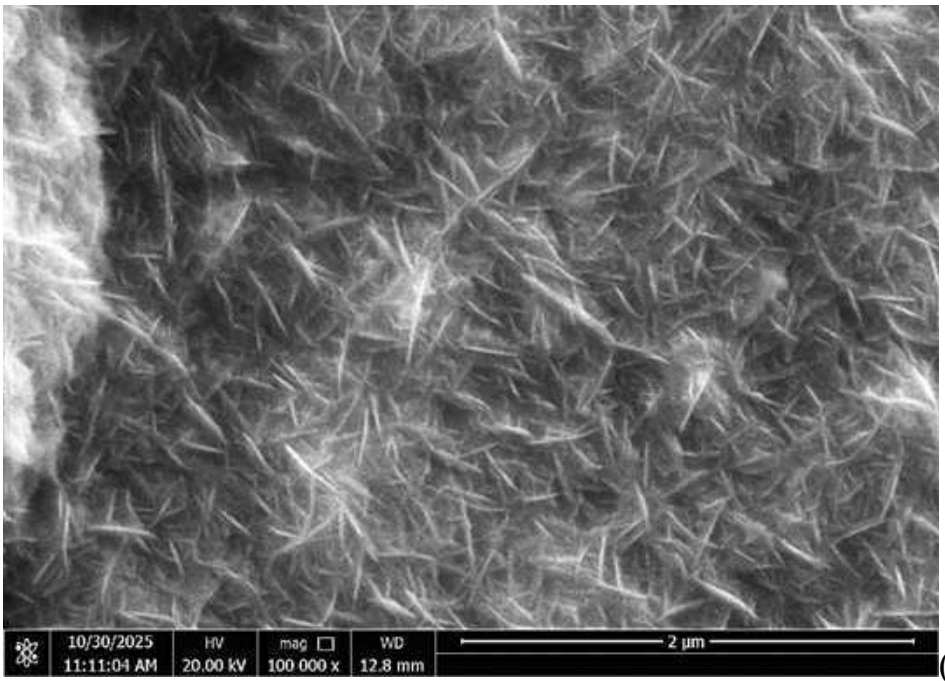
(***5***)

Figure 7. SEM images of Ni/MoS_2 coatings electrodeposited from the Ethalinebased electrolyte at 40 °C for 20 min under different current densities.

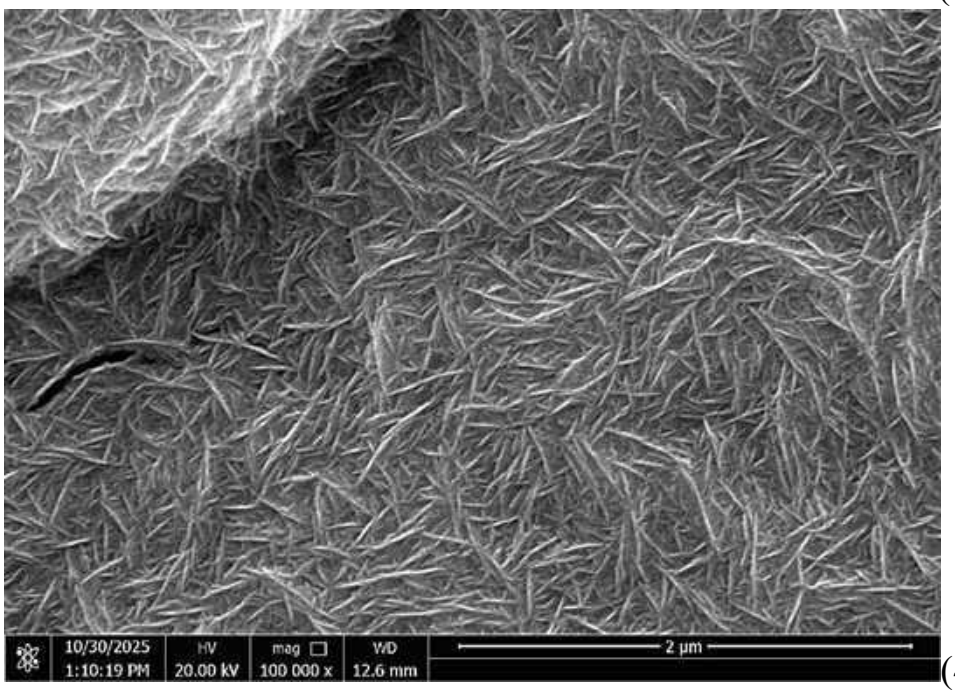
Magnification: 30k×; scale bar: 5 µm. Sample numbers correspond to the electrodeposition parameters listed in Table 2.


10/30/2025
11:28:57 AM
HV
20.00 kV
mag
100 000 x
WD
13.2 mm
2 µm
(*1*)

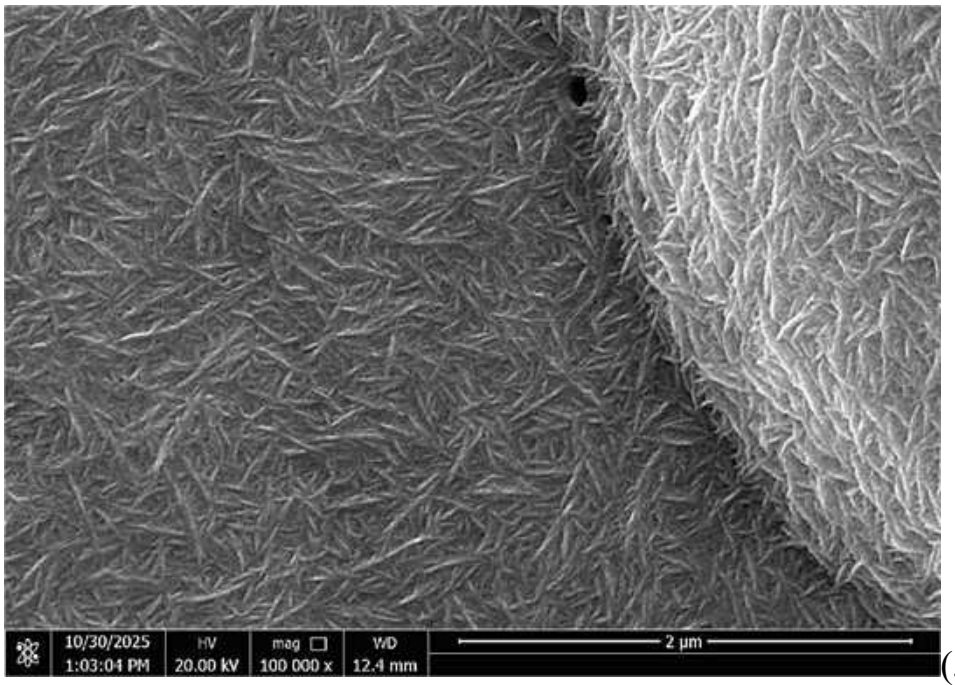

10/30/2025
11:20:57 AM
HV
20.00 kV
mag
100 000 x
WD
12.7 mm
2 µm
(*2*)


10/30/2025
11:11:04 AM
HV
20.00 kV
mag
100 000 x
WD
12.8 mm
2 µm

(*3*)


10/30/2025
1:10:19 PM
HV
20.00 kV
mag
100 000 x
WD
12.6 mm
2 µm

(*4*)



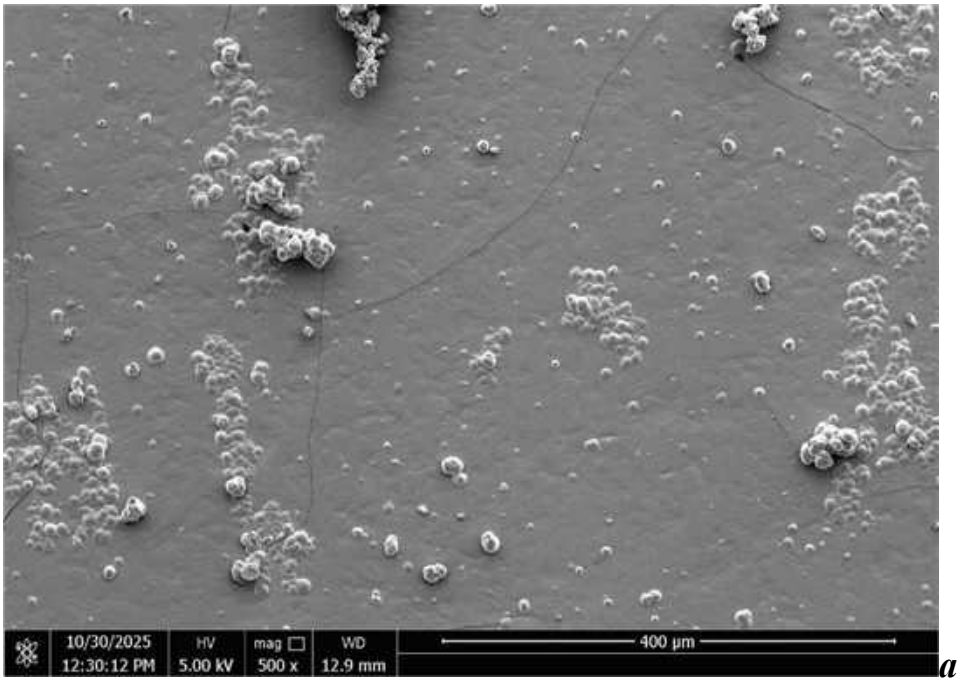
(*5*)

Figure 8. SEM images of Ni/MoS_2 coatings electrodeposited from the Ethalinebased electrolyte at 40 °C for 20 min under different current densities.
Magnification: 100k×; scale bar: 2 µm. Sample numbers correspond to the electrodeposition parameters listed in Table 2.

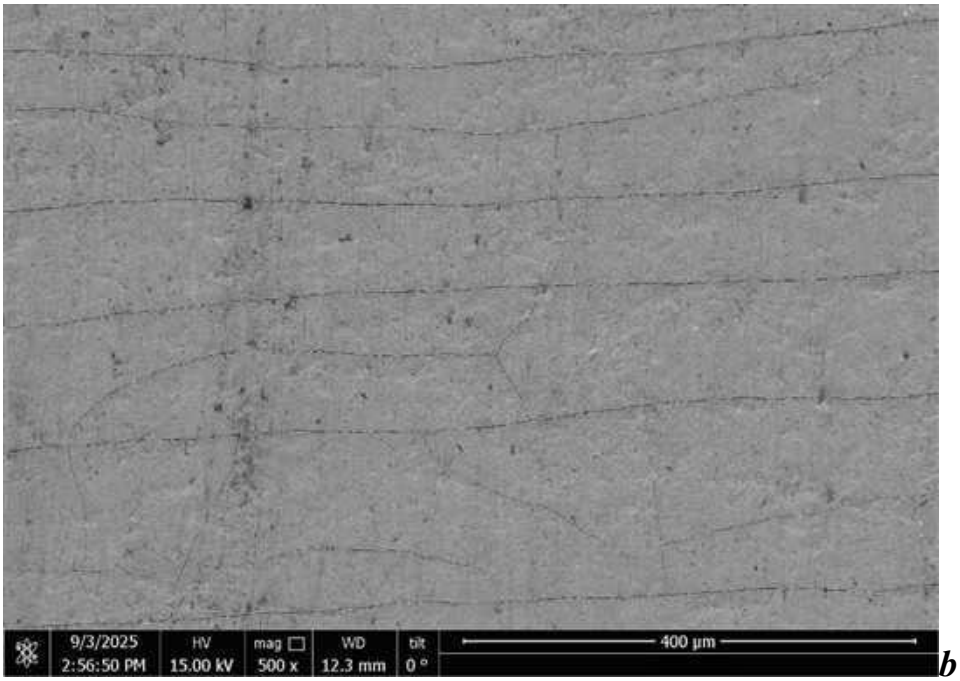
As shown in Fig. 6, which presents the coating surfaces at the lowest magnification, Ni/MoS_2 composite coatings electrodeposited at current densities of 20 mA cm^{-2} and higher exhibit cracks similar to those observed in pure Ni coatings, although their number and severity are reduced in the presence of MoS_2 particles. The formation of cracks at high current densities can be attributed to the accumulation of internal stresses during rapid deposition, while the incorporation of MoS_2 particles appears to mitigate these stresses, resulting in fewer cracks.

Admit that Ni/MoS_2 coating surfaces display islands of hemispherical features, with diameters that increase as the current density rises (Fig. 6). These hemispherical structures likely result from localized rapid Ni deposition around nucleation sites, where faster metal ion reduction at higher current densities favors the growth of

larger deposits. The incorporation of MoS_2 particles may also influence this morphology by acting as preferential nucleation centers, locally modifying the deposition rate. As demonstrated in Figure 9, such hemispherical features are absent in pure Ni coatings, confirming the role of MoS_2 particles in their formation.



a



b

Figure 9. SEM images of Ni/MoS_2 coating (a) and Ni (b) electrodeposited from the Ethaline-based electrolyte at 40 °C for 20 min under current density 20 mA cm^{-2}. Magnification: 500×; scale bar: 400 μm.

Figures 7 and 8 reveal that the Ni/MoS_2 coatings exhibit the same lamellar structure as observed for pure Ni coatings. It is evident, however, that the Ni/MoS_2 coatings possess a more pronounced hierarchical architecture, combining micro- and nanoscale structural features. Such a combination may positively influence the catalytic properties of the MoS_2-containing coatings, not only due to changes in their chemical composition and related factors but also as a result of the observed morphological variations.

For Ni and Ni/MoS_2 coatings, it was observed that layers with a thickness of 7–12 μm, deposited at high current densities (≥20 mA cm^{-2}), tend to develop cracks due to the accumulation of internal stresses (Figure 10). As previously discussed, the incorporation of MoS_2 slightly mitigates this effect, suggesting that a further increase in the MoS_2 content could reduce the tendency toward cracking by enhancing coating ductility and facilitating stress relaxation.

To further reduce internal stresses and prevent crack formation, several strategies can be implemented. Optimizing deposition parameters is especially crucial. For preparing thick Ni or Ni/MoS_2 coatings (>10 μm), applying lower current densities (<20 mA cm^{-2}) and extending the deposition time promotes more consistent growth and minimizes stress accumulation. Adding surfactants or stress-relief additives such as sodium dodecyl sulfate, saccharin, or polyethylene glycol to the electrolyte can also enhance coating uniformity and decrease internal stresses. Another effective technique involves using pulse or pulse-reverse electrodeposition, which improves ion transport and provides better control over the microstructure of the coating,

thereby reducing residual stress. Lastly, moderate post-deposition annealing can further alleviate internal stresses without compromising the coating's mechanical integrity or surface quality.

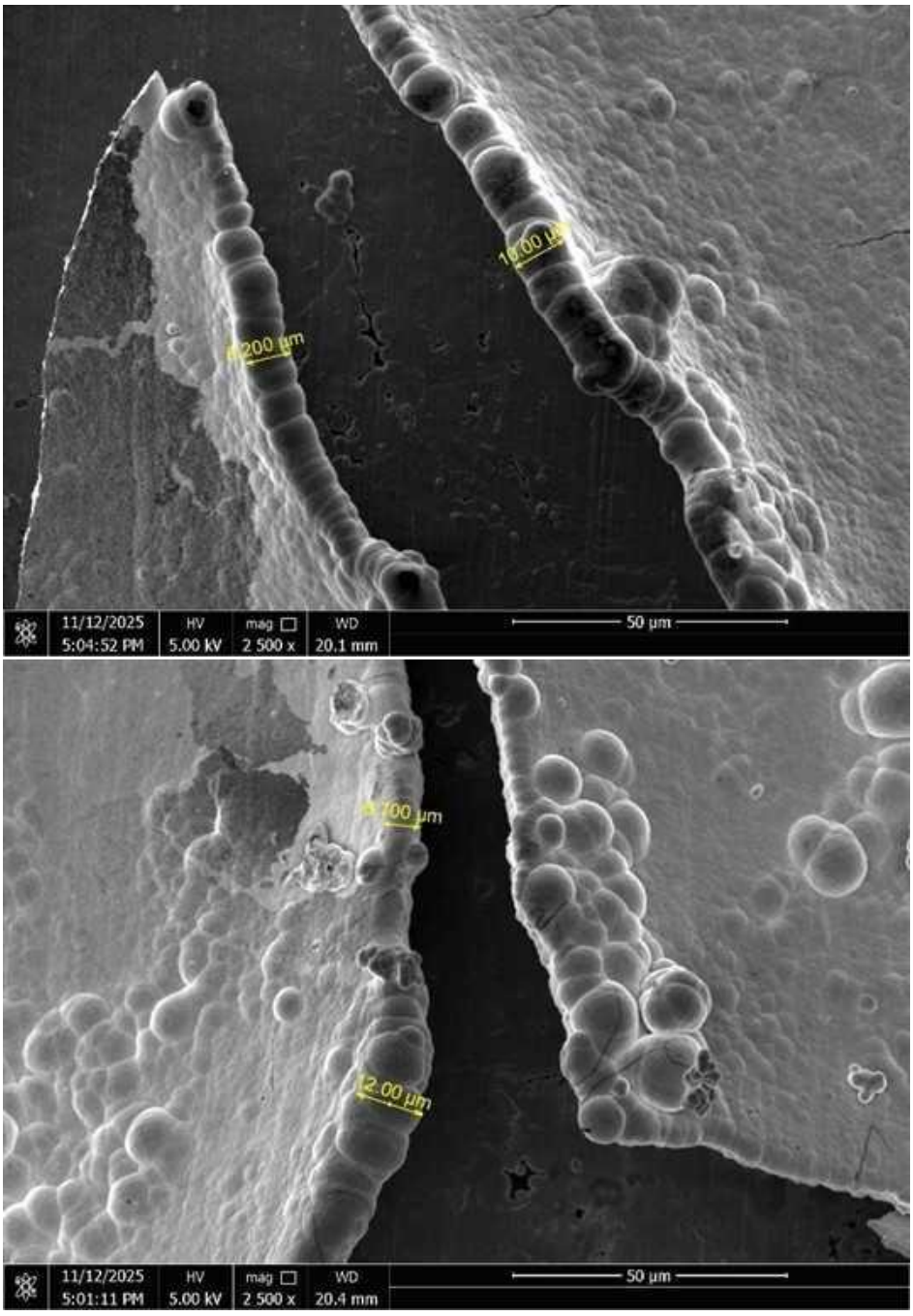


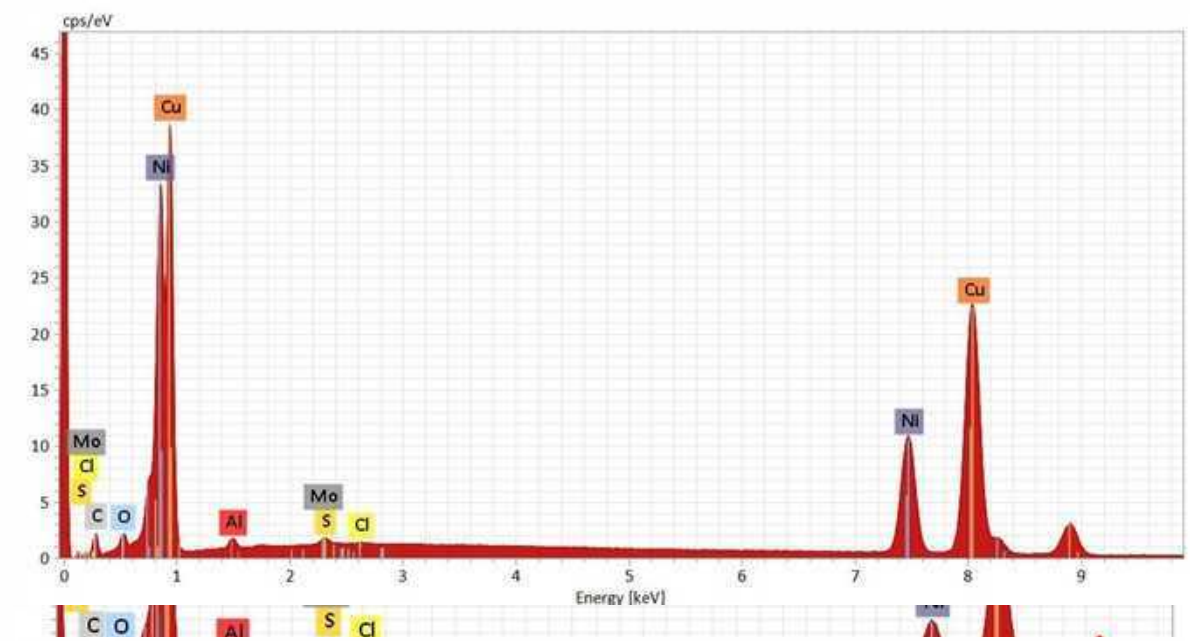
Figure 10. SEM images of Ni/MoS_2 coating electrodeposited from the Ethalinebased electrolyte at 40 °C for 20 min under a current density of 20 mA cm^{-2}.
Magnification: 2500×; scale bar: 50 µm.

In addition to surface morphology and topography, the chemical composition of the Ni/MoS_2 composite coatings was investigated to confirm the incorporation of MoS_2 particles into the electrodeposited Ni matrix and to evaluate the influence of deposition current density on the surface composition. The EDX spectra obtained for Ni/MoS_2 coatings deposited at different current densities are presented in Figure 11, while the corresponding quantitative elemental compositions are summarized in Figure 12.

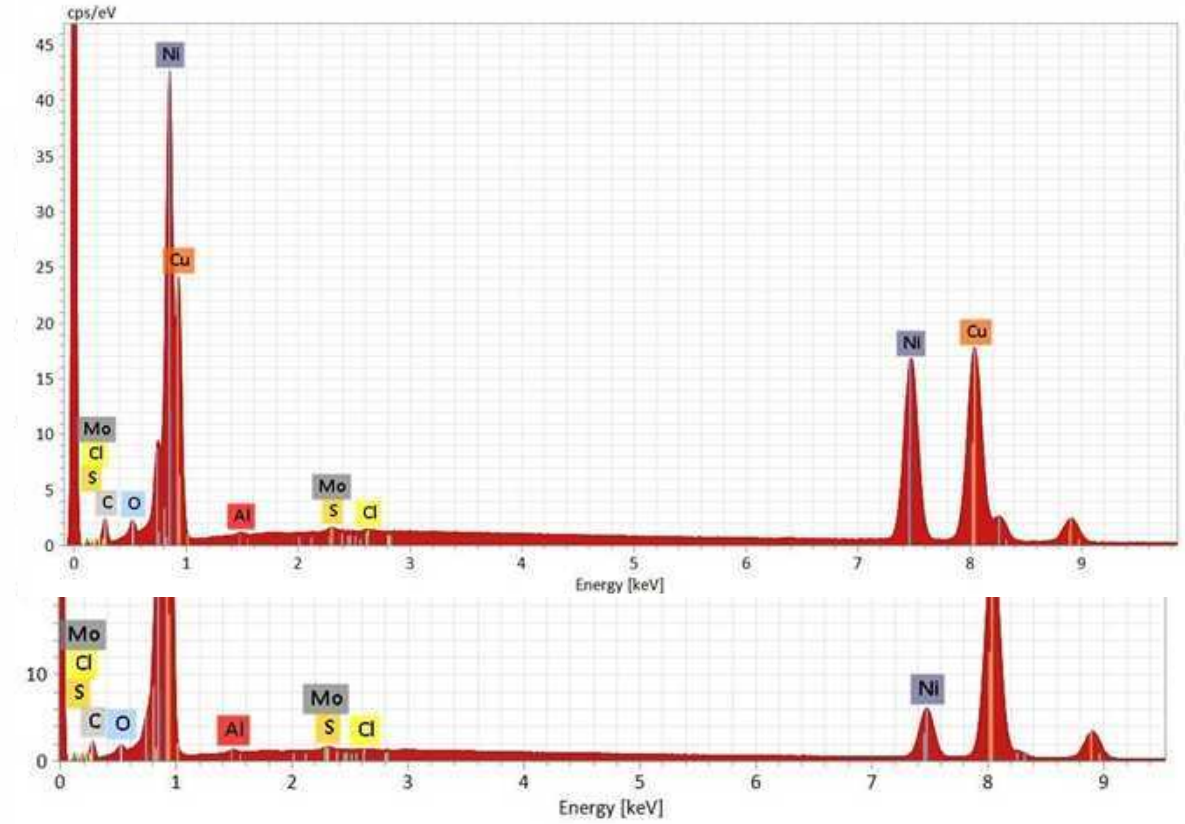
(1)

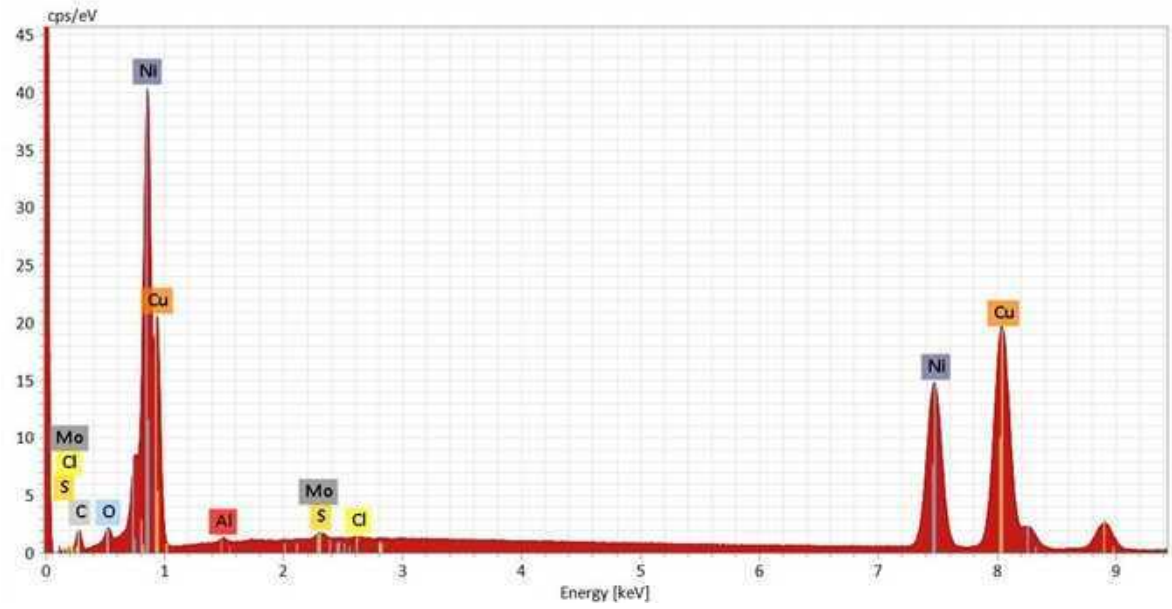
(2)

(3)


cps/eV
Cu
Ni
Mo
Cl
S
C
O
Al
Mo
S
Cl
Ni
Cu
Energy [keV]

(4)


cps/eV
Ni
Cu
Mo
Cl
S
C
O
Al
Mo
S
Cl
Ni
Cu
Energy [keV]
Mo
Cl
S
C
O
Al
Mo
S
Cl
Ni
Energy [keV]



(5)

Figure 11. EDX spectra of Ni/MoS_2 coatings electrodeposited from the Ethalinebased electrolyte under various conditions. Sample numbers correspond to the electrodeposition parameters listed in Table 2.

Element	At. No.	Netto	Mass [%]	Mass Norm. [%]	Atom [%]	abs. error [%] (1 sigma)	rel. error [%] (1 sigma)
Carbon	6	16202	6.06	6.27	25.38	0.34	5.56
Oxygen	8	6724	0.70	0.72	2.19	0.04	5.49
Aluminium	13	2247	0.12	0.13	0.23	0.01	9.57
Sulfur	16	20424	0.65	0.67	1.01	0.04	5.75
Chlorine	17	1146	0.03	0.04	0.05	0.01	17.02
Nickel	28	163902	11.58	11.98	9.92	0.16	1.42
Copper	29	784178	77.01	79.68	60.96	1.04	1.35
Molybdenum	42	9601	0.50	0.52	0.26	0.10	19.36
		Sum	**96.65**	**100.00**	**100.00**		

(1)

(2)

Element	At. No.	Netto	Mass [%]	Mass Norm. [%]	Atom [%]	abs. error [%] (1 sigma)	rel. error [%] (1 sigma)
Carbon	6	16422	6.20	6.33	25.66	0.34	5.47
Oxygen	8	5651	0.59	0.60	1.84	0.03	5.63
Aluminium	13	4752	0.25	0.26	0.47	0.02	6.15
Sulfur	16	4480	0.14	0.14	0.22	0.03	18.23
Chlorine	17	1431	0.04	0.04	0.06	0.01	14.02
Nickel	28	172608	12.52	12.79	10.61	0.17	1.34
Copper	29	778442	78.00	79.64	61.04	1.04	1.34
Molybdenum	42	3721	0.19	0.19	0.10	0.06	32.40
		Sum	**97.94**	**100.00**	**100.00**		

(3)

Element	At. No.	Netto	Mass [%]	Mass Norm. [%]	Atom [%]	abs. error [%] (1 sigma)	rel. error [%] (1 sigma)
Carbon	6	16542	5.90	6.14	24.56	0.32	5.47
Oxygen	8	9551	0.94	0.98	2.94	0.05	5.19
Aluminium	13	11683	0.66	0.69	1.23	0.03	4.42
Sulfur	16	7398	0.24	0.25	0.38	0.03	11.53
Chlorine	17	2441	0.07	0.08	0.11	0.01	14.02
Nickel	28	315290	21.93	22.82	18.68	0.28	1.29
Copper	29	698110	66.08	68.79	52.00	0.87	1.32
Molybdenum	42	4385	0.24	0.24	0.12	0.08	32.26
		Sum	**96.06**	**100.00**	**100.00**		

(4)

Element	At. No.	Netto	Mass [%]	Mass Norm. [%]	Atom [%]	abs. error [%] (1 sigma)	rel. error [%] (1 sigma)
Carbon	6	17878	6.14	6.64	26.05	0.34	5.46
Oxygen	8	9363	0.90	0.97	2.87	0.05	5.19
Aluminium	13	2634	0.14	0.16	0.27	0.01	8.42
Sulfur	16	3611	0.12	0.13	0.19	0.03	24.74
Chlorine	17	3229	0.10	0.11	0.14	0.01	7.61
Nickel	28	496428	34.30	37.06	29.78	0.44	1.27
Copper	29	545397	50.57	54.65	40.56	0.67	1.32
Molybdenum	42	5027	0.27	0.29	0.14	0.06	21.64
		Sum	**92.54**	**100.00**	**100.00**		

Element	At. No.	Netto	Mass [%]	Mass Norm. [%]	Atom [%]	abs. error [%] (1 sigma)	rel. error [%] (1 sigma)
Carbon	6	14793	5.28	5.58	22.74	0.30	5.60
Oxygen	8	8802	0.86	0.91	2.77	0.04	5.24
Aluminium	13	4511	0.25	0.27	0.48	0.02	6.25
Sulfur	16	6312	0.21	0.22	0.33	0.03	13.36
Chlorine	17	2571	0.08	0.08	0.12	0.01	14.17
Nickel	28	433948	30.73	32.47	27.07	0.40	1.29
Copper	29	602125	56.99	60.23	46.37	0.76	1.33
Molybdenum	42	4211	0.23	0.24	0.12	0.07	32.18
		Sum	**94.62**	**100.00**	**100.00**		

(5)

Figure 12. Elemental composition of Ni/MoS_2 coatings electrodeposited from the Ethaline-based electrolyte under different conditions. Sample numbers correspond to the electrodeposition parameters listed in Table 2.

The EDX analysis confirms that Ni is the predominant element in all investigated coatings, as expected for a Ni-based composite matrix. The detection of Mo and S provides evidence for the incorporation of MoS_2 particles into the electrodeposited Ni layer. In addition to the principal coating components, the spectra may contain signals associated with the substrate and/or residual species originating from the DES-based electrolyte.

Comparison of samples 1–5 indicates that the elemental composition of the coating surface varies with the applied current density. These variations can be related to changes in the relative rates of Ni electrodeposition and MoS_2 particle incorporation. Increasing the current density accelerates Ni deposition and simultaneously modifies mass transport, particle adsorption, and particle entrapment at the growing electrode surface. Consequently, the amount of MoS_2 incorporated into the Ni matrix is governed by the competition between metal deposition and particle incorporation.

The EDX results presented in Figures 11 and 12 should also be considered together with the morphological observations in Figures 6–10. The presence of MoS_2 in the coating is accompanied by the development of a more pronounced hierarchical micro-/nanostructure compared with pure Ni. Thus, incorporation of MoS_2 modifies both the chemical composition and surface morphology of the electrodeposited coatings, which may be beneficial for their catalytic performance by providing MoS_2-containing active sites together with a structurally developed Ni-based surface.

The EDX results confirm the presence of Mo and S in all investigated samples, demonstrating successful incorporation of the MoS_2-containing phase into the coatings throughout the entire current-density range. The highest contents of both elements were detected in sample 1, deposited at 5 mA cm^{-2}, where the Mo and S contents were approximately 0.52 and 0.67 wt.%, respectively. For sample 2, deposited at 10 mA cm^{-2}, the Mo and S contents decreased to approximately 0.19 and 0.14 wt.%. At 15 mA cm^{-2}, corresponding to sample 3, the measured values increased slightly to approximately 0.24 wt.% Mo and 0.25 wt.% S.

For samples deposited at higher current densities, MoS_2 remained detectable, although no monotonic dependence on current density was observed. Sample 4, obtained at 20 mA cm^{-2}, contained approximately 0.29 wt.% Mo and 0.13 wt.% S, while sample 5, deposited at 25 mA cm^{-2}, contained approximately 0.24 wt.% Mo and 0.22 wt.% S. Thus, except for the relatively high Mo and S contents detected in sample 1, the concentrations of these elements remain within a comparatively narrow range at higher current densities. This indicates that an increase in current density does not lead to a proportional increase in the amount of incorporated MoS_2. Instead,

the particle incorporation process appears to be influenced by the balance between particle transport, adsorption at the electrode surface, and entrapment within the growing metallic layer.

The carbon content remains relatively stable for all investigated samples, ranging from approximately 5.58 to 6.64 wt.%. The measured values were 6.27, 6.33, 6.14, 6.64, and 5.58 wt.% for samples 1–5, respectively. The absence of a systematic variation with current density suggests that the carbon content is only weakly affected by the applied deposition conditions. Its presence is most likely associated with the organic components of the Ethaline-based electrolyte, as was also observed for the pure Ni coatings discussed earlier in the report.

The oxygen concentration is considerably lower than that of carbon and varies between approximately 0.60 and 0.98 wt.%. The lowest oxygen content was detected in sample 2, while samples 3–5 exhibited similar values close to 1 wt.%. As with carbon, no clear monotonic relationship between oxygen content and deposition current density is evident. The relatively small amount of oxygen may be related to surface oxidation and/or oxygen-containing residual species present on the coating surface.

Ni and Cu constitute the major components detected by EDX. Their relative contributions change with deposition current density, mainly reflecting differences in coating growth, thickness, surface coverage, and the contribution of the Cu substrate to the analyzed volume. These changes do not alter the main conclusion regarding the composite phase: Mo and S are consistently detected in all samples.

Overall, Figures 11 and 12 demonstrate that MoS_2 is incorporated into Ni-based coatings over the entire investigated current-density range. The Mo and S contents vary with deposition conditions but do not show a simple monotonic dependence on current density. In contrast, the C and O contents remain comparatively stable,

indicating that their presence is only weakly influenced by the applied current density. The EDX results therefore confirm the formation of Ni/MoS_2 composite coatings while showing that the efficiency of MoS_2 incorporation is governed by more complex factors than the deposition current density alone.

In future experiments, the electrodeposition procedure will be further modified by applying continuous stirring of the electrolyte during deposition, with the aim of enhancing the transport of suspended MoS_2 particles toward the cathode and thereby increasing their incorporation into the growing Ni matrix. Particular attention will be given to the influence of stirring speed on the MoS_2 content of the resulting composite coatings. By systematically varying the stirring rate while maintaining the other electrodeposition parameters constant, the relationship between hydrodynamic conditions, particle incorporation efficiency, and coating characteristics will be established, allowing further optimization of the Ni/MoS_2 electrodeposition process.

1.3 Characterization of MoFeNiP catalysts

The structural and chemical properties of the synthesized MoFeNiP catalysts were examined using several complementary analytical methods. X-ray diffraction (XRD) was employed to identify the crystalline phases formed during thermal treatment. To assess the ordering and defect density of the carbon matrix, Raman spectroscopy was performed. The surface morphology, particle dispersion, and elemental distribution within the materials were investigated using scanning electron microscopy (SEM) coupled with energy-dispersive X-ray spectroscopy (EDX).

SEM images of the obtained MoFeNiP catalysts are presented in Figure 13, together with the corresponding EDX elemental maps. The elemental mapping provides information on the spatial distribution of the constituent elements across

the catalyst surface, enabling assessment of the homogeneity of their distribution within the investigated material.

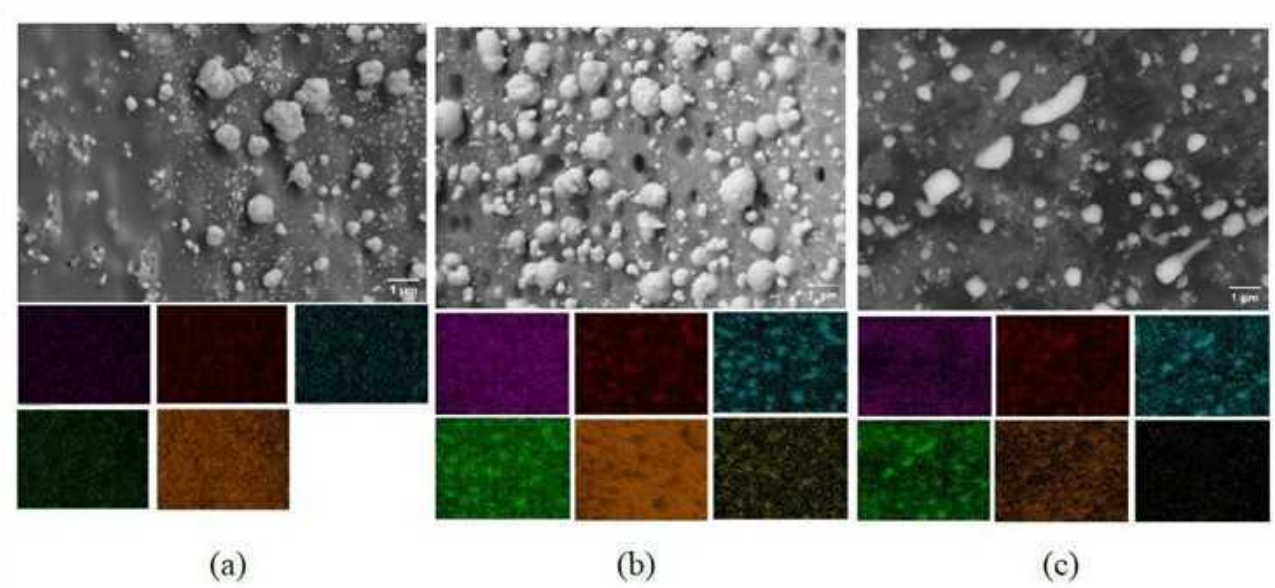


Figure 13. SEM images and corresponding mappings for (a) MoFeNiP-800, (b) MoFeNiP-1000, and (c) MoFeNiP-1200. Elemental distributions are color-labeled as Mo (purple), Fe (red), Ni (blue), P (green), C (orange), and O (yellow). The elemental mapping images correspond to the SEM micrographs shown above (scale bar as indicated).

X-ray diffraction analysis confirmed that all synthesized samples exhibited a combination of crystalline phases, including orthorhombic MoFeP, hexagonal NiMoP, and a graphitic carbon phase (Figure 14). Although the phase composition remained consistent across the series, increasing the pyrolysis temperature enhanced the overall crystallinity of the metal phosphides. This improvement was reflected in sharper and more intense diffraction peaks, indicating better structural ordering and more well-defined phosphide domains at higher temperatures. Raman spectra of all samples displayed the characteristic D band at approximately 1340 cm^{-1} and the G band at around 1586 cm^{-1}, corresponding to disordered and graphitic carbon

structures, respectively (Figure 15). The intensity ratio ID/IG was close to unity for every sample, revealing that the carbon matrix is highly defect-rich and only partially graphitized. Such structural disorder is advantageous for electrocatalytic applications, as it increases the number of edge sites and active regions that can contribute to enhanced HER performance.

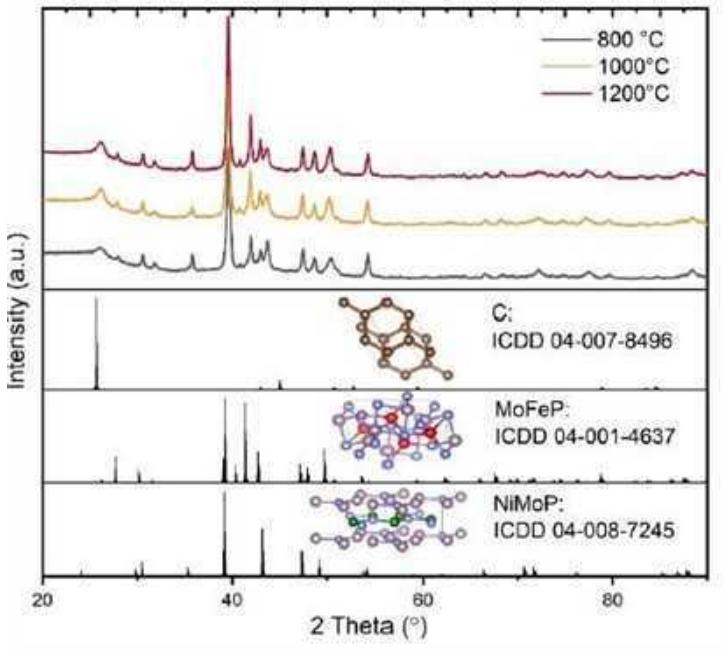


Figure 14. XRD of C-MoFeNiP samples heat treated at different temperatures.

SEM observations revealed that the synthesized materials consist of nanoparticles ranging from approximately 30 nm to 1 μm, uniformly dispersed throughout the carbon matrix (Figure 16). With increasing pyrolysis temperature, the particles exhibited a subtle morphological shift from predominantly spherical to slightly ellipsoidal shapes, a change attributed to enhanced atomic mobility and anisotropic growth at elevated temperatures. Complementary EDX analysis confirmed a homogeneous distribution of Mo, Fe, Ni, and P within the observed particles, verifying the successful formation of multimetallic phosphide domains. A marginally

lower detected content of molybdenum was noted, likely arising from partial X-ray absorption within the surrounding carbon matrix, which can attenuate Mo signals during EDX measurement.

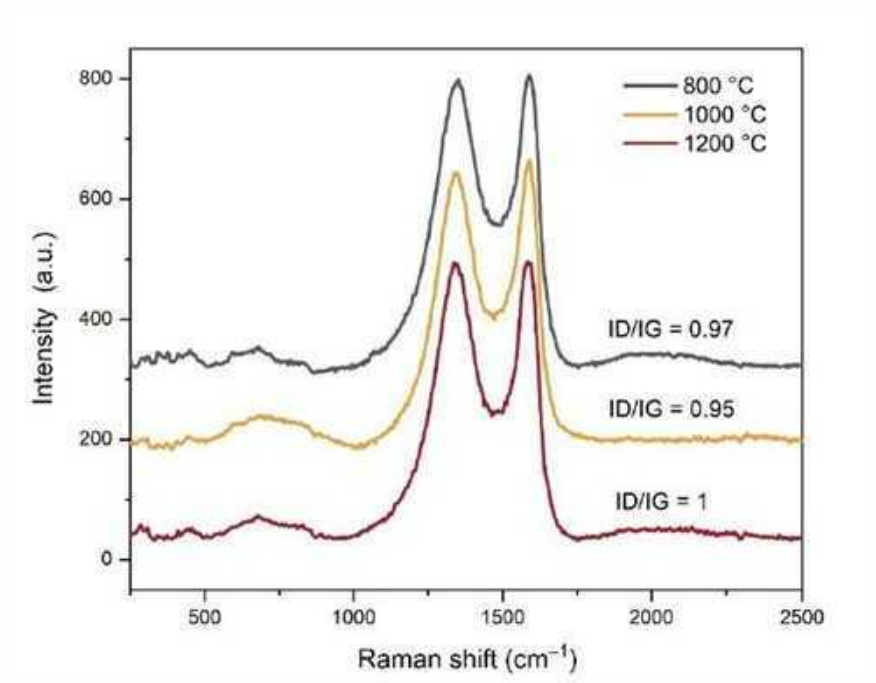


Figure 15. Raman spectra of C-MoFeNiP samples treated at different temperatures with the ID/IG ratio.

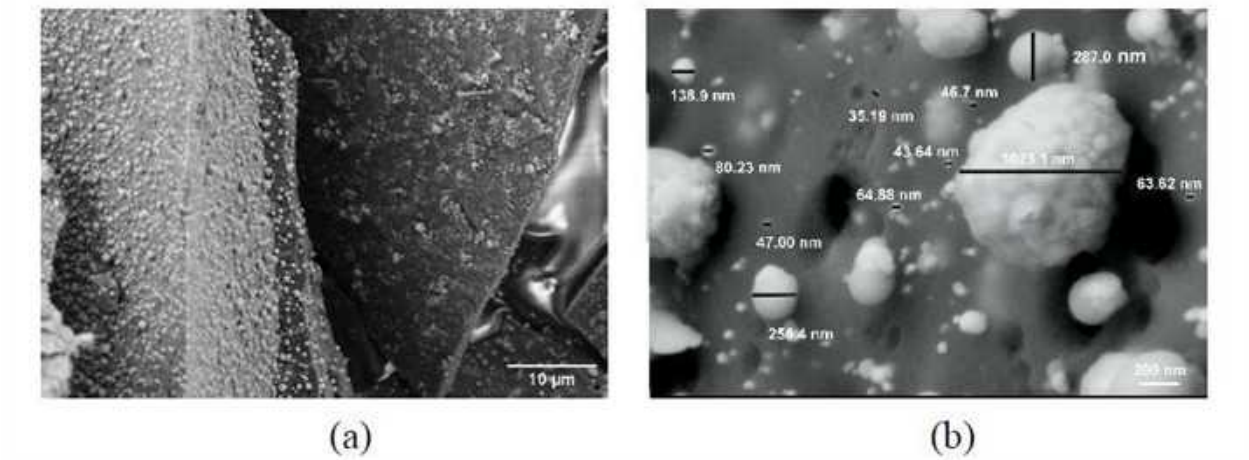


Figure 16. SEM image of the C-MoFeNiP-1000: (a) dispersion of MoFeNiP particle within the carbon matrix, (b) particle size distribution.

1.4 SEM and EDX characterization of Ni/MXene composite coatings

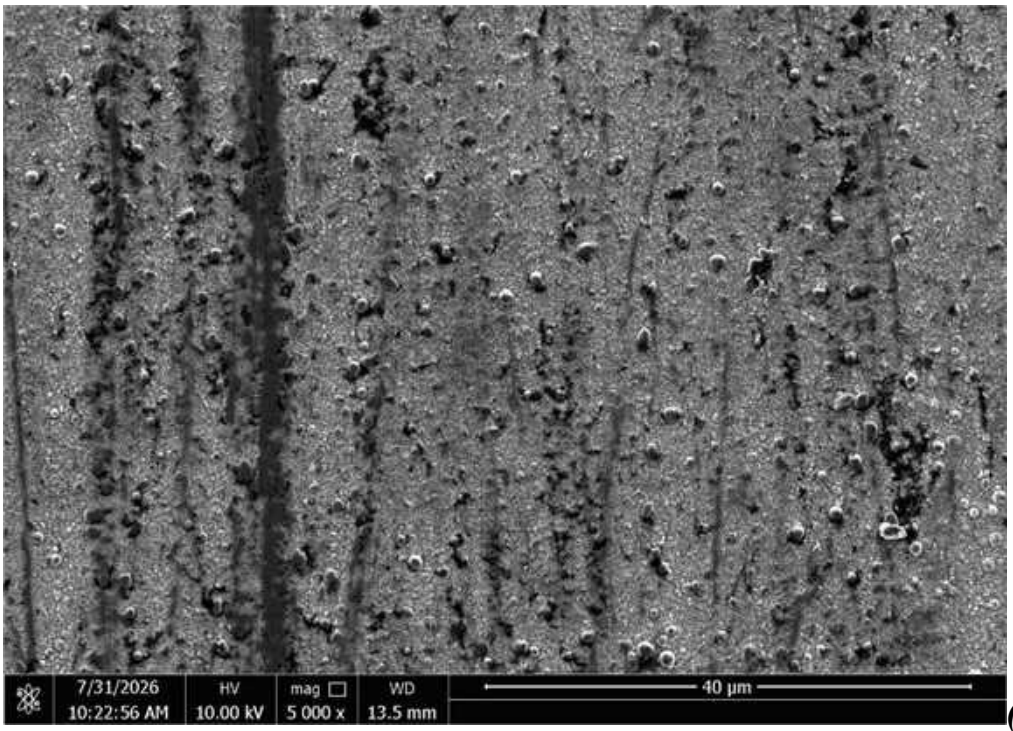
Ni/MXene composite coatings were prepared by electrodeposition from the Ethaline-based electrolyte in the presence of dispersed MXene particles. The electrodeposition conditions used for the preparation of the coatings are summarized in Table 3. The influence of two principal electrodeposition parameters, electrolyte temperature and current density, was investigated. The temperature was varied from 30 to 60 °C, while the applied current density ranged from 5 to 25 mA cm^{-2}. The deposition time was maintained constant at 20 min for all samples. This experimental matrix enabled evaluation of the combined influence of temperature and current density on the morphology of the Ni/MXene composite coatings.

Table 3. Electrodeposition conditions for Ni/MXene composite coatings.

Sample	**t°C**	**j, mA/cm²**	**τ, min**
1	40	5	20
2		10	
3		15	
4		20	
5		25	
6	50	5	
7		10	
8		15	
9		20	
10		25	

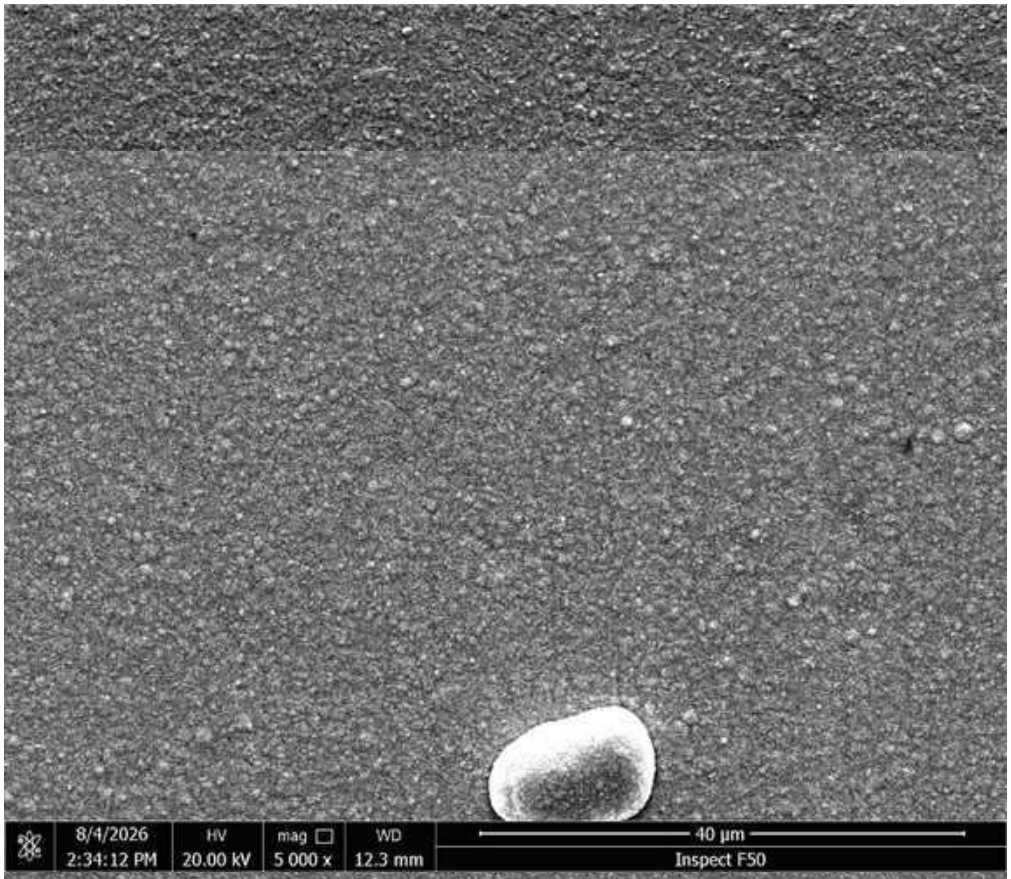
11	60	5	
12		10	
13		15	
14		20	
15		25	
16	30	5	
17		10	
18		15	
19		20	
20		25	

The surface morphology and topography of the resulting coatings were examined by SEM at several magnifications. Figures 17–20 present SEM images acquired at 5k×, 10k×, 30k×, and 100k× magnifications, respectively. The lower-magnification images provide information on the overall coating uniformity and the presence of macroscopic surface defects, whereas the higher-magnification observations reveal the micro- and nanoscale features of the electrodeposited surfaces.



(1)

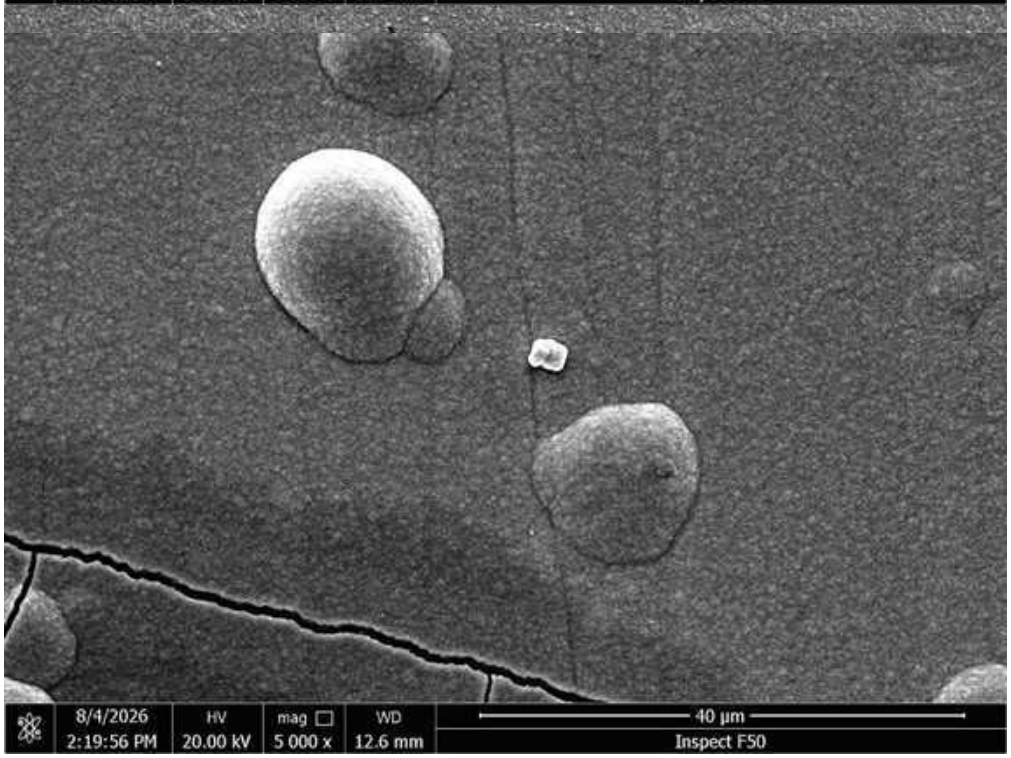
(2)



(3)

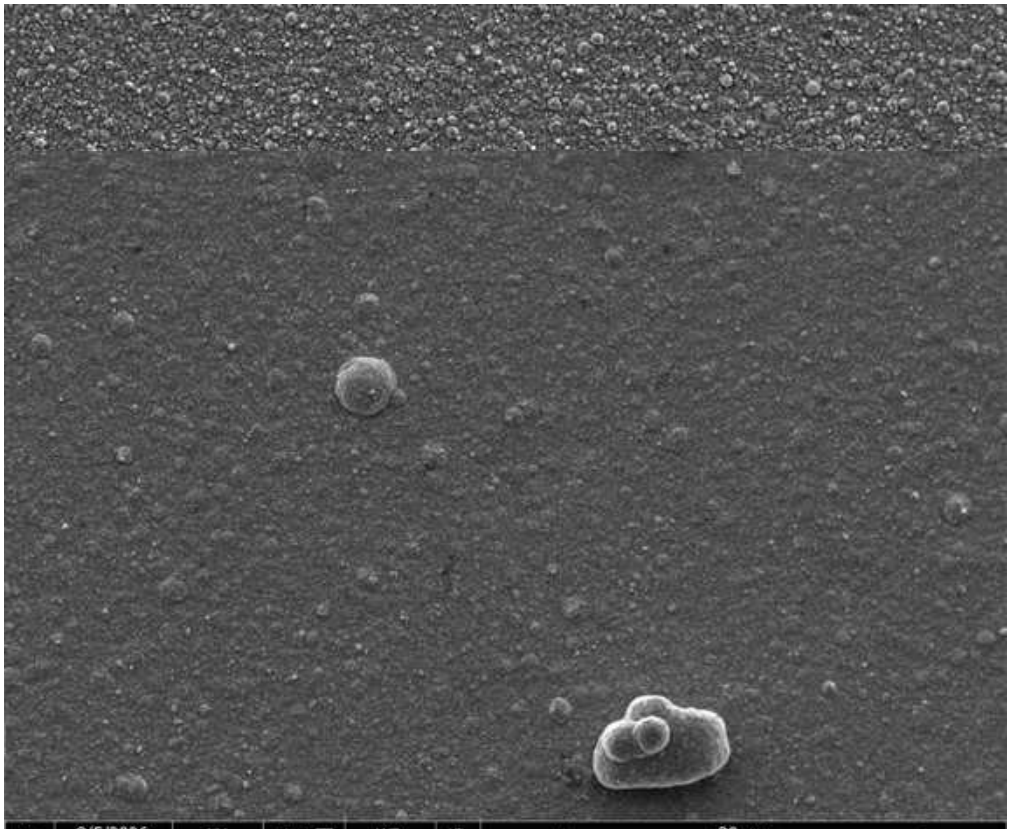
8/4/2026	HV	mag	WD	40 µm
2:34:12 PM	20.00 kV	5 000 x	12.3 mm	Inspect F50

(4)



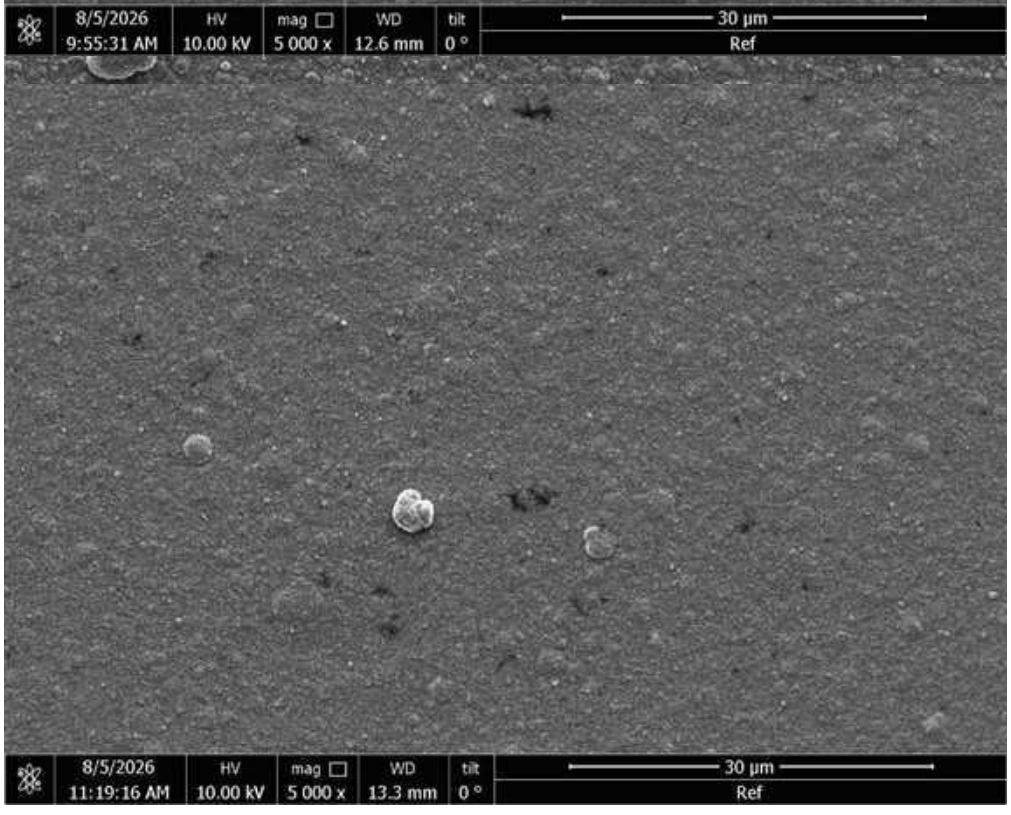
8/4/2026	HV	mag	WD	40 µm
2:19:56 PM	20.00 kV	5 000 x	12.6 mm	Inspect F50

(5)



(6)

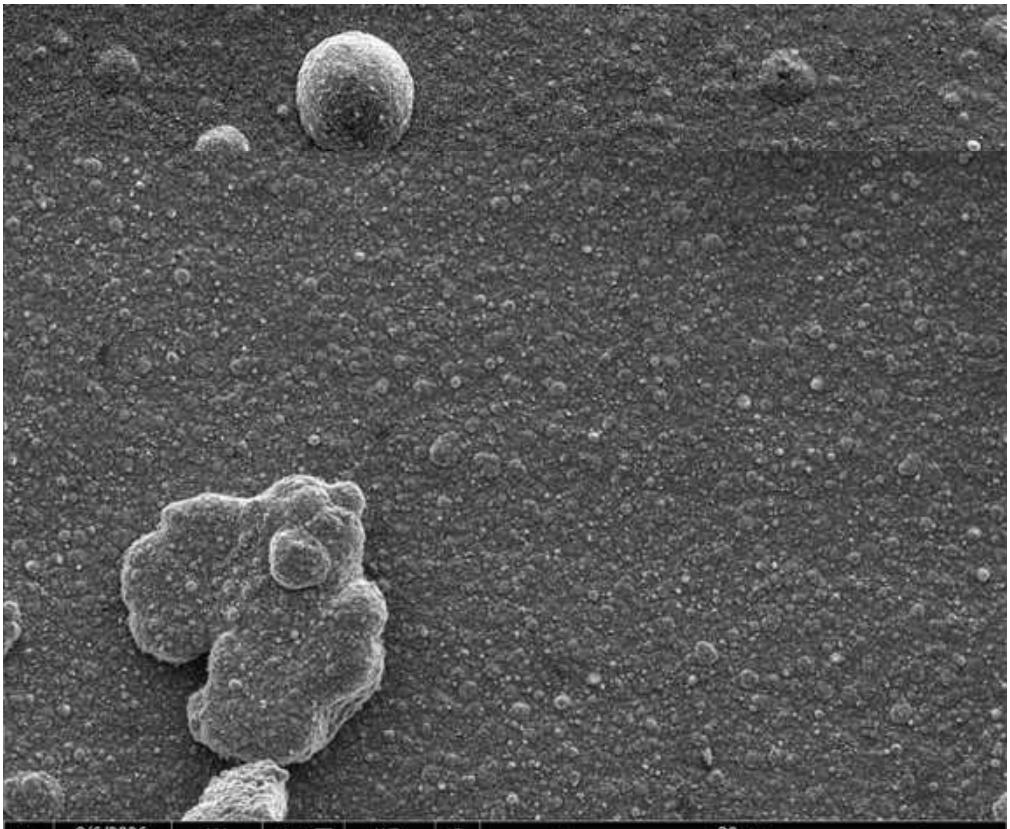
(7)


8/5/2026
9:55:31 AM
HV
10.00 kV
mag
5 000 x
WD
12.6 mm
tilt
0 °
30 µm
Ref

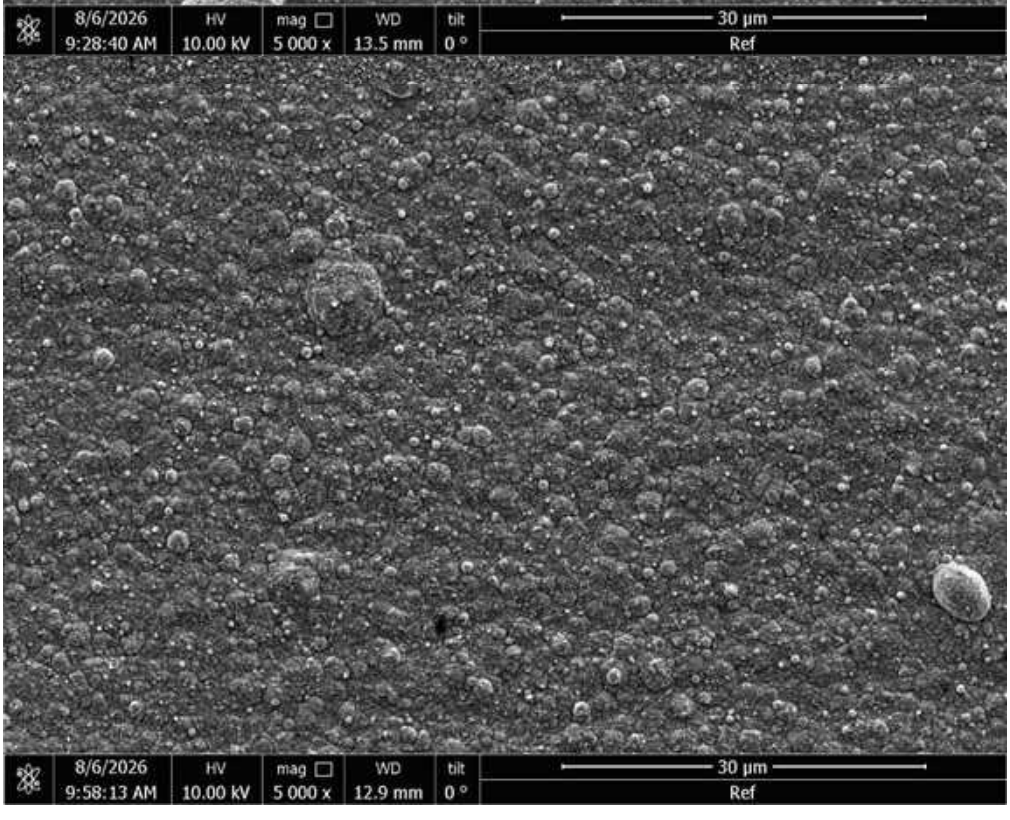
(8)

8/5/2026
11:19:16 AM
HV
10.00 kV
mag
5 000 x
WD
13.3 mm
tilt
0 °
30 µm
Ref

(9)



(10)

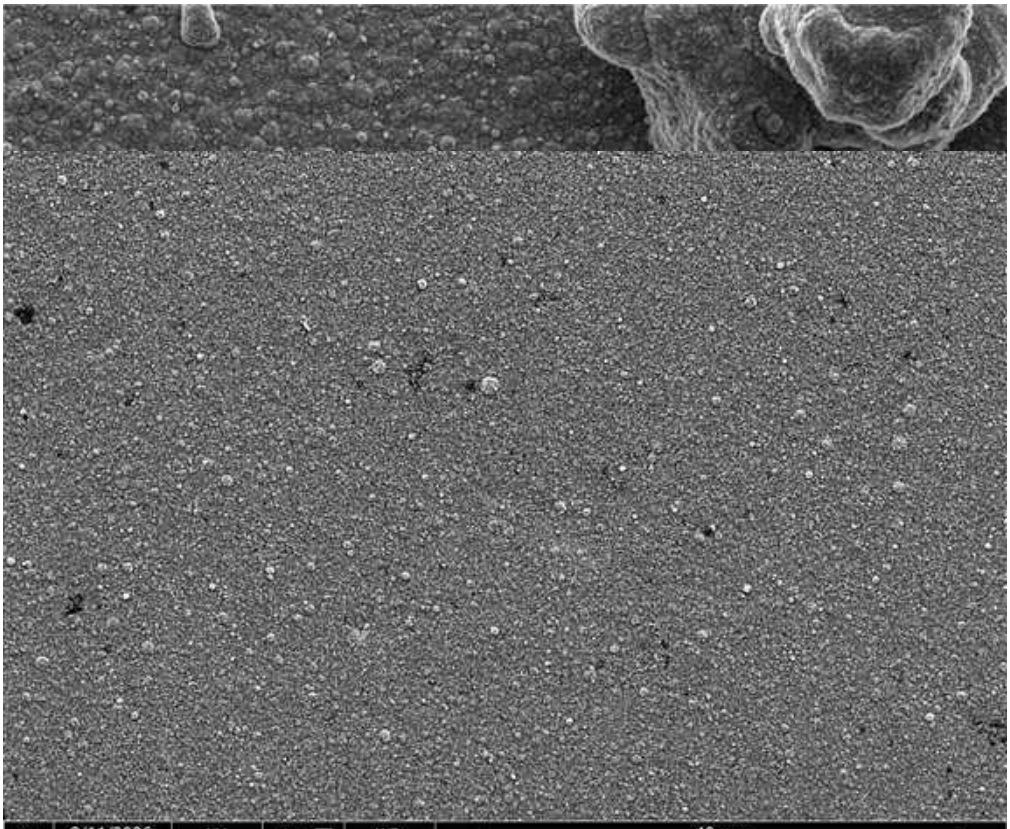

8/6/2026
9:28:40 AM
HV
10.00 kV
mag
5 000 x
WD
13.5 mm
tilt
0 °
30 µm
Ref

(11)

(12)

8/6/2026
9:58:13 AM
HV
10.00 kV
mag
5 000 x
WD
12.9 mm
tilt
0 °
30 µm
Ref

(13)

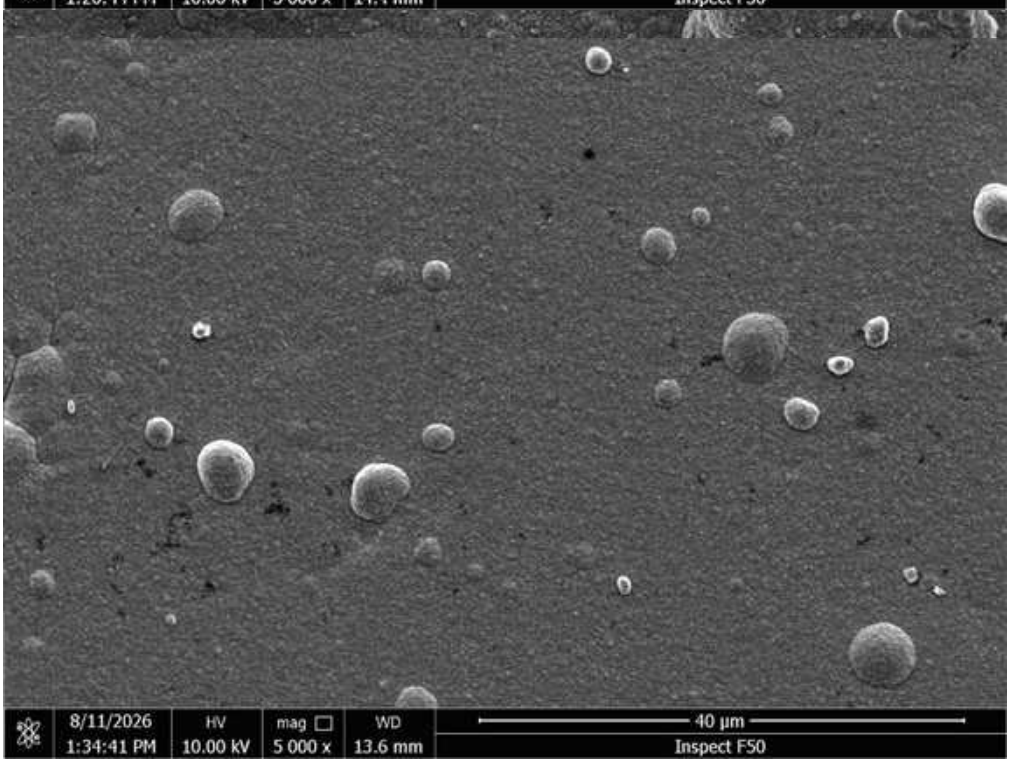


(14)

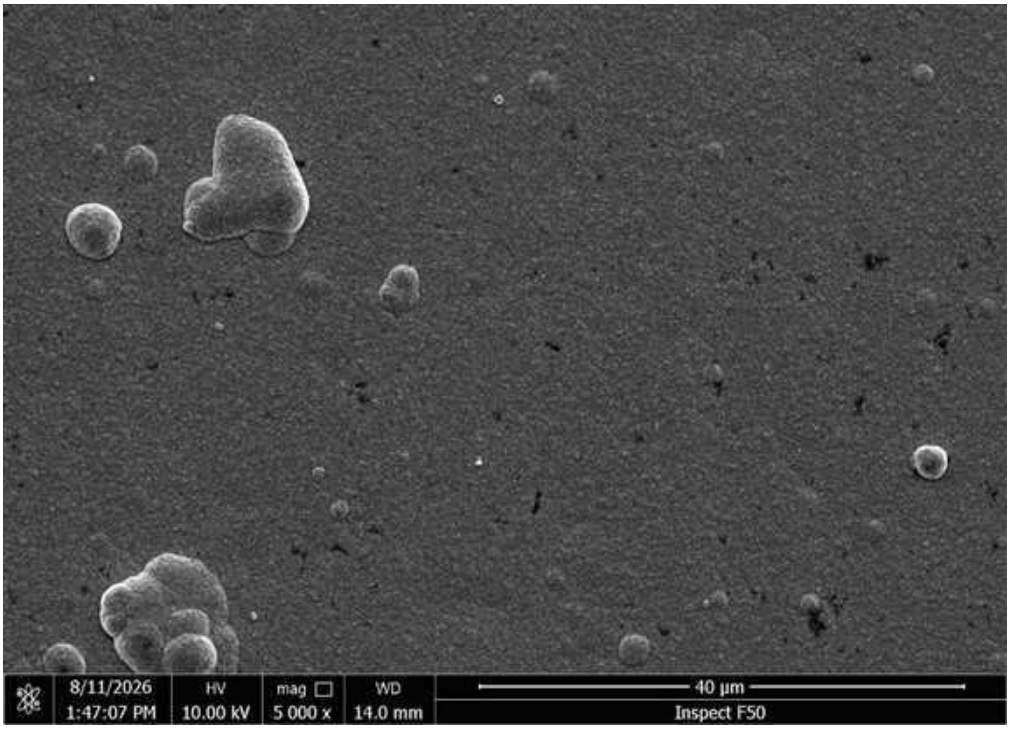
8/11/2026
1:20:44 PM
HV
10.00 kV
mag
5 000 x
WD
14.4 mm
40 µm
Inspect F50

(15)

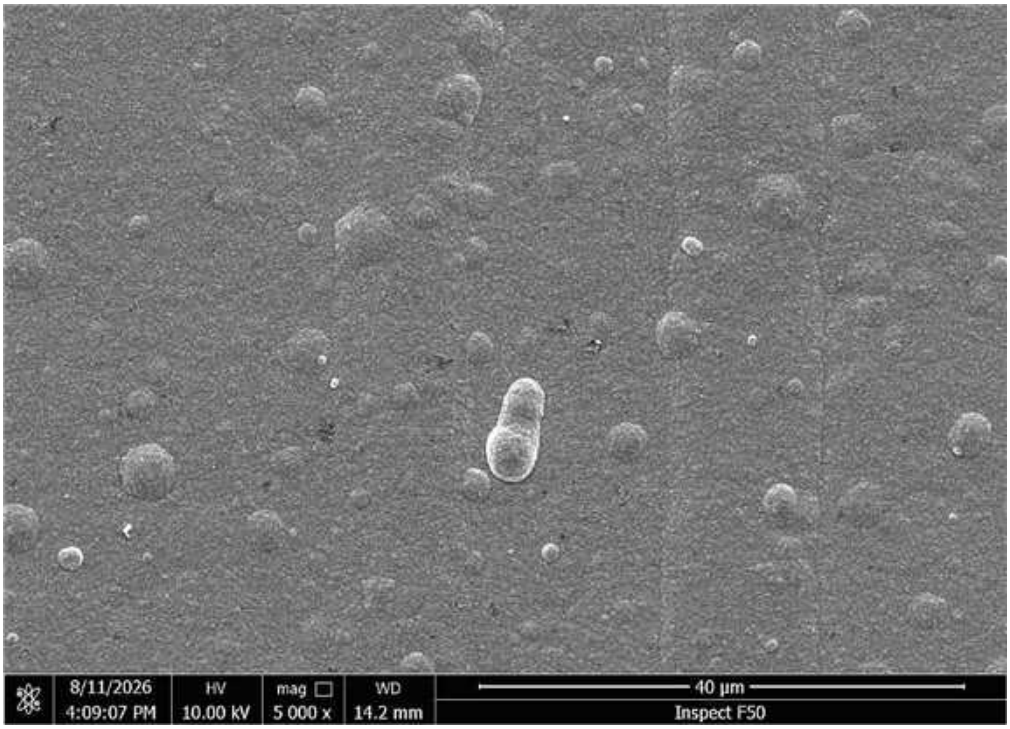
(16)


8/11/2026
1:34:41 PM
HV
10.00 kV
mag
5 000 x
WD
13.6 mm
40 µm
Inspect F50

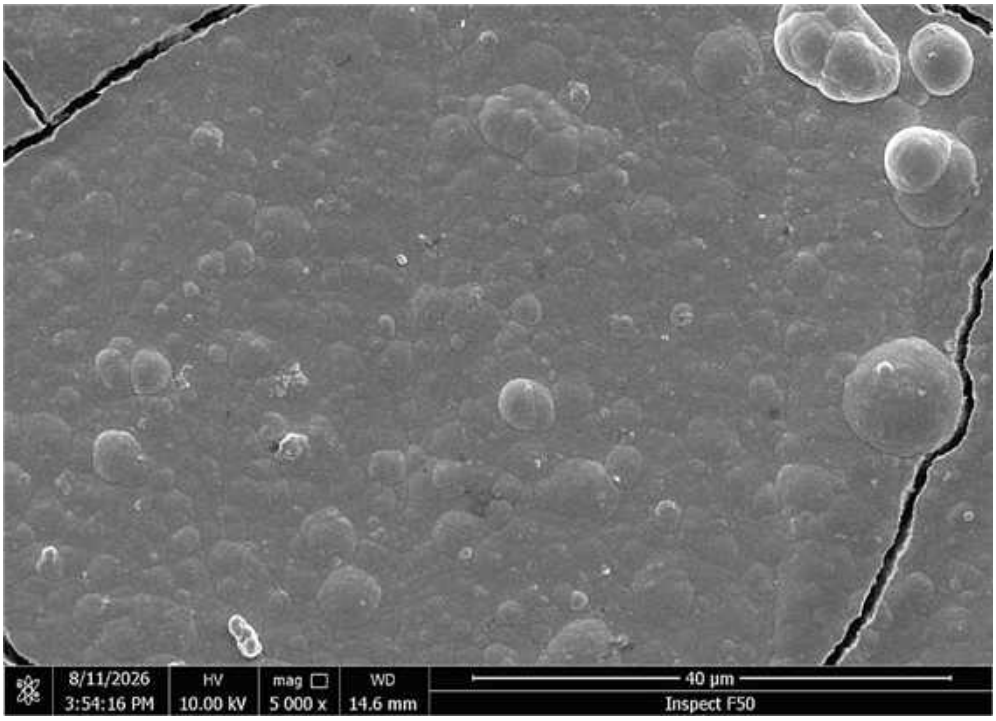
(17)


8/11/2026
1:47:07 PM
HV
10.00 kV
mag
5 000 x
WD
14.0 mm
40 µm
Inspect F50

(18)

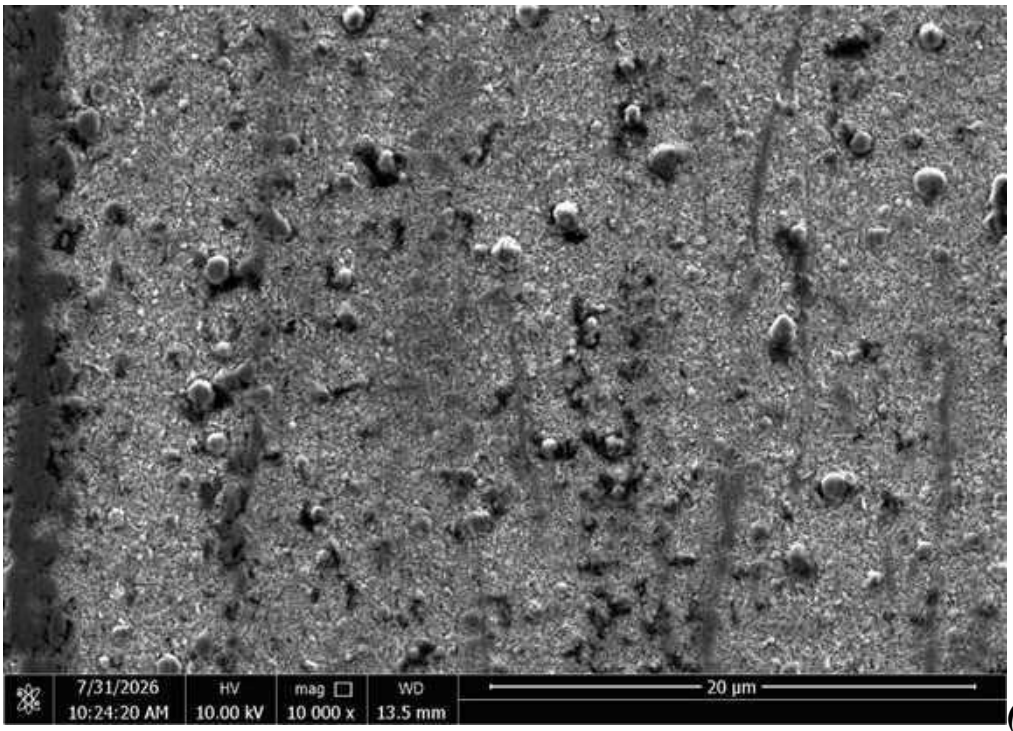

8/11/2026
4:09:07 PM
HV
10.00 kV
mag
5 000 x
WD
14.2 mm
40 µm
Inspect F50

(19)

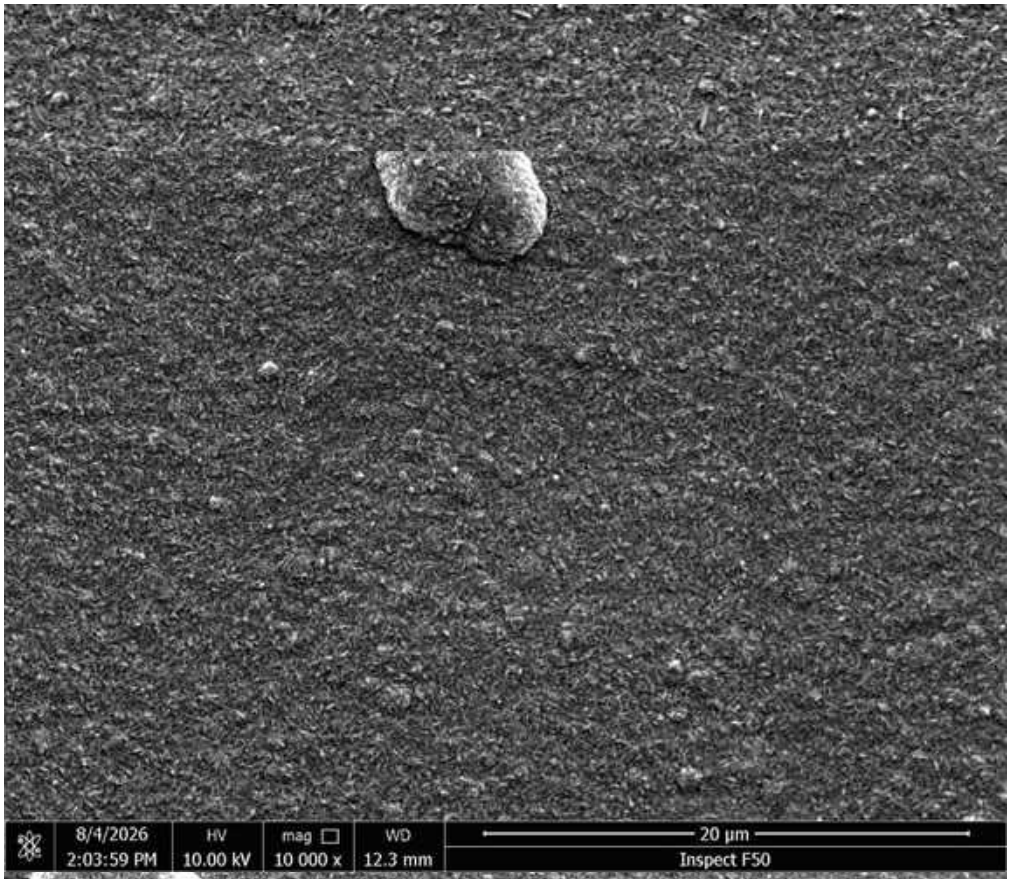


(20)

Figure 17. SEM images of Ni/M-Xene coatings electrodeposited from the Ethalinebased electrolyte at 30 – 60 °C for 20 min under different current densities. Magnification: 5k×; scale bars: 40 and 30 µm. Sample numbers correspond to the electrodeposition parameters listed in Table 3.



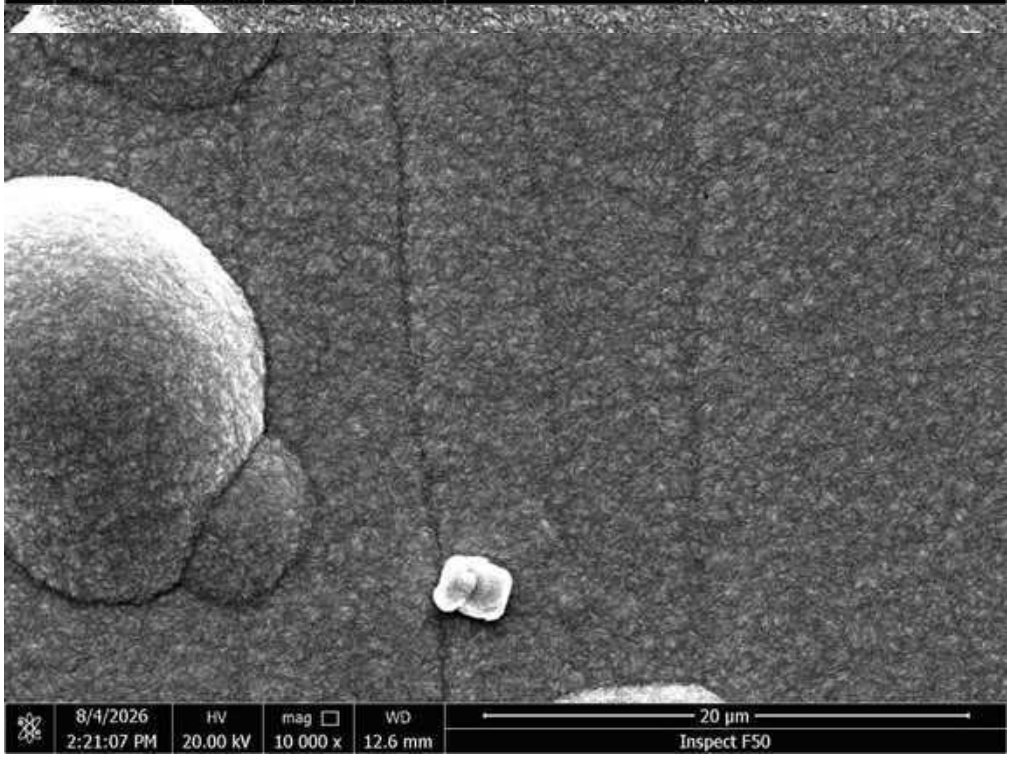
(1)


8/4/2026
2:03:59 PM
HV
10.00 kV
mag
10 000 x
WD
12.3 mm
20 µm
Inspect F50

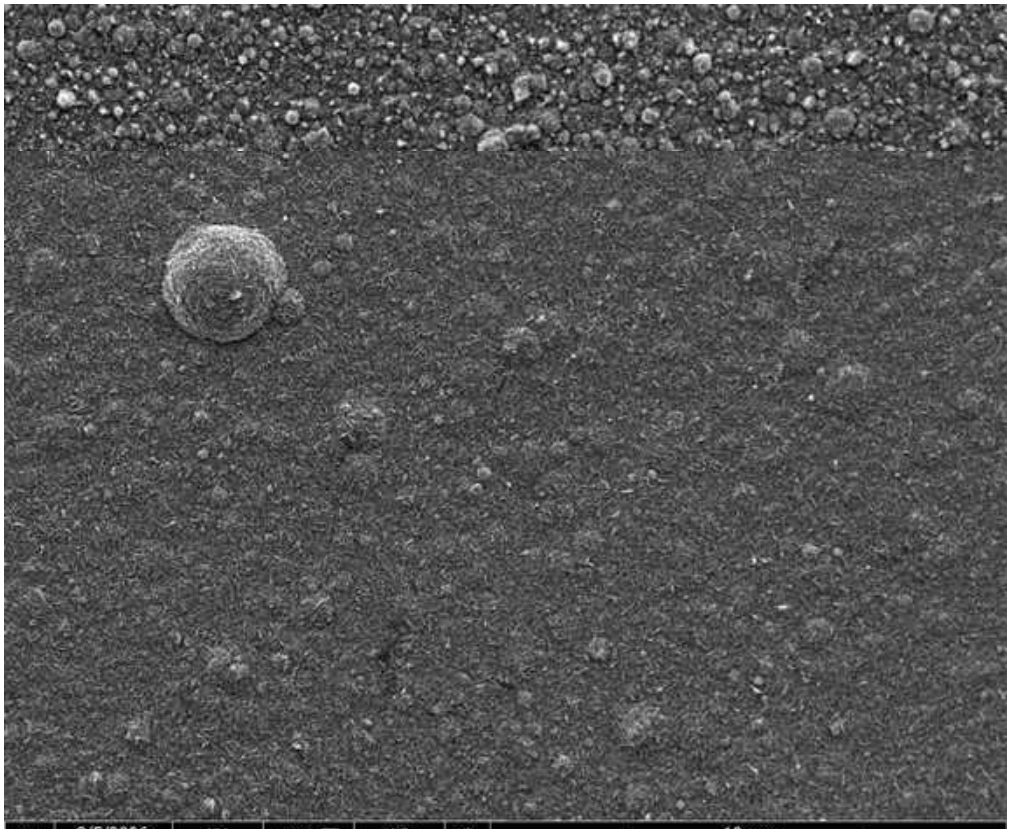
(2)

(3)

(4)


8/4/2026
2:21:07 PM
HV
20.00 kV
mag
10 000 x
WD
12.6 mm
20 µm
Inspect F50

(5)



(6)

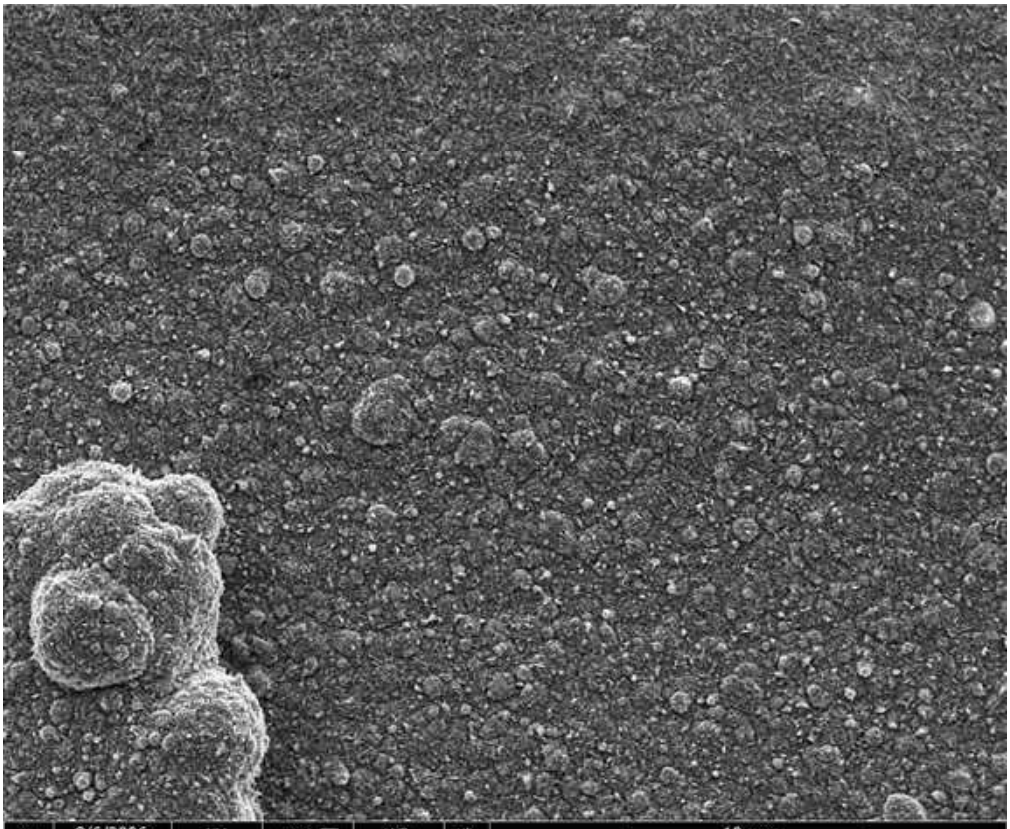
(7)


8/5/2026
9:56:33 AM
HV
10.00 kV
mag
10 000 x
WD
12.6 mm
tilt
0 °
10 µm
Ref

(8)

8/5/2026
11:19:59 AM
HV
10.00 kV
mag
10 000 x
WD
13.3 mm
tilt
0 °
10 µm
Ref

(9)

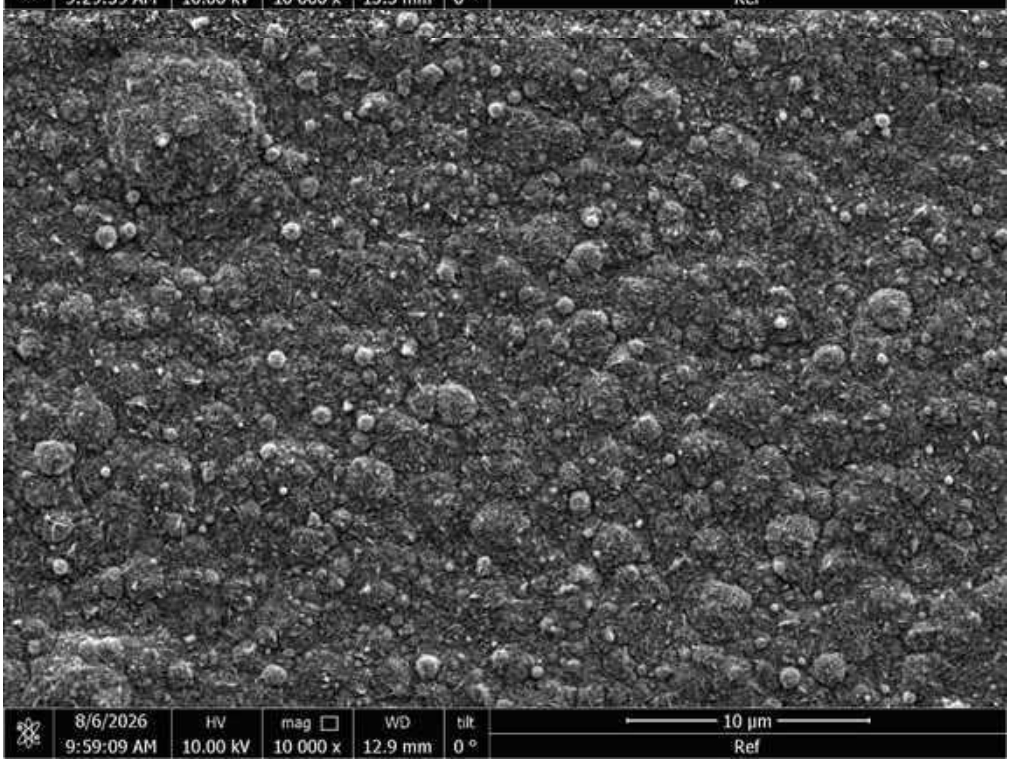


(10)

(11)

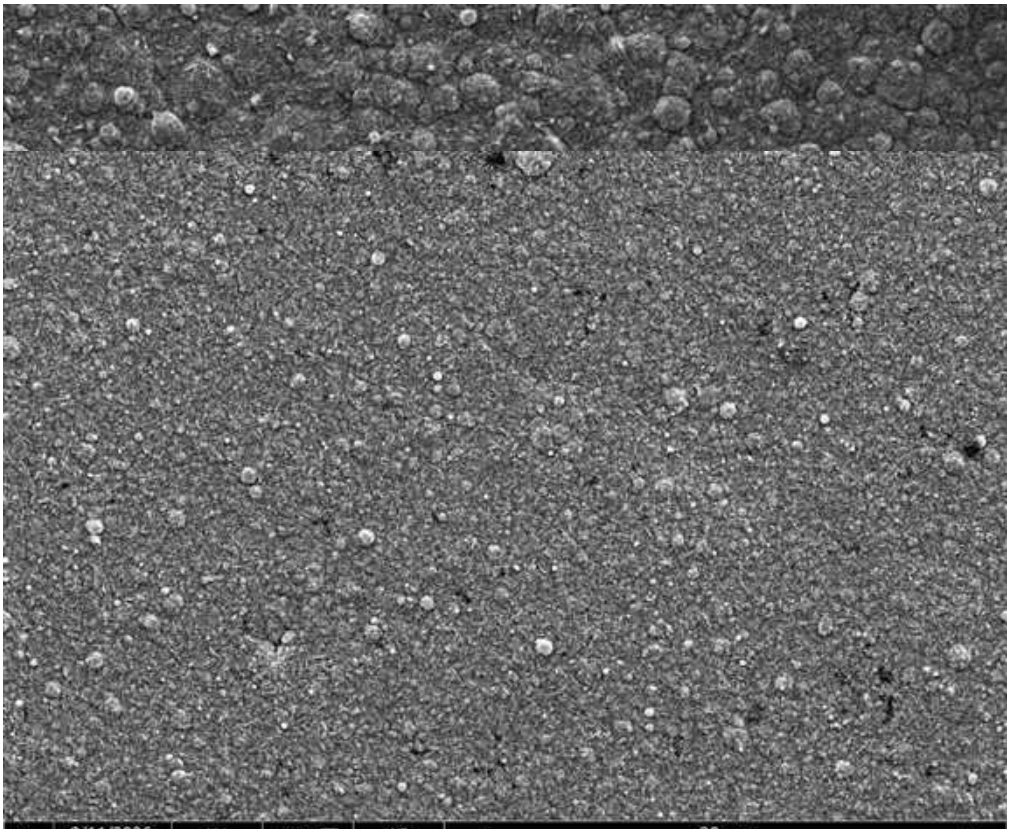
8/6/2026	HV	mag	WD	tilt	10 µm
9:29:39 AM	10.00 kV	10 000 x	13.5 mm	0 °	Ref

(12)



8/6/2026	HV	mag	WD	tilt	10 µm
9:59:09 AM	10.00 kV	10 000 x	12.9 mm	0 °	Ref

(13)

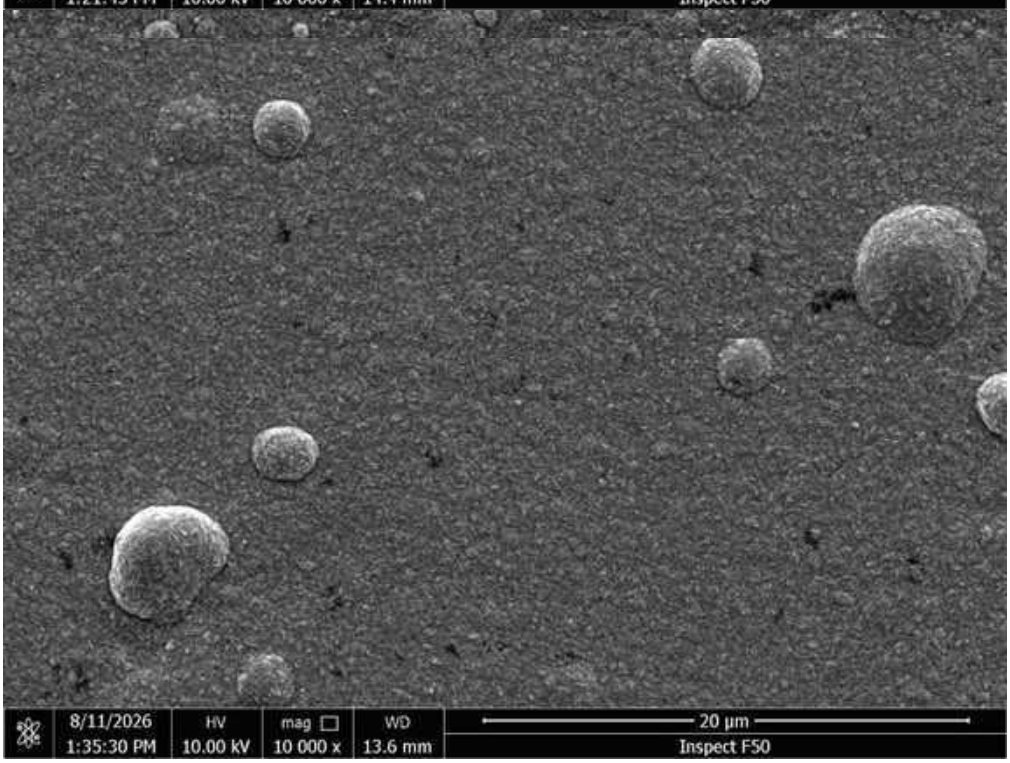


(14)

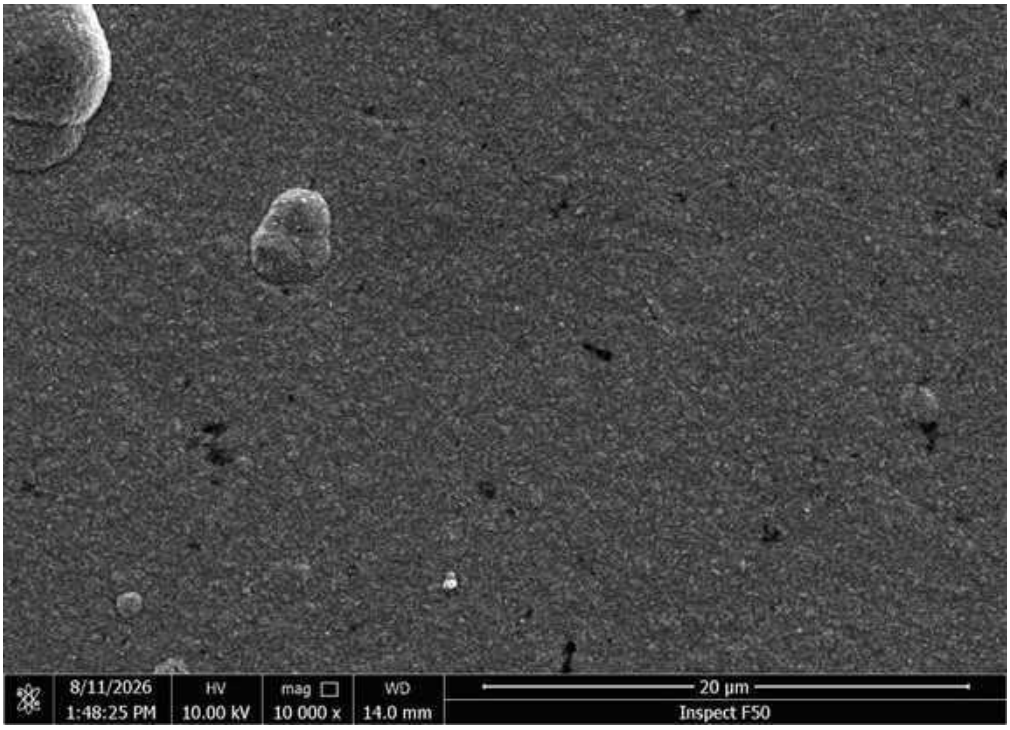
8/11/2026
1:21:45 PM
HV
10.00 kV
mag
10 000 x
WD
14.4 mm
20 µm
Inspect F50

(15)

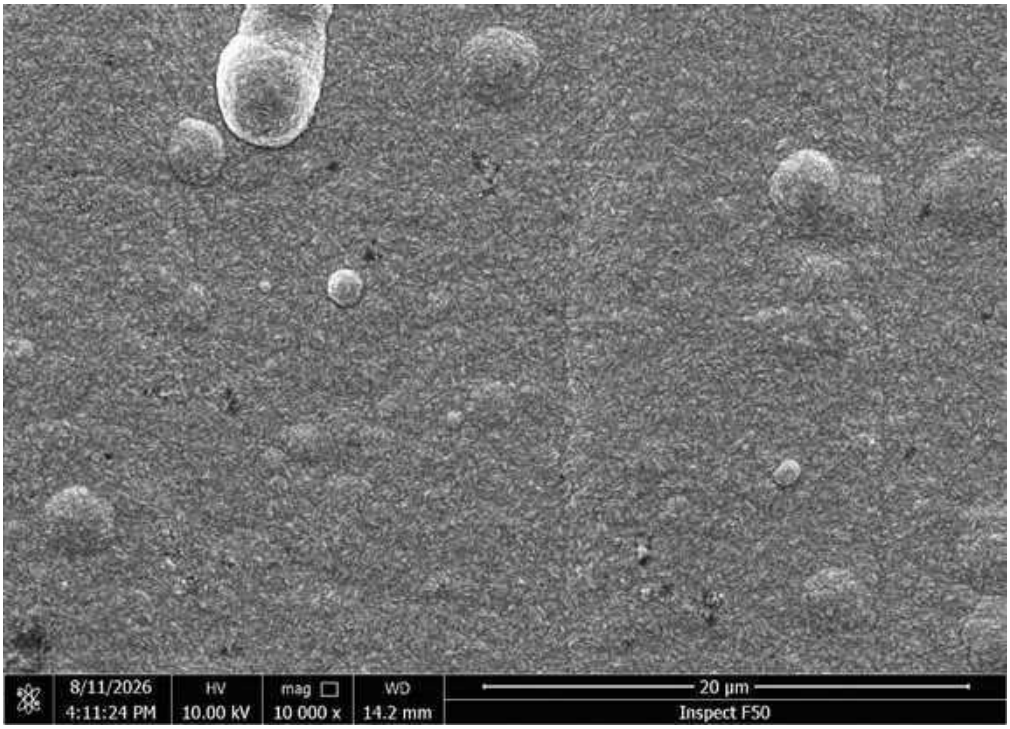
(16)


8/11/2026
1:35:30 PM
HV
10.00 kV
mag
10 000 x
WD
13.6 mm
20 µm
Inspect F50

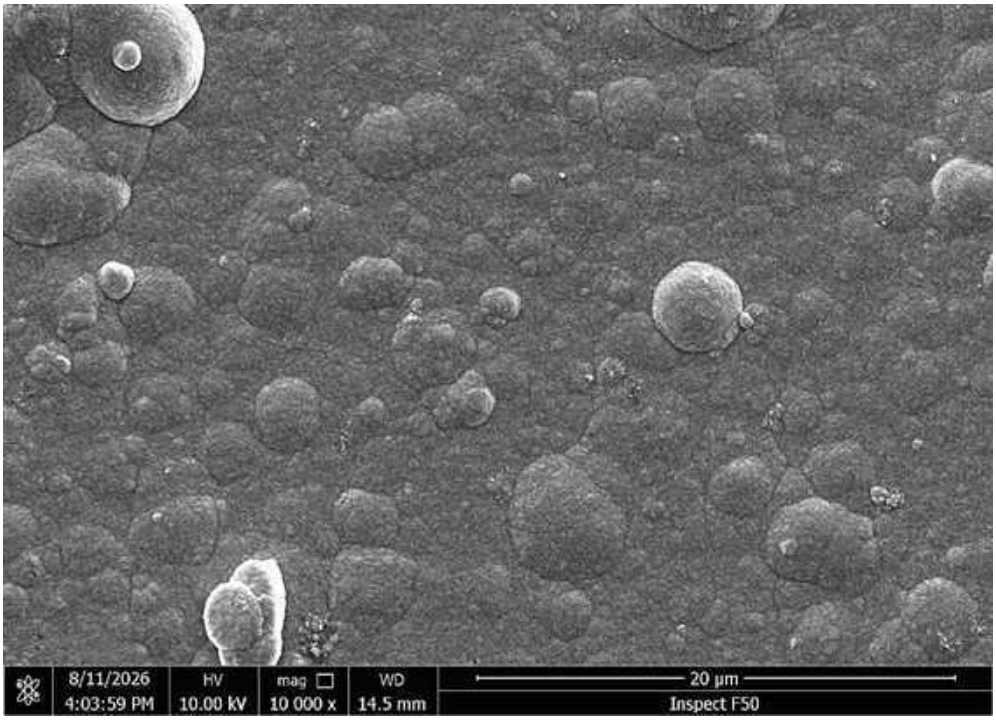
(17)


8/11/2026
1:48:25 PM
HV
10.00 kV
mag
10 000 x
WD
14.0 mm
20 µm
Inspect F50

(18)

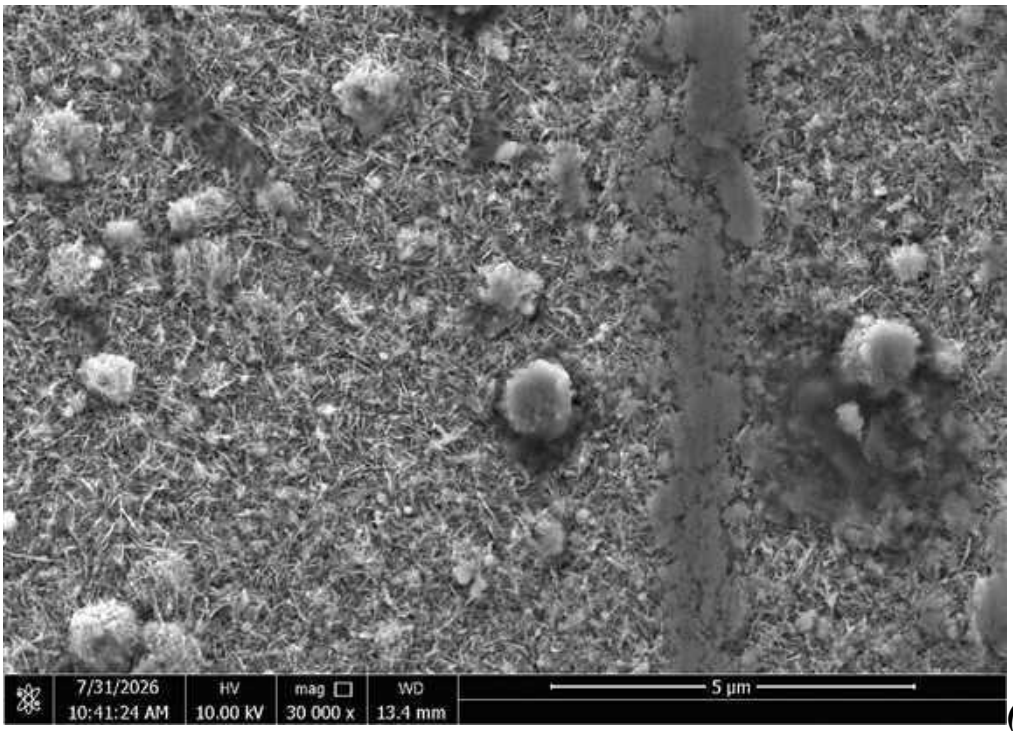

8/11/2026
4:11:24 PM
HV
10.00 kV
mag
10 000 x
WD
14.2 mm
20 µm
Inspect F50

(19)

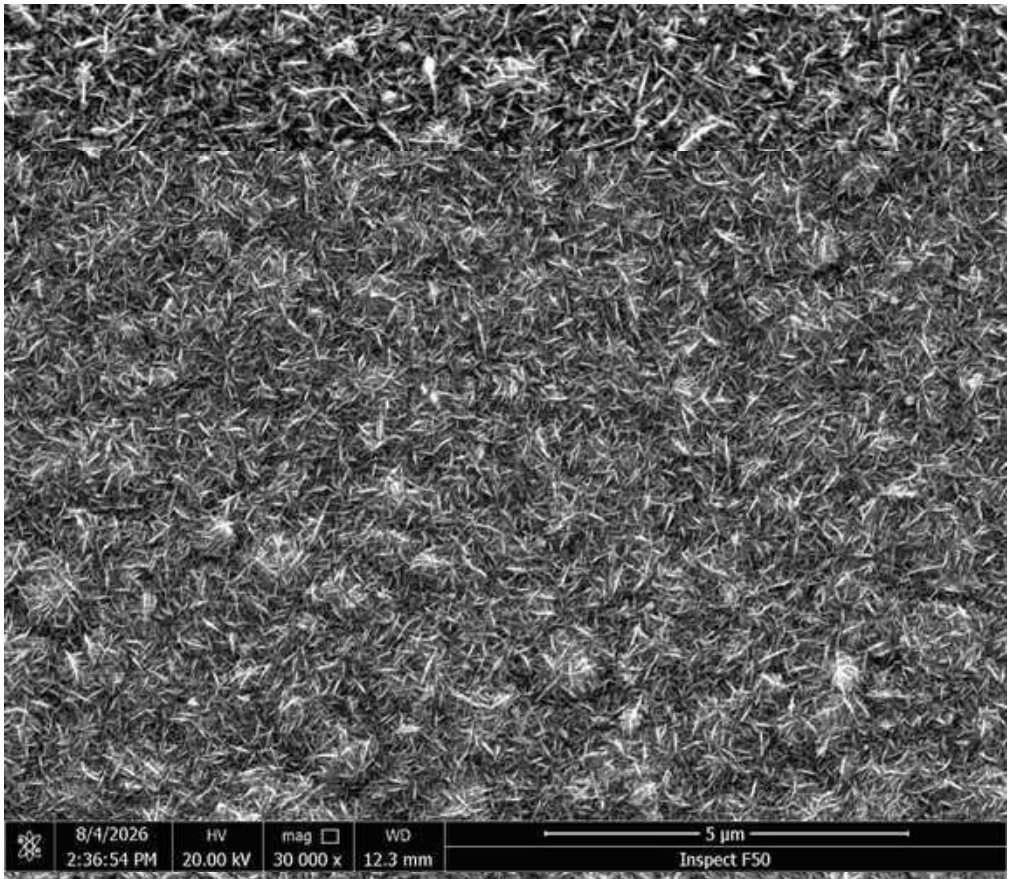


(20)

Figure 18. SEM images of Ni/M-Xene coatings electrodeposited from the Ethalinebased electrolyte at 30 – 60 °C for 20 min under different current densities. Magnification: 10k×; scale bars: 20 and 10 µm. Sample numbers correspond to the electrodeposition parameters listed in Table 3.

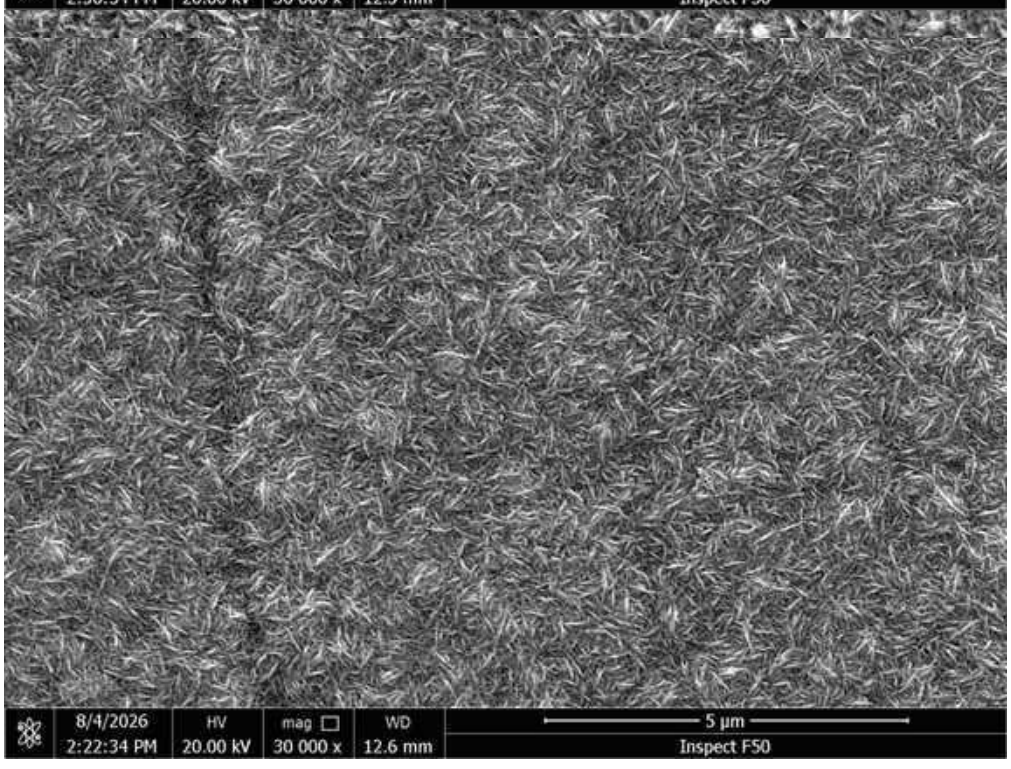


(1)



(2)

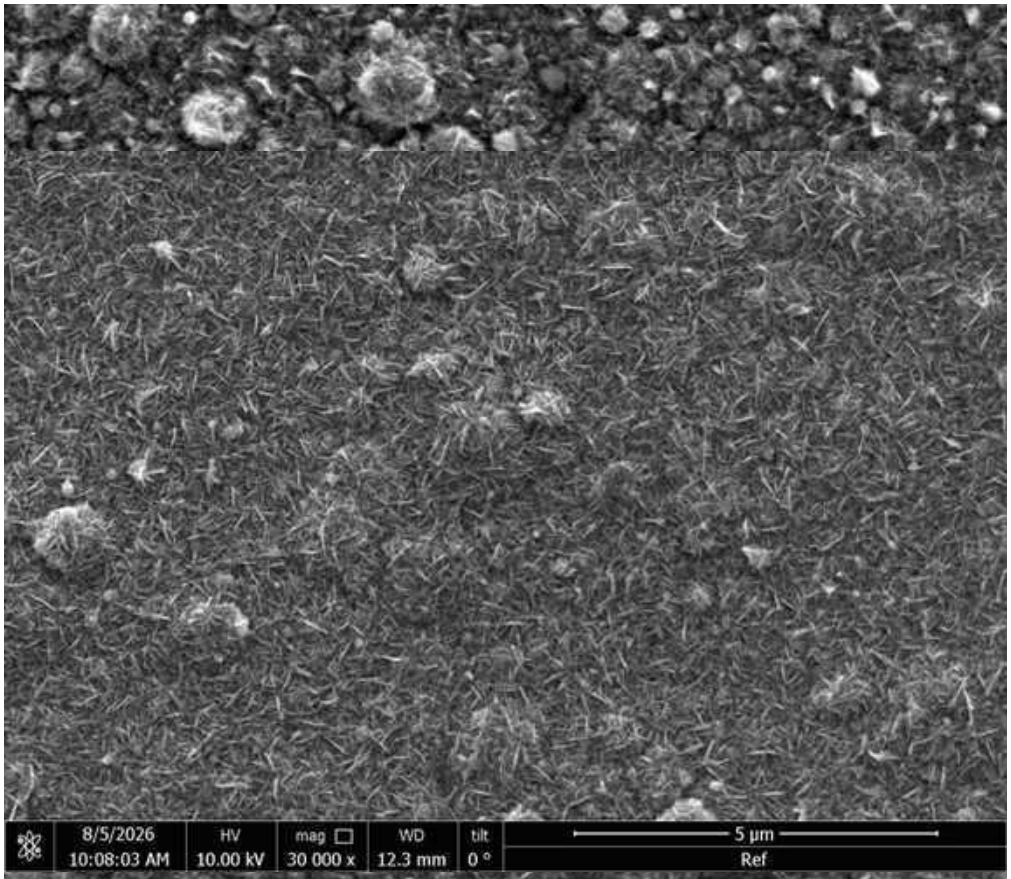
(3)


8/4/2026
2:36:54 PM
HV
20.00 kV
mag
30 000 x
WD
12.3 mm
5 µm
Inspect F50

(4)

8/4/2026
2:22:34 PM
HV
20.00 kV
mag
30 000 x
WD
12.6 mm
5 µm
Inspect F50

(5)

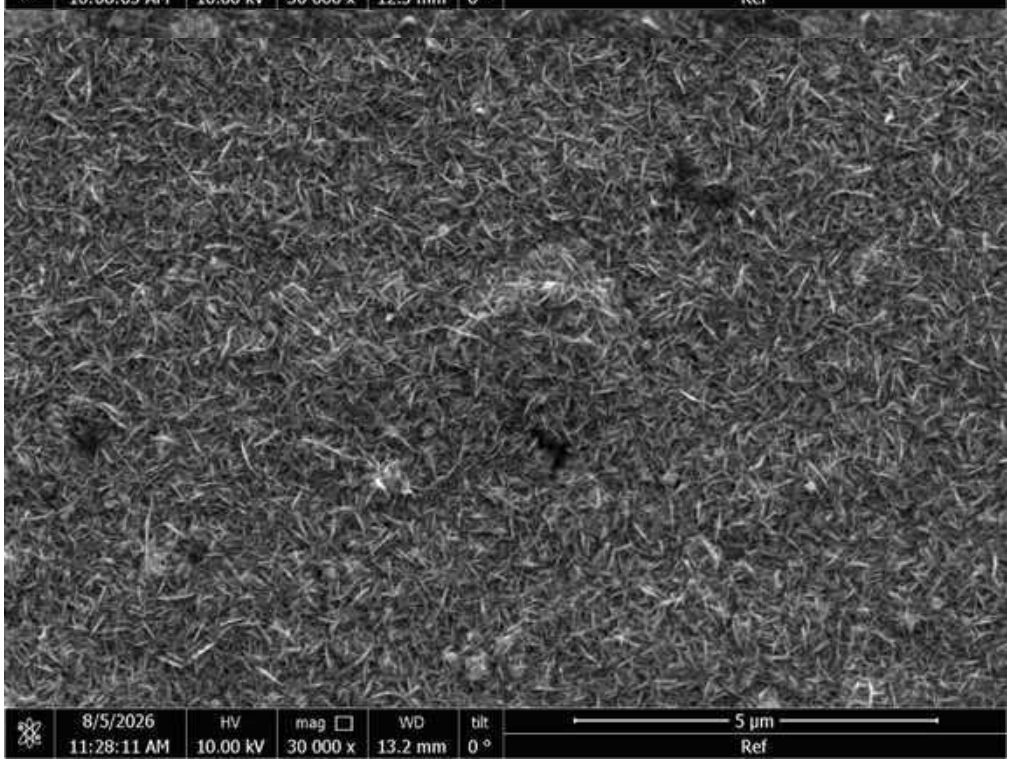


(6)

(7)

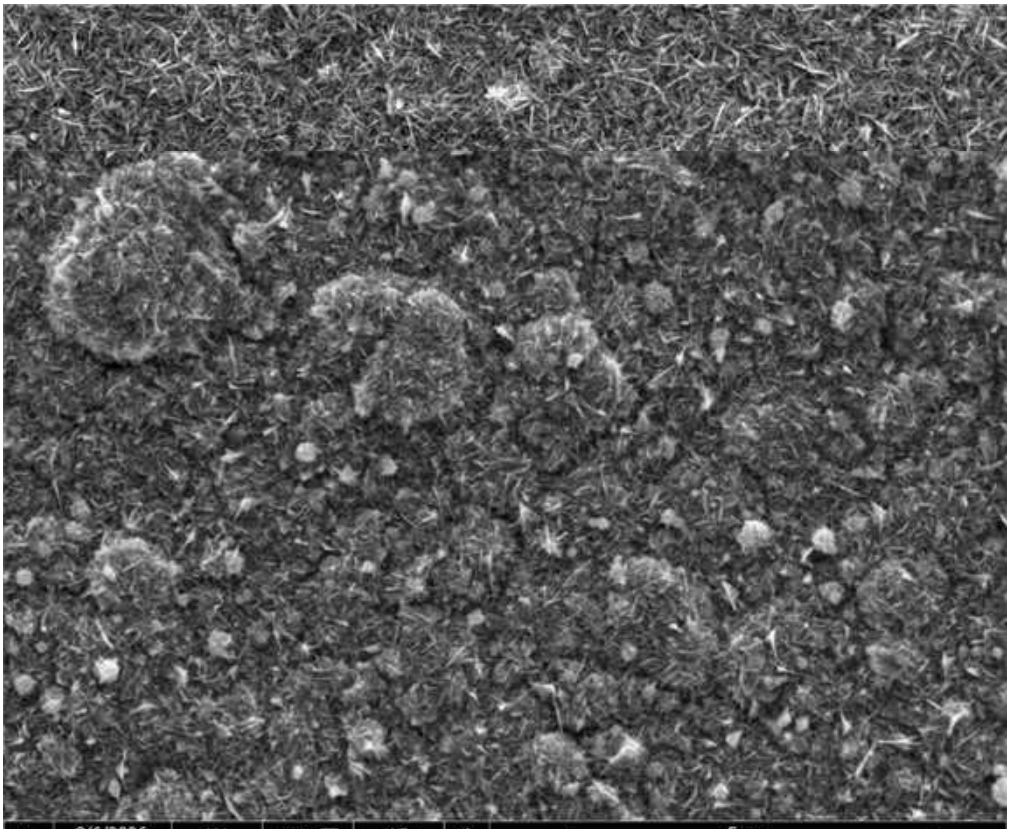
8/5/2026
10:08:03 AM
HV
10.00 kV
mag
30 000 x
WD
12.3 mm
tilt
0 °
5 µm
Ref

(8)



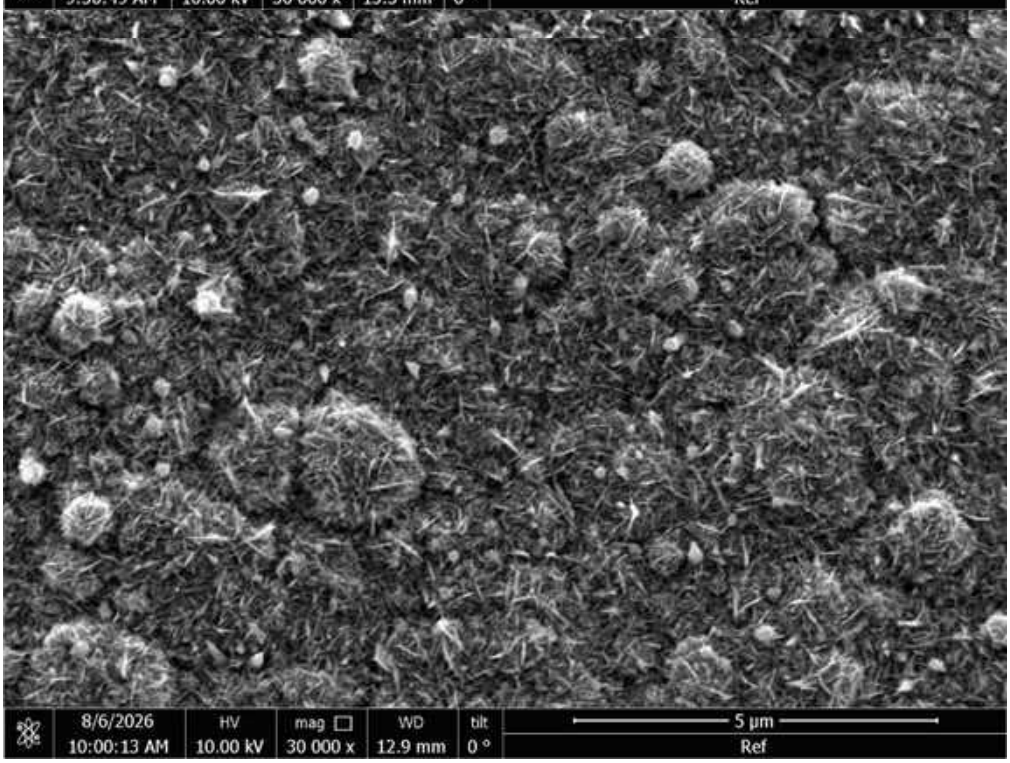
8/5/2026
11:28:11 AM
HV
10.00 kV
mag
30 000 x
WD
13.2 mm
tilt
0 °
5 µm
Ref

(9)



(10)

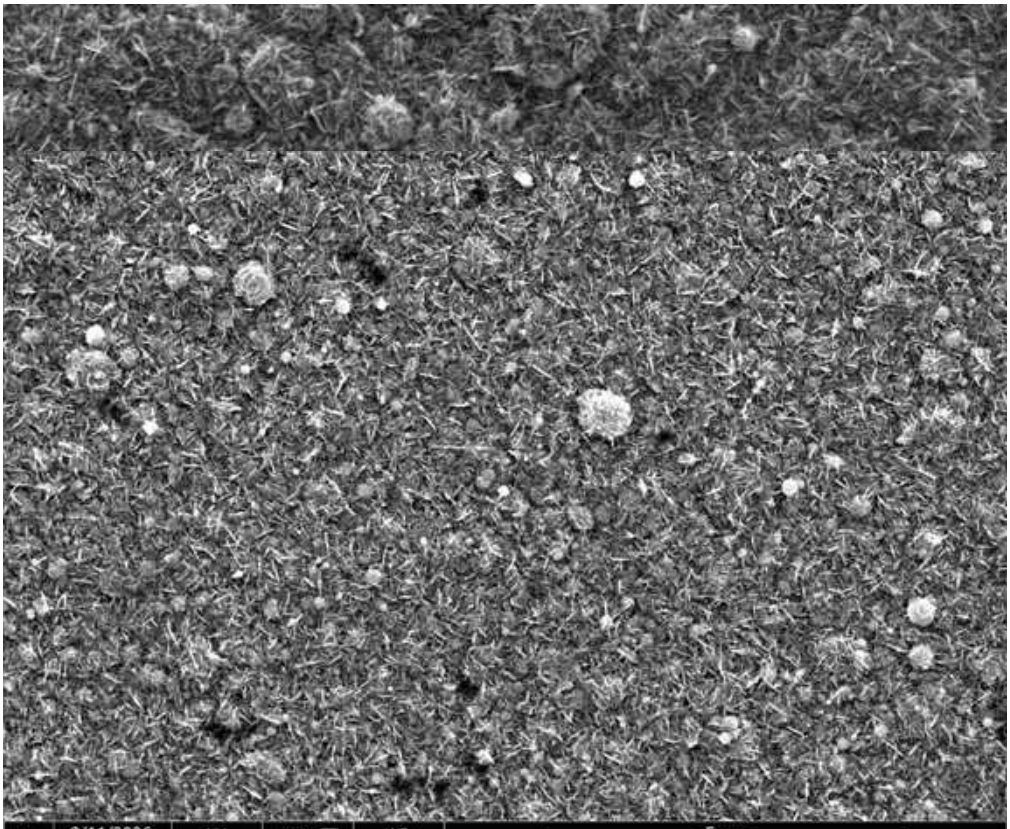
(11)


8/6/2026
9:30:49 AM
HV
10.00 kV
mag
30 000 x
WD
13.5 mm
tilt
0 °
5 µm
Ref

(12)

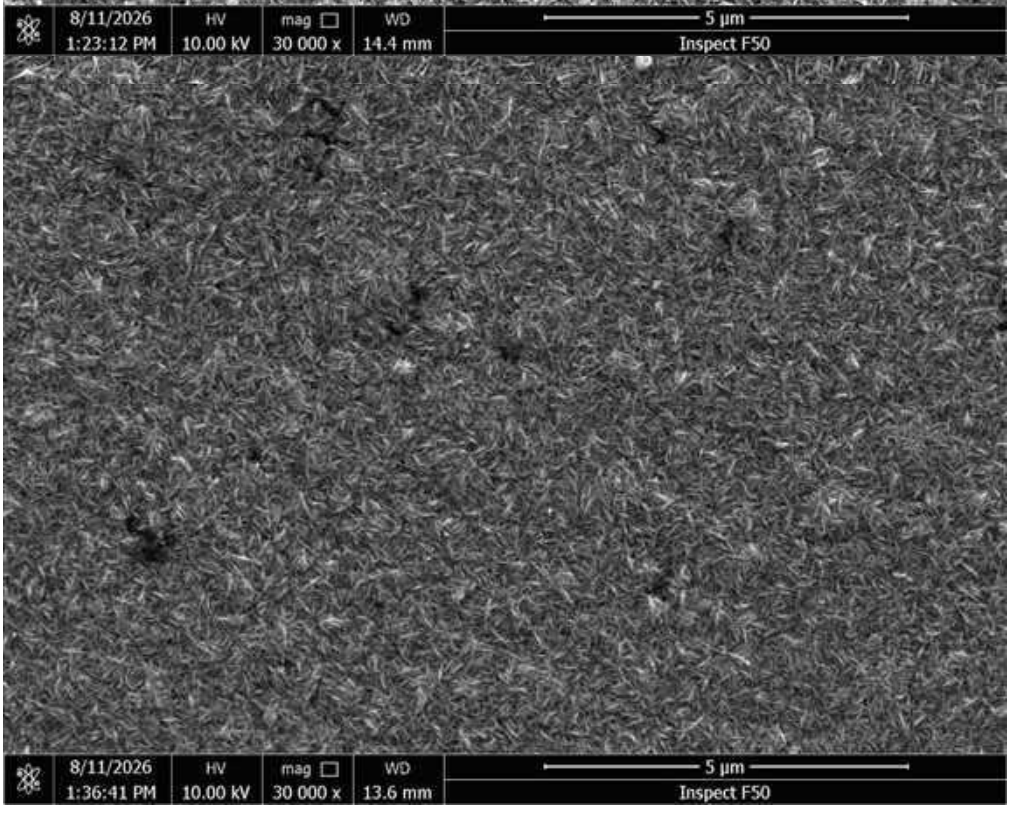
8/6/2026
10:00:13 AM
HV
10.00 kV
mag
30 000 x
WD
12.9 mm
tilt
0 °
5 µm
Ref

(13)



(14)

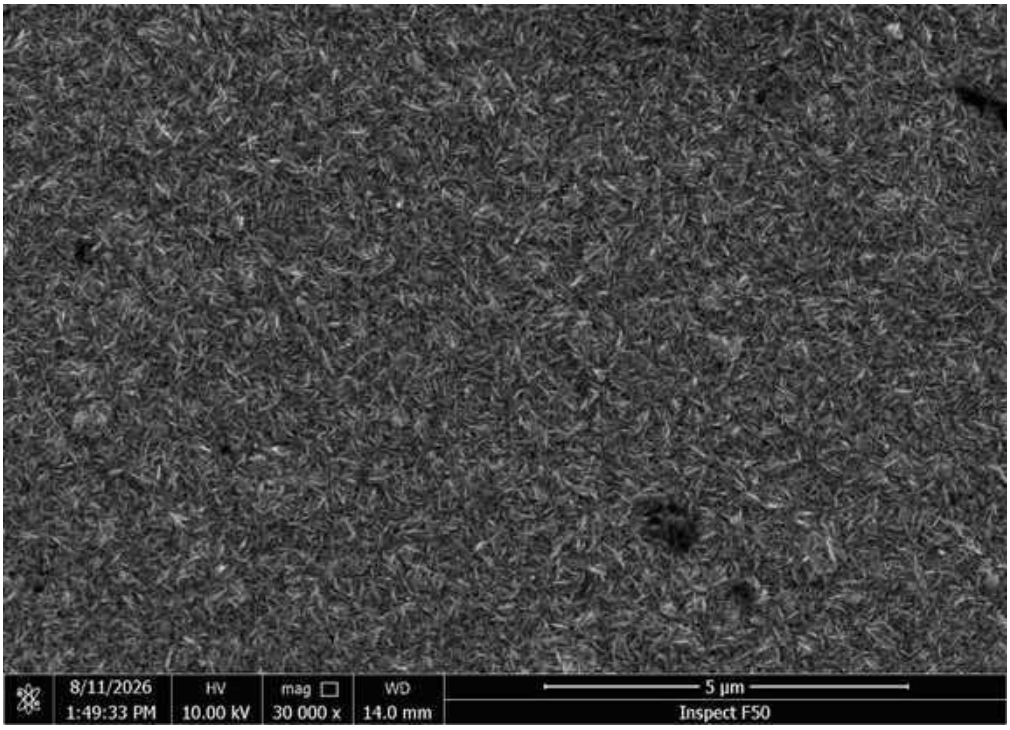
(15)


8/11/2026
1:23:12 PM
HV
10.00 kV
mag
30 000 x
WD
14.4 mm
5 µm
Inspect F50

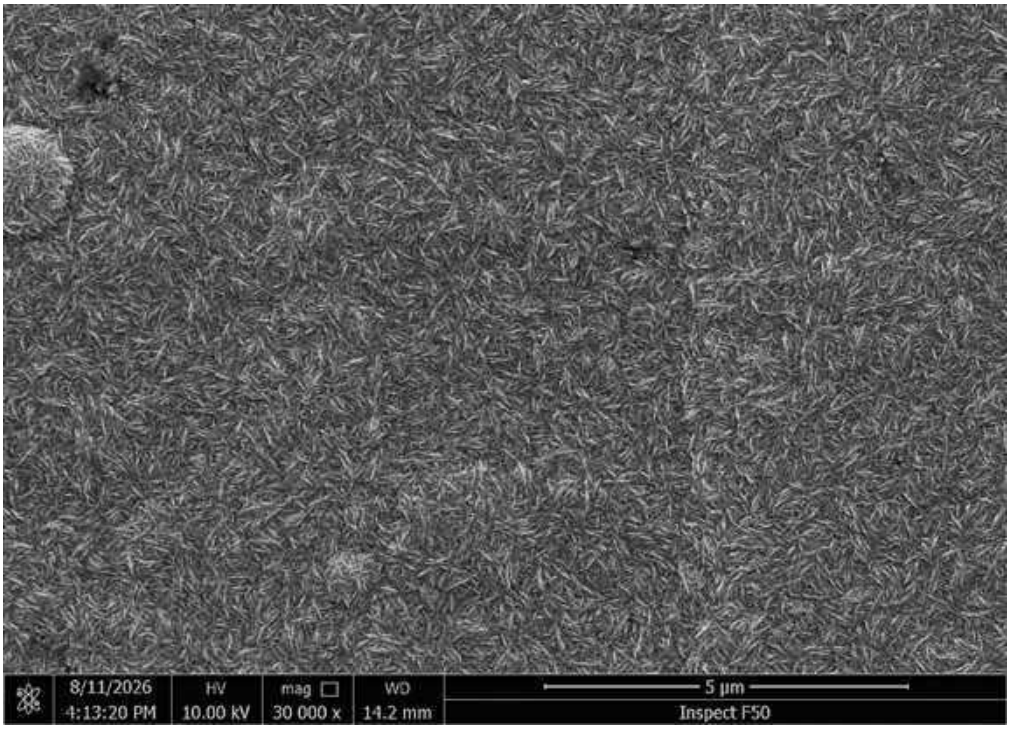
(16)

8/11/2026
1:36:41 PM
HV
10.00 kV
mag
30 000 x
WD
13.6 mm
5 µm
Inspect F50

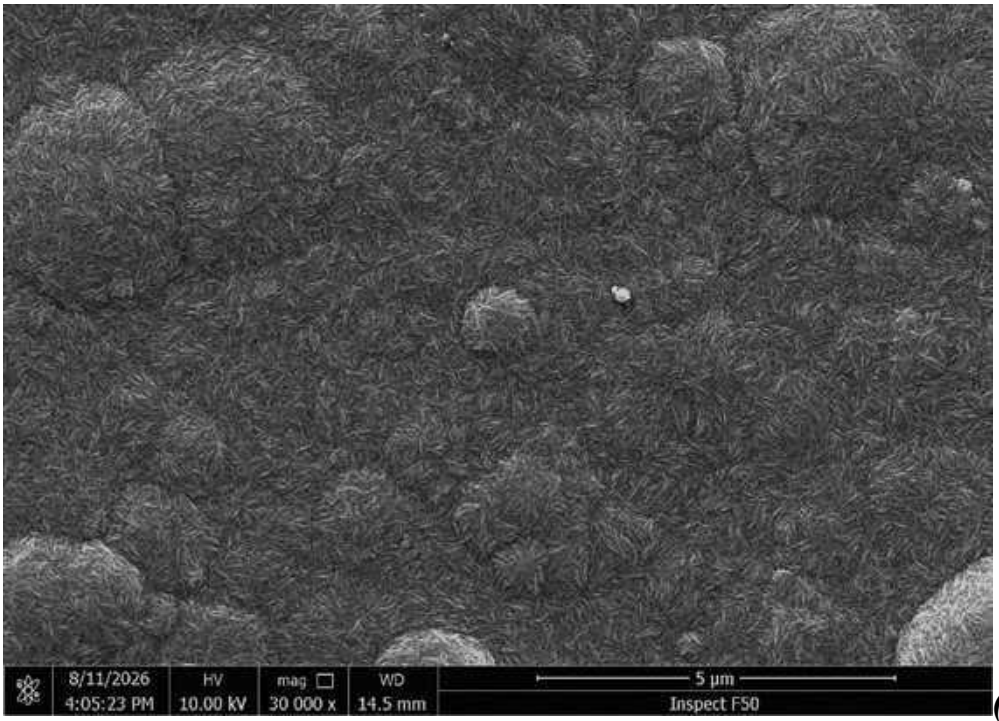
(17)


8/11/2026
1:49:33 PM
HV
10.00 kV
mag
30 000 x
WD
14.0 mm
5 µm
Inspect F50

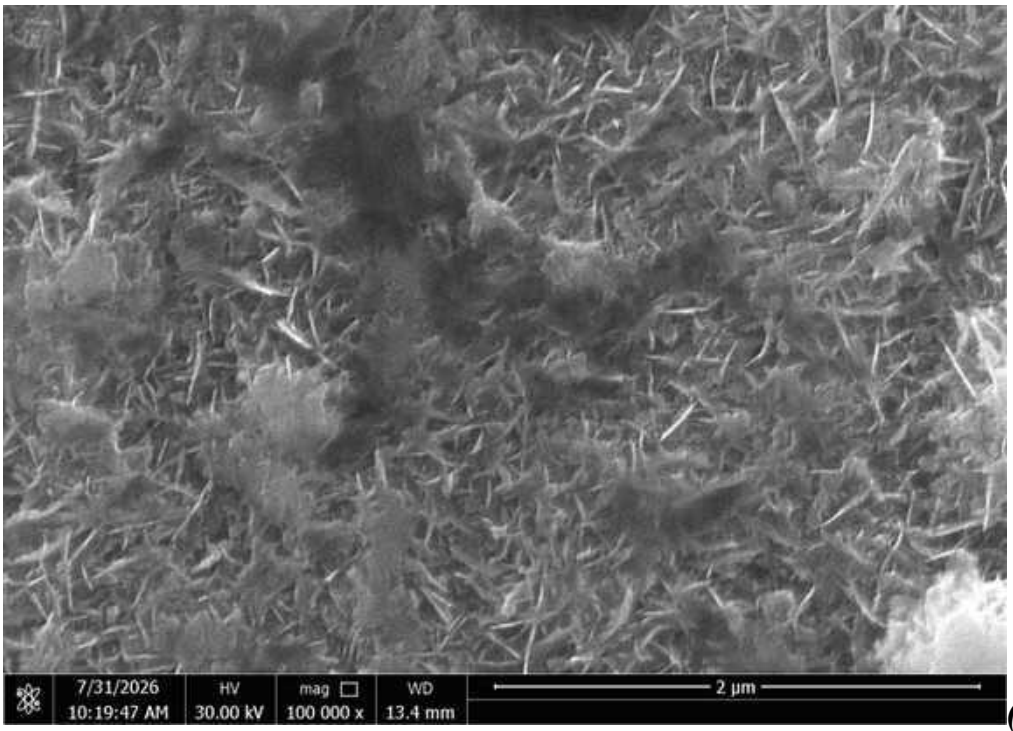
(18)


8/11/2026
4:13:20 PM
HV
10.00 kV
mag
30 000 x
WD
14.2 mm
5 µm
Inspect F50

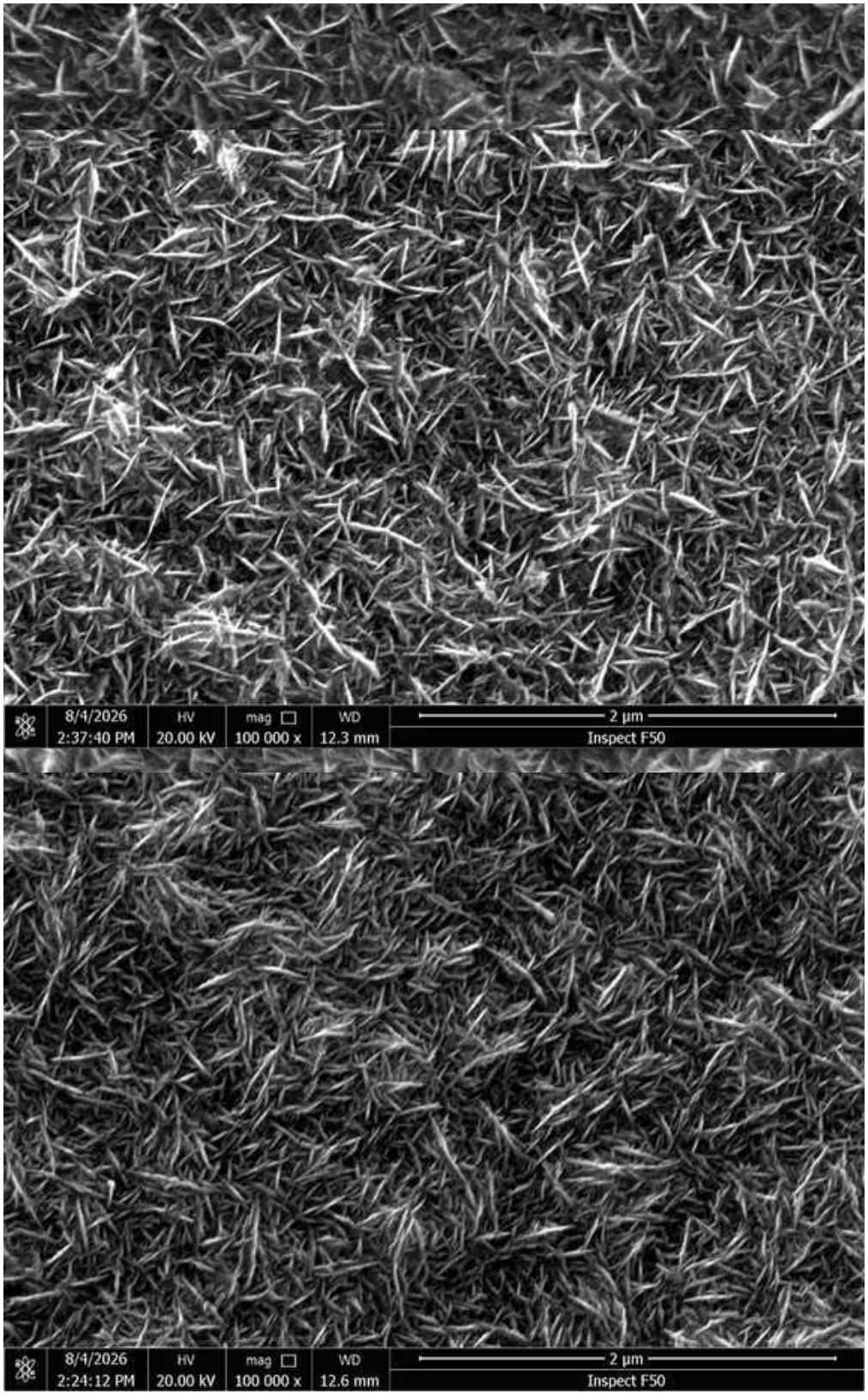
(19)



(20) **Figure 19.** SEM images of Ni/M-Xene coatings electrodeposited from the Ethalinebased electrolyte at 30 – 60 °C for 20 min under different current densities. Magnification: 30k×; scale bar: 5 µm. Sample numbers correspond to the electrodeposition parameters listed in Table 3.



(1)

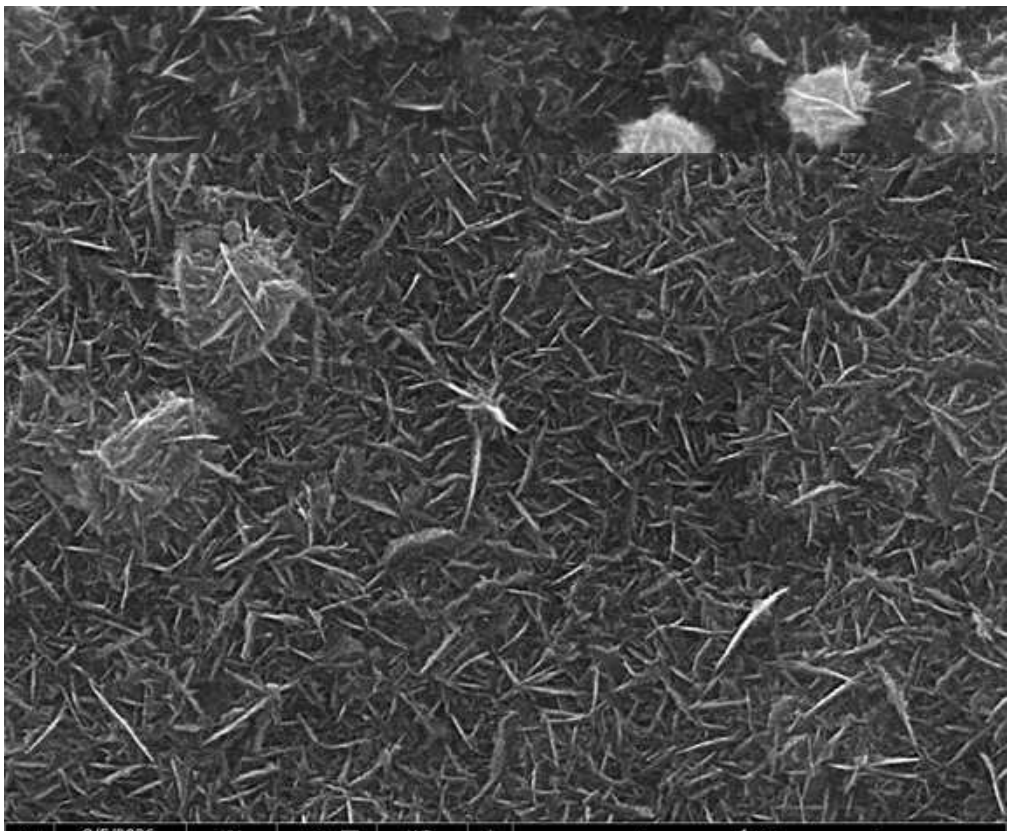

8/4/2026
2:37:40 PM
HV
20.00 kV
mag
100 000 x
WD
12.3 mm
2 µm
Inspect F50
8/4/2026
2:24:12 PM
HV
20.00 kV
mag
100 000 x
WD
12.6 mm
2 µm
Inspect F50

(2)

(3)

(4)

(5)

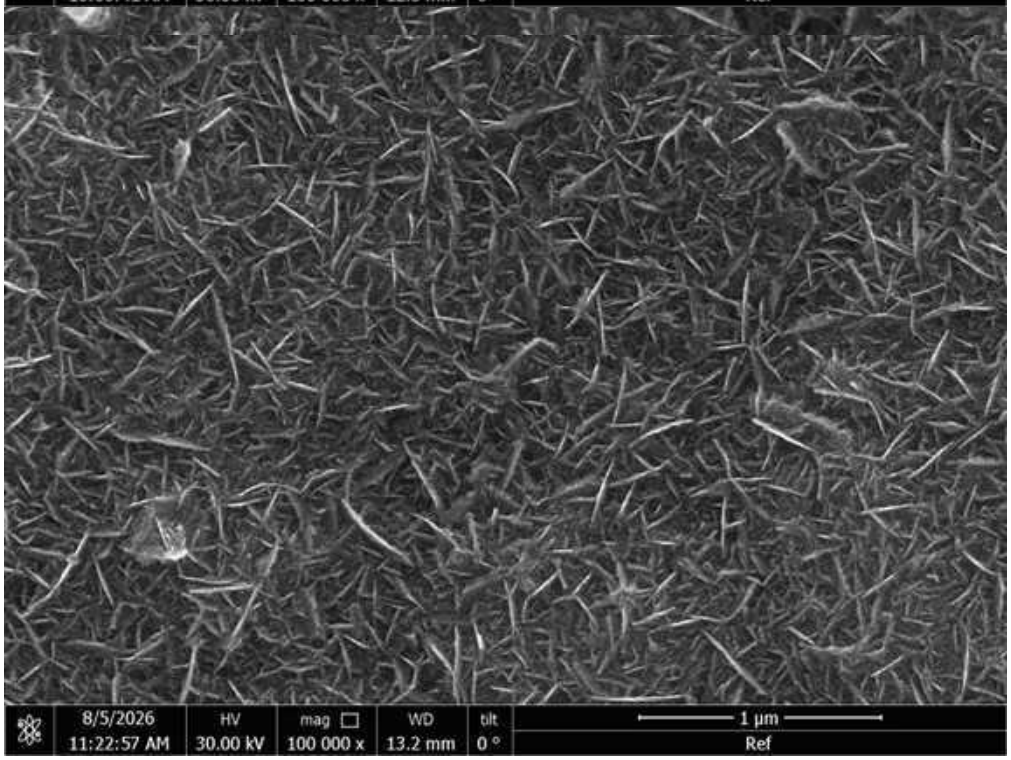


(6)

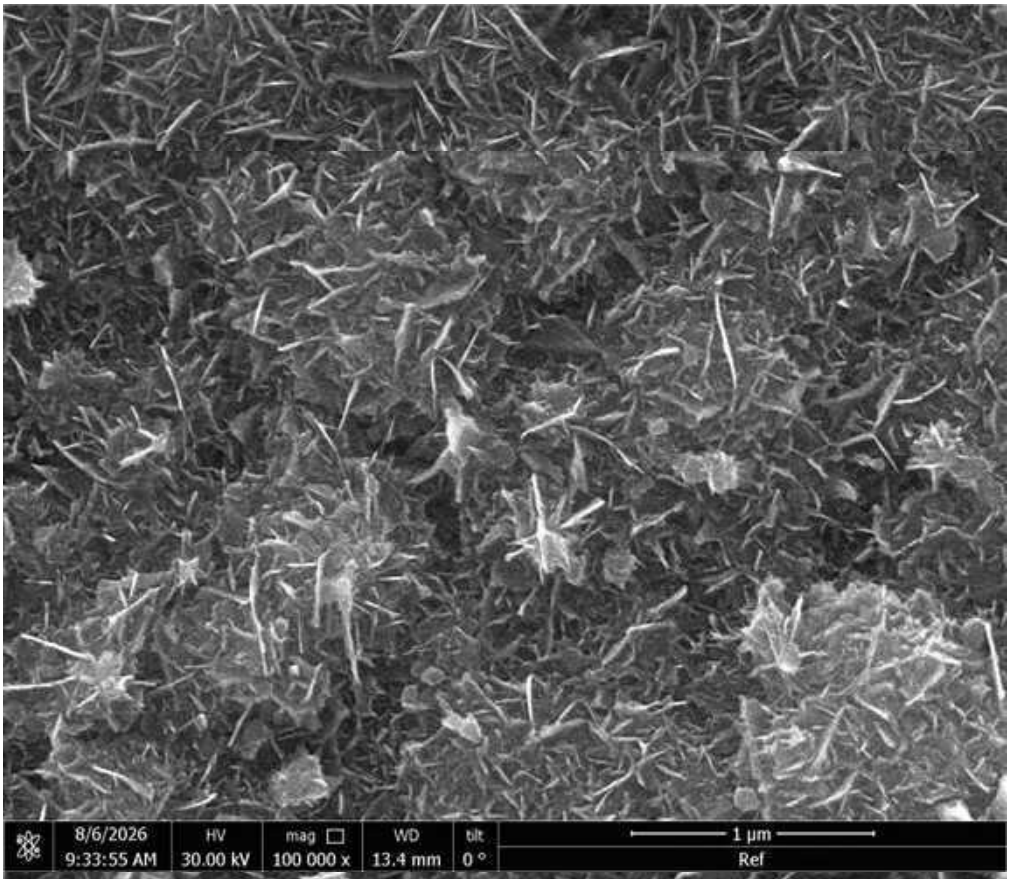

8/5/2026
10:00:41 AM
HV
30.00 kV
mag
100 000 x
WD
12.5 mm
tilt
0 °
1 µm
Ref

(7)

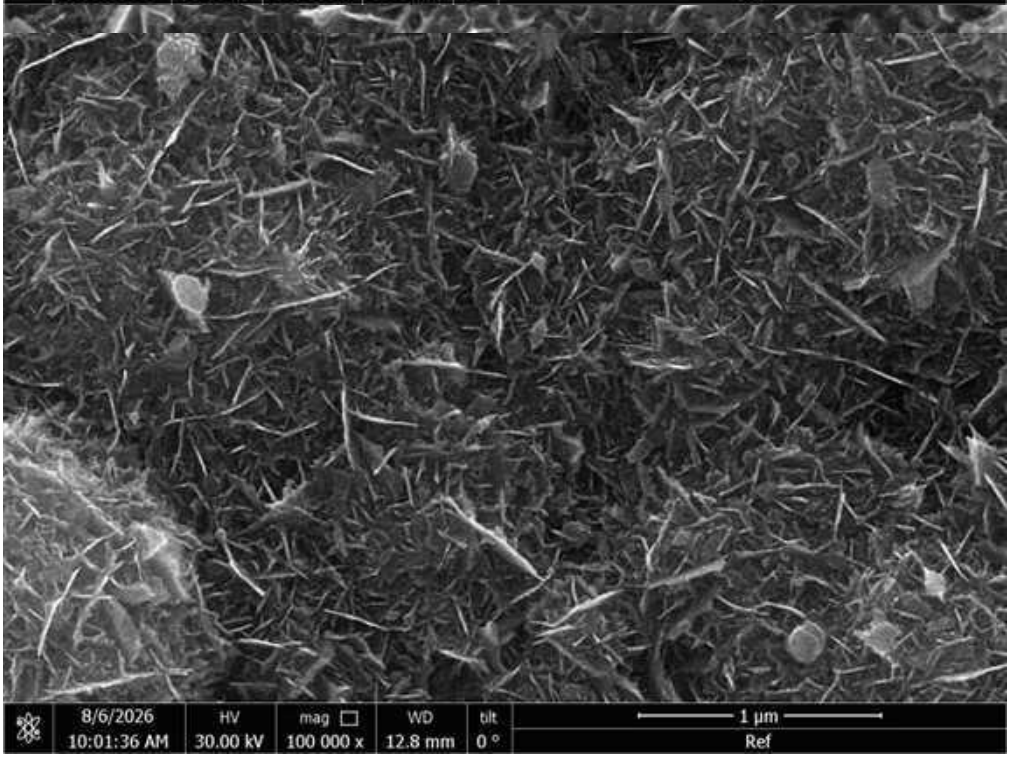
(8)


8/5/2026
11:22:57 AM
HV
30.00 kV
mag
100 000 x
WD
13.2 mm
tilt
0 °
1 µm
Ref

(9)



(10)

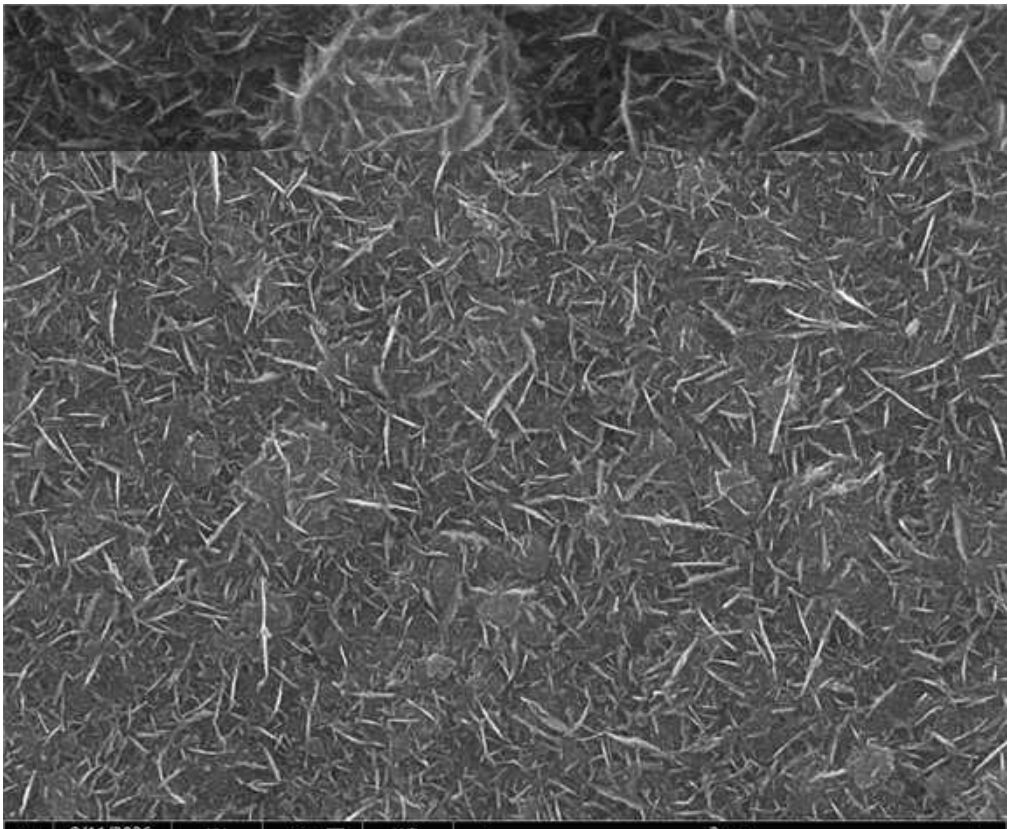

8/6/2026
9:33:55 AM
HV
30.00 kV
mag
100 000 x
WD
13.4 mm
tilt
0 °
1 µm
Ref

(11)

(12)

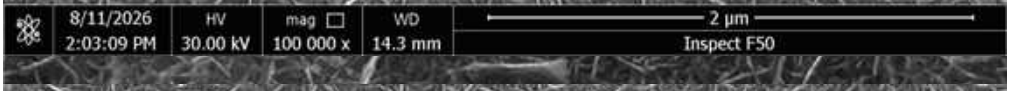
8/6/2026
10:01:36 AM
HV
30.00 kV
mag
100 000 x
WD
12.8 mm
tilt
0 °
1 µm
Ref

(13)

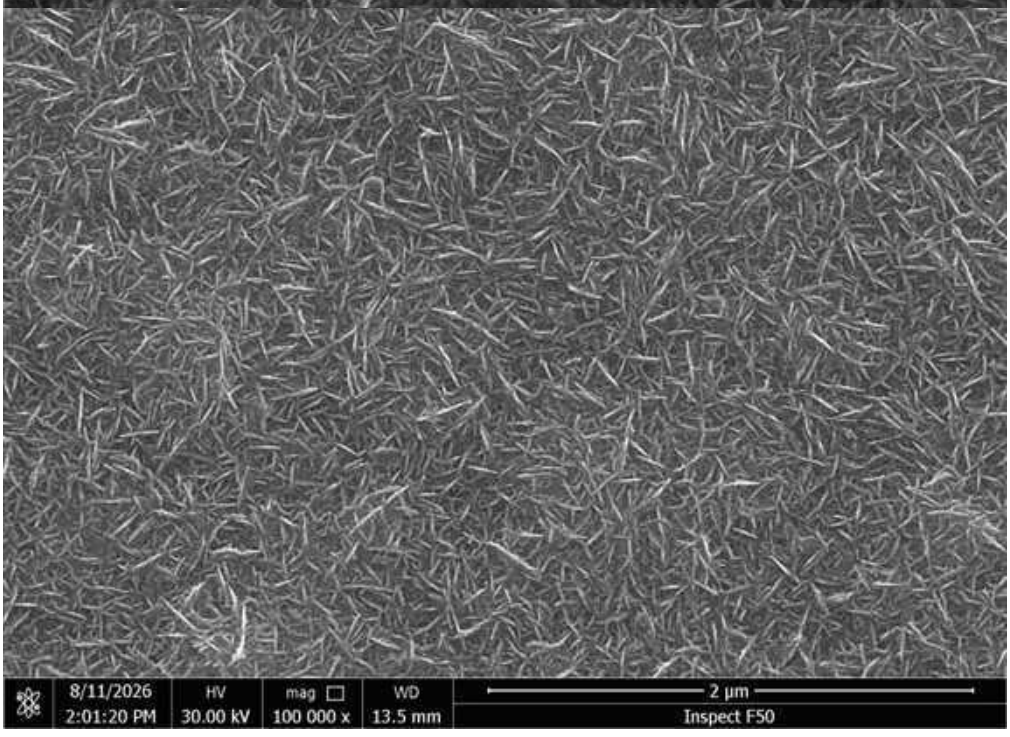


(14)

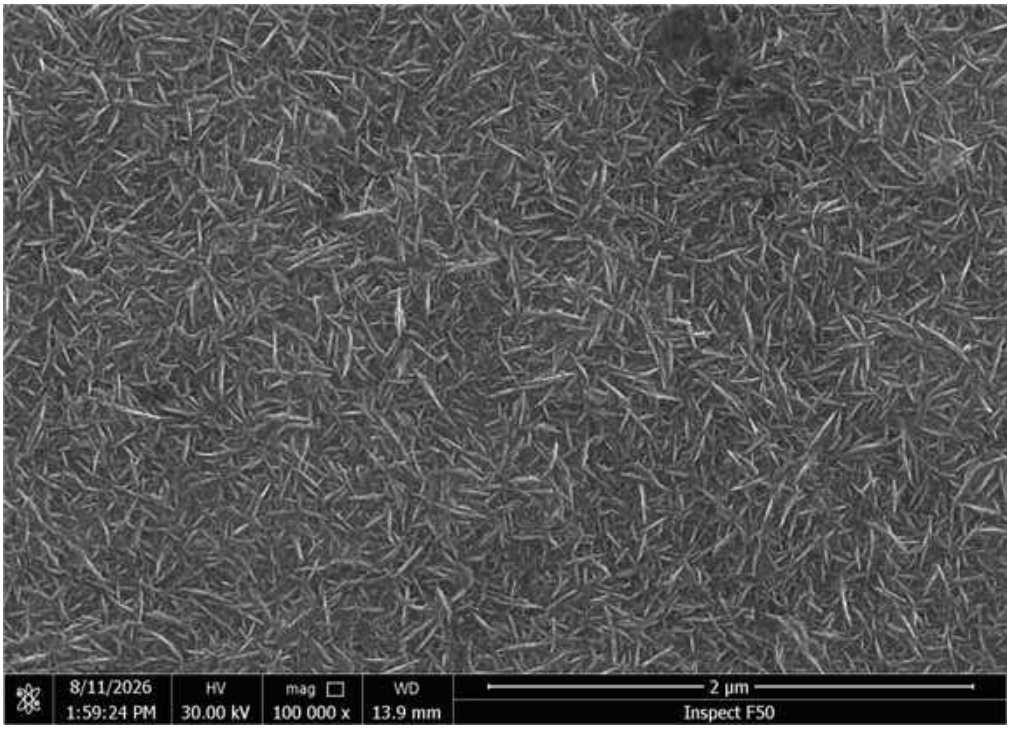
(15)


8/11/2026
2:03:09 PM
HV
30.00 kV
mag
100 000 x
WD
14.3 mm
2 µm
Inspect F50

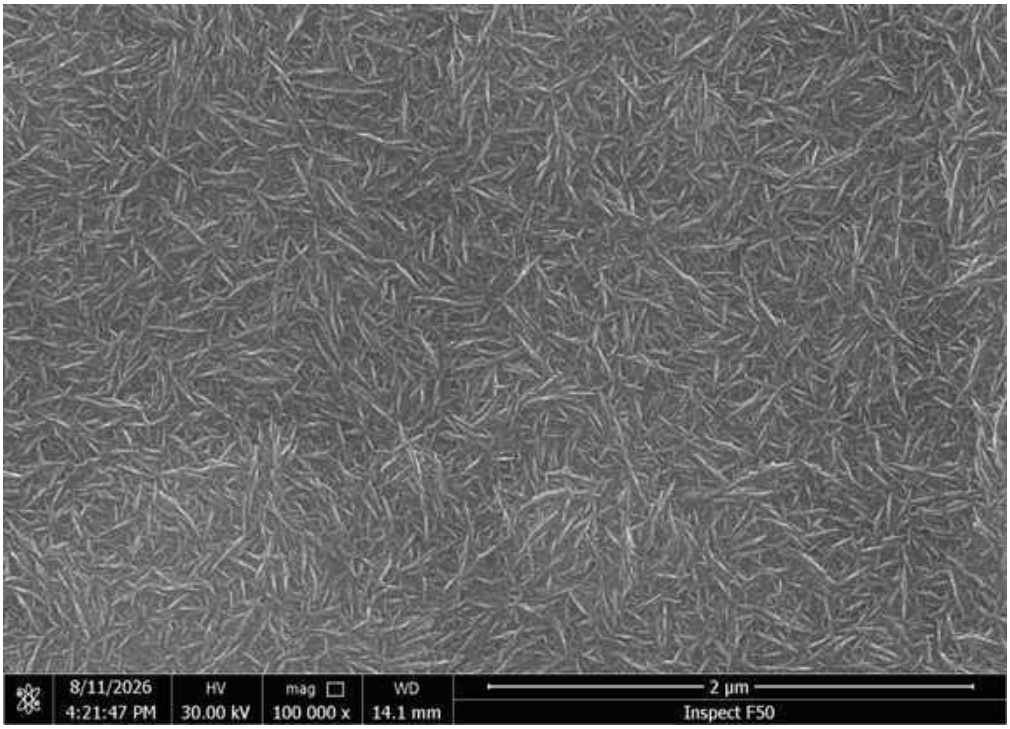
(16)


8/11/2026
2:01:20 PM
HV
30.00 kV
mag
100 000 x
WD
13.5 mm
2 µm
Inspect F50

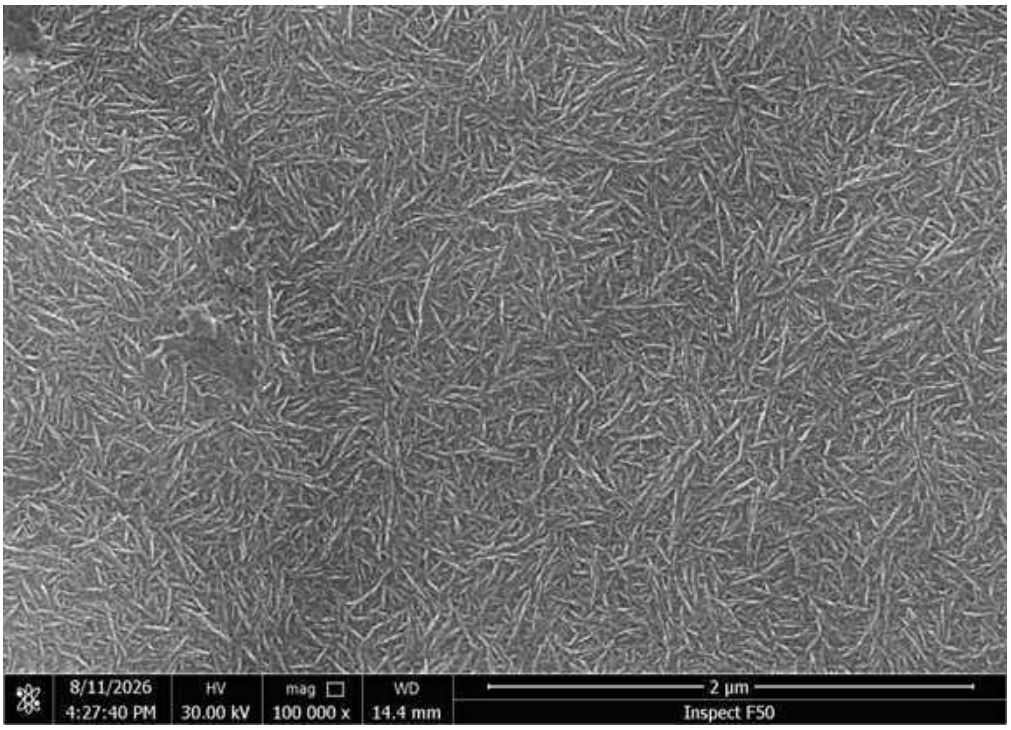
(17)


8/11/2026
1:59:24 PM
HV
30.00 kV
mag
100 000 x
WD
13.9 mm
2 µm
Inspect F50

(18)


8/11/2026
4:21:47 PM
HV
30.00 kV
mag
100 000 x
WD
14.1 mm
2 µm
Inspect F50

(19)



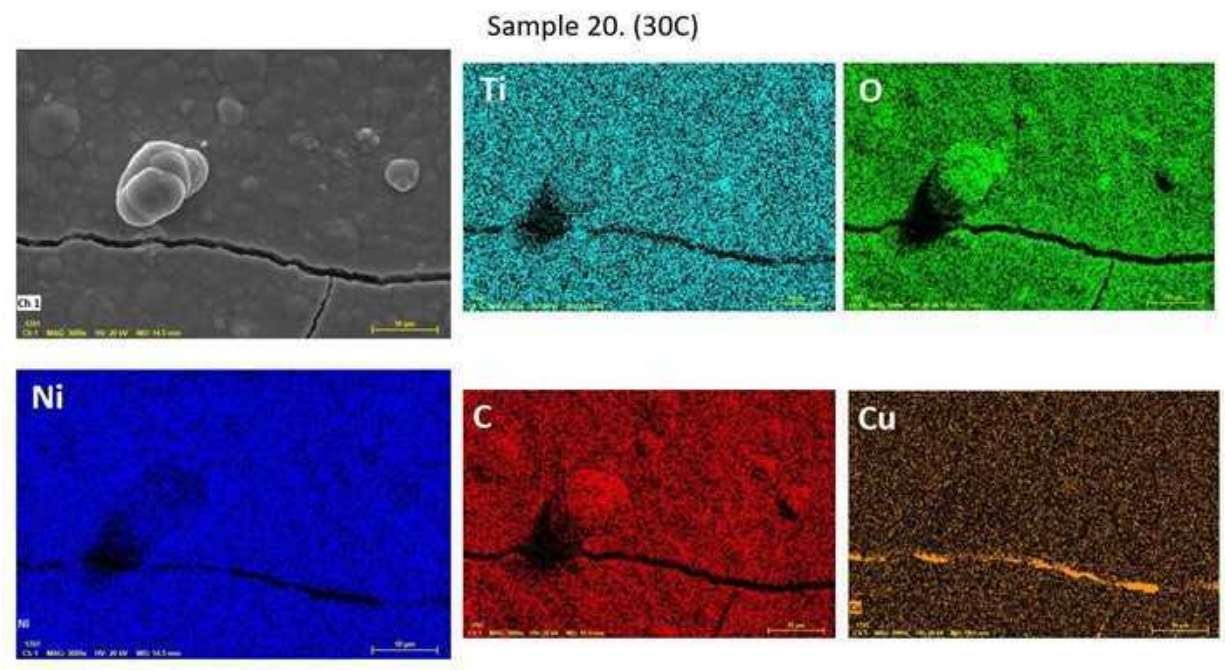
(20)

Figure 20. SEM images of Ni/M-Xene coatings electrodeposited from the Ethalinebased electrolyte at 30 – 60 °C for 20 min under different current densities. Magnification: 100k×; scale bar: 1 µm. Sample numbers correspond to the electrodeposition parameters listed in Table 3.

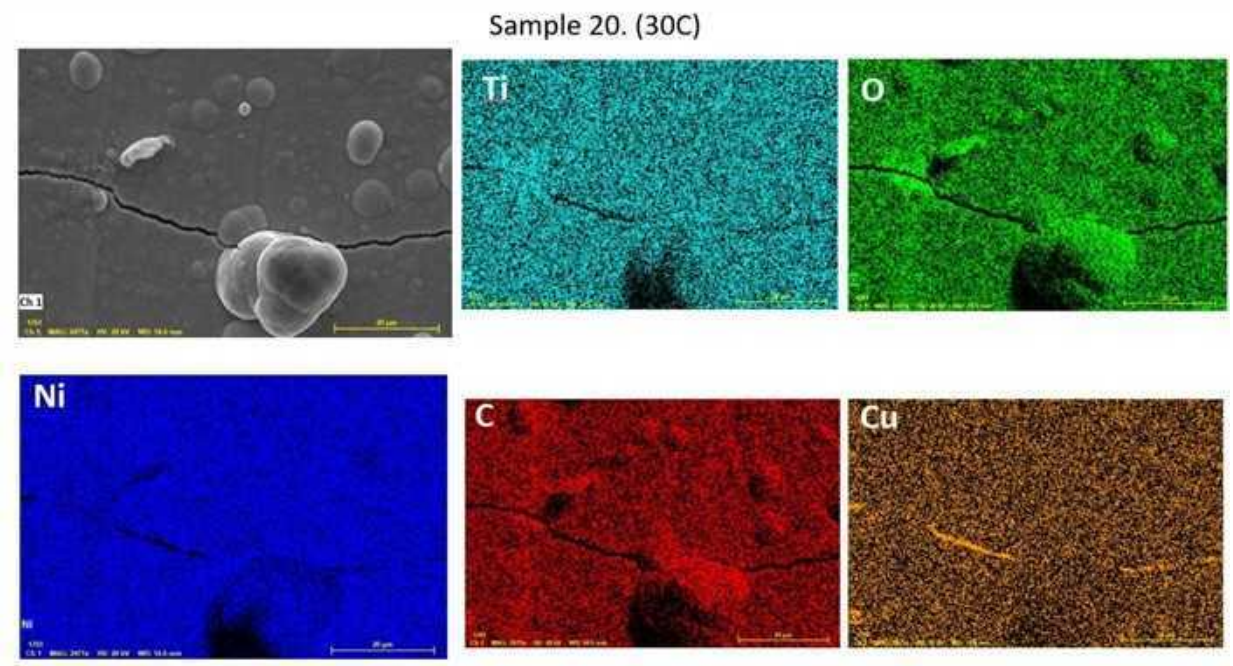
Comparison of the SEM images with the electrodeposition parameters presented in Table 3 indicates a relationship between the applied deposition conditions and the resulting surface morphology. Both current density and electrolyte temperature affect the development of the Ni matrix and therefore the final morphology of the Ni/MXene composite coating. In general, modification of these parameters changes the relative contribution of nucleation and subsequent growth, resulting in differences in surface roughness, characteristic feature size, and coating homogeneity. The observed morphological variations demonstrate that the structure of Ni/MXene coatings can be controlled to some extent through optimization of the electrodeposition conditions.

As observed previously for the Ni and Ni/MoS_2 systems, the formation of cracks becomes an important consideration under deposition conditions that promote rapid coating growth. The SEM observations of the Ni/MXene series similarly indicate that coating integrity must be considered together with the development of the micro-/nanostructured surface. Consequently, conditions providing a structurally developed surface while limiting crack formation should be preferred for further optimization.

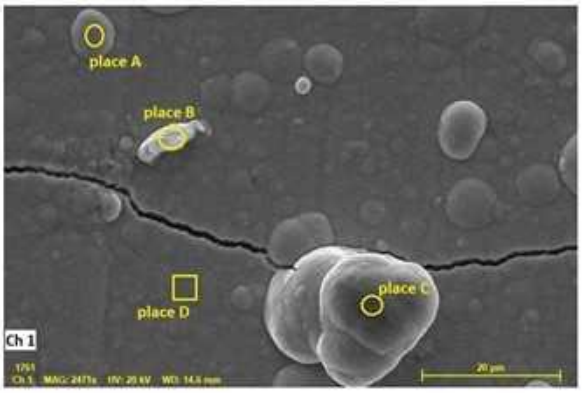
In addition to SEM characterization, EDX analysis was performed to evaluate the elemental composition of the Ni/MXene coatings and, in particular, to verify the incorporation of the MXene-containing phase into the Ni matrix. A more detailed SEM/EDX investigation is presented for sample 20, electrodeposited at 30 °C and 25 mA cm^{-2} according to Table 3. Elemental maps and local EDX analyses obtained from different regions of this coating are shown in Figure 21.



(a)



(b)



Place A

Element	Atomic number	Net counts	Mass Concentration /%	Norm. mass concentration /%	Norm. atomic concentration /%	1σ uncertainty /mass%	1σ rel. uncertainty /%
Carbon	6	7915	5.06	5.21	20.64	0.15	3.00
Oxygen	8	6710	1.16	1.19	3.55	0.04	3.43
Titanium	22	0	0.00	0.00	0.00	0.00	100.76
Nickel	28	680458	89.89	92.58	75.05	1.32	1.47
Copper	29	5755	0.99	1.02	0.76	0.03	3.34
		Sum	**97.09**	**100.00**	**100.00**		

Place B

Element	Atomic number	Net counts	Mass Concentration /%	Norm. mass concentration /%	Norm. atomic concentration /%	1σ uncertainty /mass%	1σ rel. uncertainty /%
Carbon	6	22792	11.70	11.95	36.82	0.27	2.31
Oxygen	8	26691	4.44	4.54	10.50	0.09	2.06
Titanium	22	6918	0.42	0.43	0.33	0.01	3.41
Nickel	28	688507	80.41	82.17	51.81	1.17	1.45
Copper	29	5953	0.89	0.91	0.53	0.03	3.32
		Sum	**97.86**	**100.00**	**100.00**		

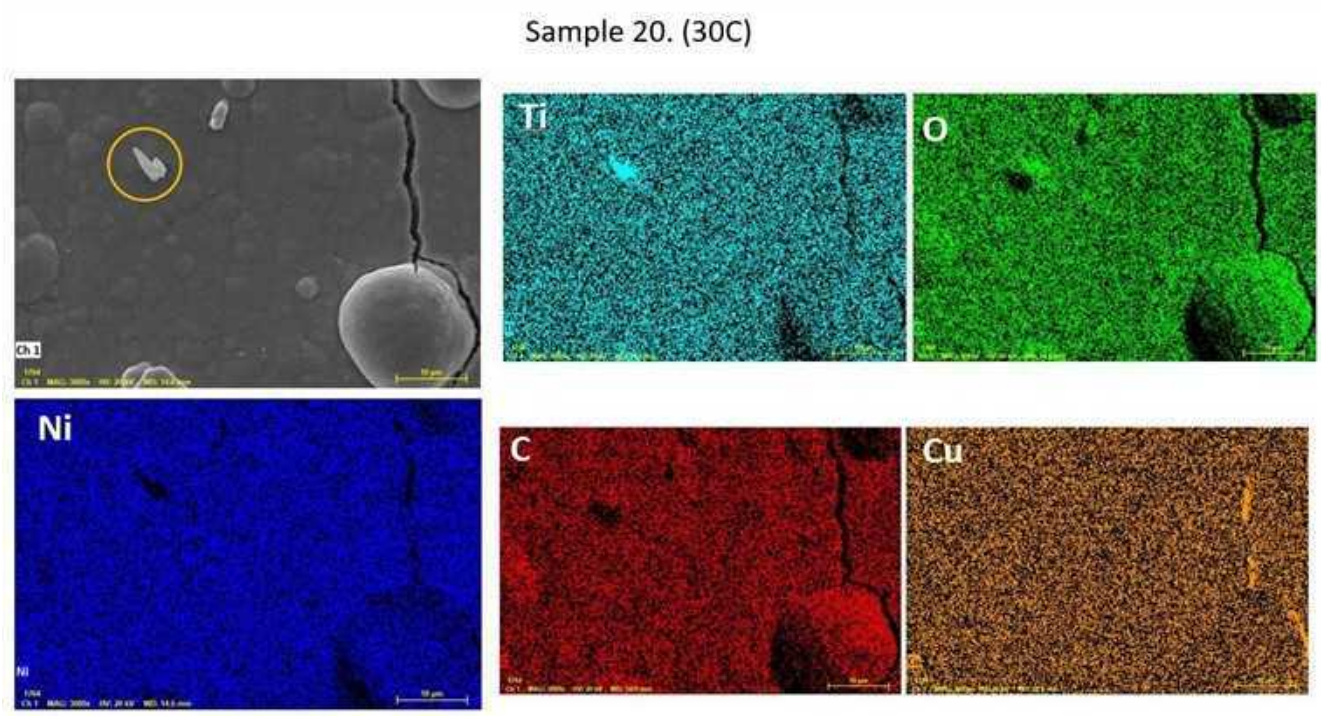
Place C

Element	Atomic number	Net counts	Mass Concentration /%	Norm. mass concentration /%	Norm. atomic concentration /%	1σ uncertainty /mass%	1σ rel. uncertainty /%
Carbon	6	11366	10.17	10.63	34.71	0.24	2.40
Oxygen	8	10795	3.00	3.13	7.67	0.07	2.28
Titanium	22	749	0.08	0.08	0.07	0.01	14.92
Nickel	28	411564	81.70	85.34	57.04	1.38	1.68
Copper	29	3066	0.78	0.82	0.51	0.03	4.43
		Sum	**95.73**	**100.00**	**100.00**		

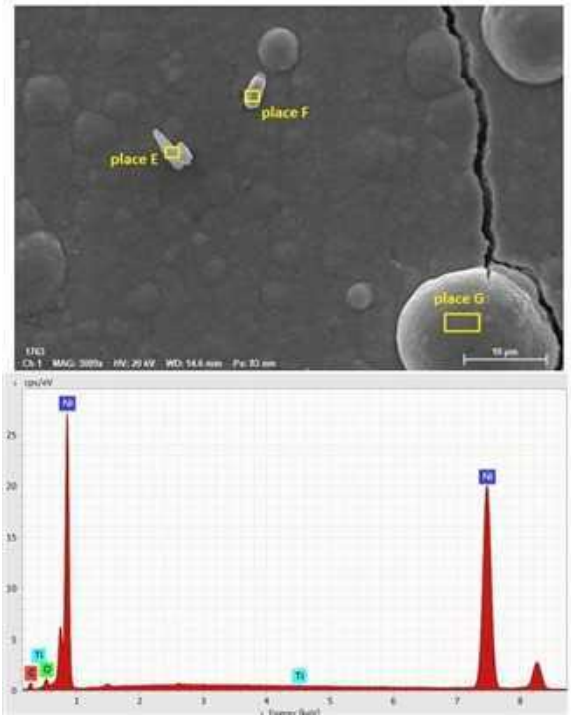
Place D

Element	Atomic number	Net counts	Mass Concentration /%	Norm. mass concentration /%	Norm. atomic concentration /%	1σ uncertainty /mass%	1σ rel. uncertainty /%
Carbon	6	10765	6.01	6.18	23.85	0.15	2.44
Oxygen	8	6399	0.99	1.02	2.94	0.03	2.93
Titanium	22	0	0.00	0.00	0.00	0.00	100.78
Nickel	28	766908	89.29	91.79	72.47	1.27	1.42
Copper	29	6600	0.99	1.01	0.74	0.03	3.15
		Sum	**97.28**	**100.00**	**100.00**		

(c)



(d)



Place E

Element	Atomic number	Net counts	Mass Concentration /%	Norm. mass concentration /%	Norm. atomic concentration /%	1σ uncertainty /mass%	1σ rel. uncertainty /%
Carbon	6	13657	9.08	9.02	28.00	0.22	2.37
Oxygen	8	29730	7.71	7.66	17.85	0.16	2.07
Titanium	22	109931	8.87	8.82	6.86	0.14	1.60
Nickel	28	480991	74.12	73.64	46.78	1.17	1.58
Copper	29	4410	0.87	0.86	0.51	0.03	3.72
		Sum	100.65	100.00	100.00		

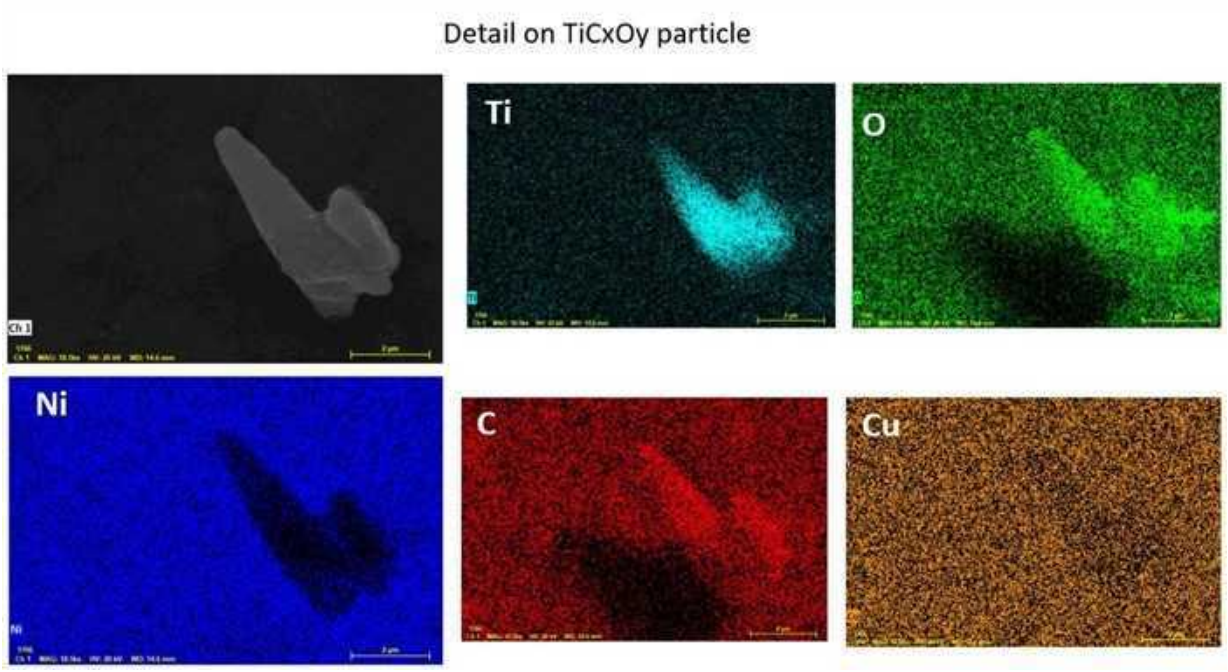
Place F

Element	Atomic number	Net counts	Mass Concentration /%	Norm. mass concentration /%	Norm. atomic concentration /%	1σ uncertainty /mass%	1σ rel. uncertainty /%
Carbon	6	16896	6.82	6.92	25.54	0.16	2.35
Oxygen	8	17872	2.05	2.08	5.76	0.04	2.18
Titanium	22	5088	0.23	0.23	0.21	0.01	4.61
Nickel	28	1034341	88.46	89.73	67.76	1.16	1.31
Copper	29	9130	1.03	1.04	0.73	0.03	2.75
		Sum	98.59	100.00	100.00		

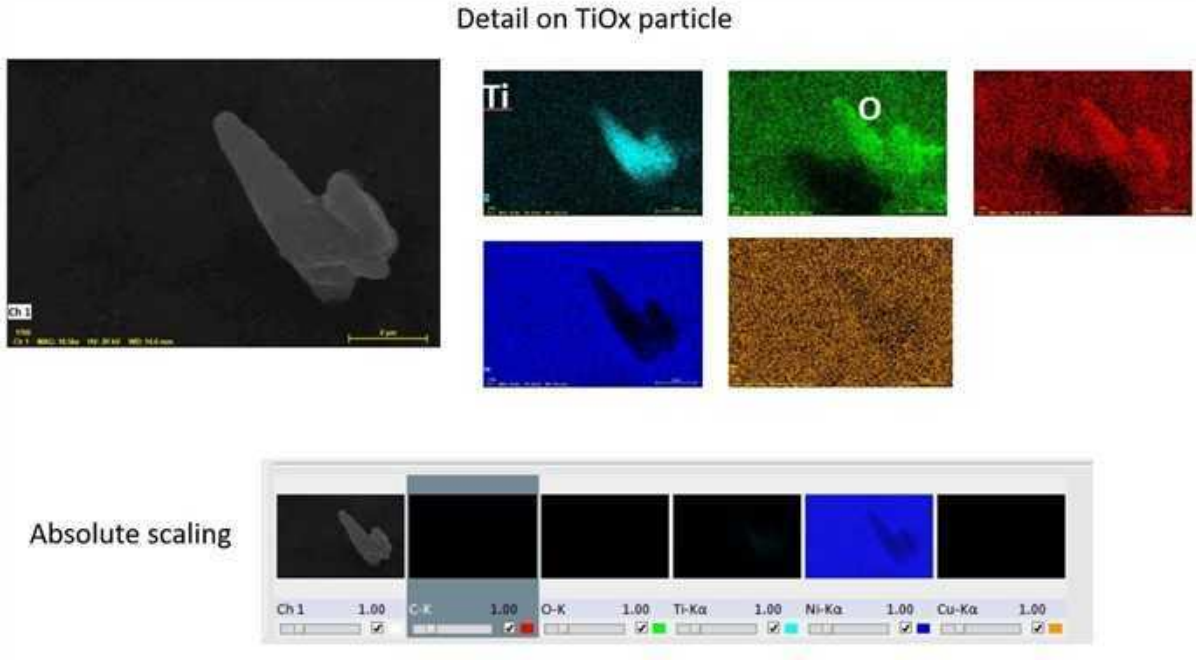
Place G

Element	Atomic number	Net counts	Mass Concentration /%	Norm. mass concentration /%	Norm. atomic concentration /%	1σ uncertainty /mass%	1σ rel. uncertainty /%
Carbon	6	7242	4.13	4.32	17.59	0.12	3.02
Oxygen	8	7594	1.14	1.20	3.66	0.03	3.06
Titanium	22	419	0.03	0.03	0.03	0.01	33.27
Nickel	28	766098	89.44	93.51	77.98	1.28	1.43
Copper	29	5947	0.91	0.95	0.73	0.03	3.35
		Sum	95.65	100.00	100.00		

(e)



(f)



(g)

Figure 21. SEM images, EDX elemental maps, and local compositional analysis of the Ni/MXene composite coating (sample 20) electrodeposited from the Ethalinebased electrolyte at 30 °C and 25 mA cm^{-2} for 20 min.

Figure 21 shows SEM images together with elemental distribution maps for Ti, O, Ni, C, and Cu and local EDX analyses performed at selected positions. The Ni signal is distributed over the coating surface, confirming the formation of the Nibased matrix, whereas the Cu signal is associated with the underlying Cu substrate and becomes particularly evident in regions where cracks expose or approach the substrate. Carbon is distributed across the analyzed area and can originate from both the MXene-containing phase and organic components of the Ethaline-based electrolyte. The Ti-containing regions are of particular importance because Ti serves as an indicator of the presence of the MXene-derived phase.

A correlation between the morphology of individual surface particles and their elemental composition can be identified from the SEM/EDX maps in Figure 21. In particular, some particle-like features observed by SEM correspond to locally enhanced Ti, C and O signals, while the Ni signal is reduced in the same regions. Detailed mapping of an individual Ti-rich particle further confirms that the Ti signal is concentrated within this feature rather than being uniformly distributed throughout the surrounding Ni matrix. These observations provide evidence for the presence and local incorporation of MXene-derived particles in the electrodeposited coating. At the same time, the localized character of the Ti-rich regions suggests that the distribution and overall amount of incorporated MXene remain limited under the investigated electrodeposition conditions.

The results therefore indicate that MXene-containing particles can be incorporated into the Ni coating during electrodeposition from the Ethaline-based electrolyte; however, a higher MXene content in the composite coating is desirable to increase the contribution of the MXene phase to the surface composition and potentially improve the functional and electrocatalytic properties of the material.

Increasing the MXene concentration in the electrolyte alone may not be sufficient, because incorporation also depends on the transport of suspended particles toward the cathode, their adsorption at the electrode surface, and their subsequent entrapment within the growing Ni layer.

Accordingly, the next stage of the investigation will focus on electrodeposition under continuous stirring of the electrolyte. Stirring is expected to improve suspension stability and enhance the transport of MXene particles toward the cathode, thereby increasing the probability of their incorporation into the growing Ni matrix. The influence of stirring rate should be investigated systematically while maintaining the other electrodeposition parameters constant. The resulting coatings should then be compared in terms of MXene content, elemental distribution, surface morphology, coating integrity, and catalytic performance. This approach will allow the relationship between hydrodynamic conditions and MXene incorporation efficiency to be established and will provide a basis for further optimization of Ni/MXene composite coatings.

1.5 Morphological and elemental analysis of $Ni_{1-x}Co_xS$ catalysts

Scanning electron microscopy (SEM) was employed to examine the morphology of the synthesized $Ni_{1-x}Co_xS$ materials, while energy-dispersive X-ray spectroscopy (EDX) mapping and semi-quantitative analysis were utilized to assess the element distribution and composition. As the morphology appeared nearly identical across the synthesized materials, Figure 22 shows representative SEM images of $Ni_{0.4}Co_{0.6}S$, selected as the best-performing catalyst. SEM images revealed that all samples consist of well-separated agglomerates of different sizes ≤500 nm with irregular, sharp-edged structures resembling fractured “rocks” with smooth surfaces and no visible pores.

The elemental mapping showed a uniform distribution of Ni, Co, and S at the microscopic scale, with no significant segregation (Figure 22d). The semiquantitative EDX results indicated that the Ni/Co ratios in the synthesized materials were close to the nominal values (Figure 22e). However, the total metal content was slightly higher relative to sulfur than expected. This deviation can be attributed to partial sulfur loss during the MSR event, which may occur due to the local temperature increase. The specific rotten egg smell of sulfur was noted upon opening the milling chamber, supporting the assumption of sulfur volatilization. In addition, the low oxygen content (1.91 at. %) indicated that oxide phases were not formed, despite milling in an air atmosphere. Both the minor sulfur deficiency and absence of oxide phases are consistent with previously reported MSR synthesis of metal chalcogenides in published literature.

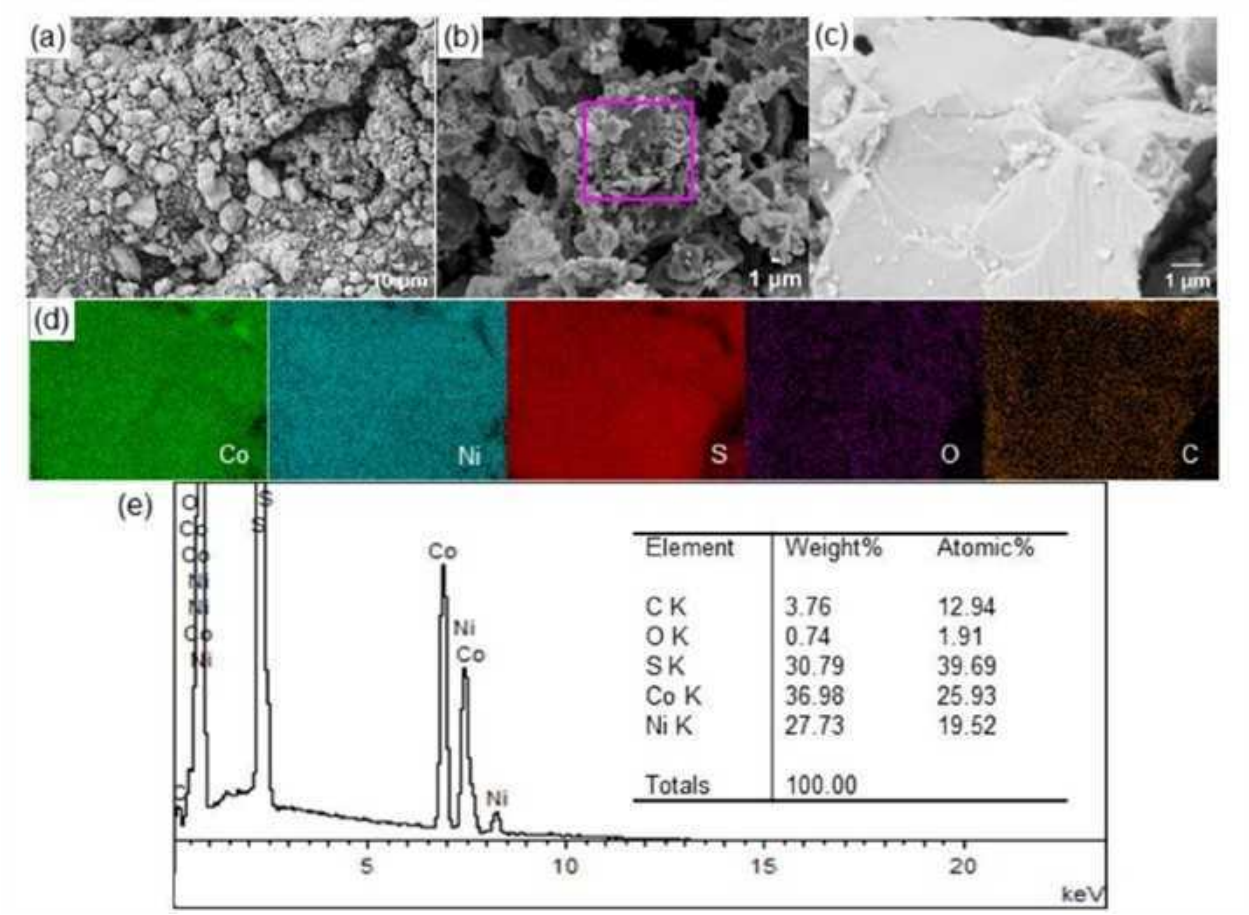


Figure 22. (a–c) SEM images of the $Ni_{0.4}Co_{0.6}S$ sample recorded at different magnifications. (d) EDX elemental mapping acquired from the region shown in panel c. (e) EDX compositional analysis (at. %) corresponding to the rectangular area marked in panel b.

XRD analysis of all prepared catalysts was performed to identify the crystalline phases formed during MSR synthesis. It was found that the phase composition strongly depends on the Ni/Co ratio, with characteristic similarities observed among the samples with low, medium, and high Co content (Figures 23–25). Specifically, the low Co content sample ($Ni_{0.9}Co_{0.1}S$) exhibits an almost identical XRD pattern to that of the NiS reference sample (Figure 23), indicating a small amount of cobalt is effectively incorporated into the structure, without altering it. According to database

reference, these samples are predominately composited of the Ni_7S_6 phase (ICDD 00-051-0718; monoclinic system; a = 6.24 Å, b = 16.42 Å, c = 11.59 Å), with minor amounts of the NiS (ICDD 00-003-0760; rhombohedral system, a = 9.62 Å, b = 9.62 Å, c = 3.16 Å), and NiS_2 (ICDD 00-003-0734; cubic system a = 5.67 Å, b = 5.67 Å, c = 5.67 Å) phases. This formation of multiple phases is consistent with previously published studies, which showed that targeted stoichiometry in MSR synthesis rarely yields a pure single–phase product and most often results in a mixture of phases. Despite this similarity in phase composition, all reflections in Ni0.9Co0.1S are slightly shifted toward higher 2θ values compared to the NiS reference sample, which suggests incorporation of Co into the nickel-sulfide lattices and formation of mixed Ni–Co sulfide phases.

In contrast, samples with high cobalt content, such as $Ni_{0.5}Co_{0.5}S$ and $Ni_{0.4}Co_{0.6}S$, display diffraction patterns that significantly differ from those of Ni0.9Co0.1S and NiS (Figure 24). Such changes in phase composition are consistent with reports on binary MSR systems, which demonstrate that variation in precursor stoichiometry dictates the resulting phase composition. Diffractograms of the high Co content samples closely resemble the diffraction pattern of the CoS reference sample (Figure 24), and according to the database reference, they are composed of Co9S8 (ICDD 03-065-6801; cubic system; a = 9.93 Å, b = 9.93 Å, c = 9.93 Å) and CoS (ICDD 01-075-0605; hexagonal; a = 3.38 Å, b = 3.38 Å, c = 5.16 Å phases). Similar to $Ni_{0.9}Co_{0.1}S$, the high Co content samples also exhibit a shift in reflection compared with the CoS reference sample, but in this case toward lower 2θ values. This peak shift supports the conclusion that mixed Ni–Co sulfides are formed during the MSR synthesis of Ni–Co–S samples. However, unlike $Ni_{0.9}Co_{0.1}S$, where Co is

incorporated into the nickel sulfide lattice, in the high Co content samples, the trend is reversed, and Ni becomes incorporated into the cobalt sulfide lattice, leading to the formation of a mixed Ni–Co sulfide phases in both cases rather than separated Ni- and Co-sulfide phases. This interpretation is supported by EDX elemental mapping, which confirmed a homogeneous spatial distribution of Ni and Co across the samples (Figure 22d).

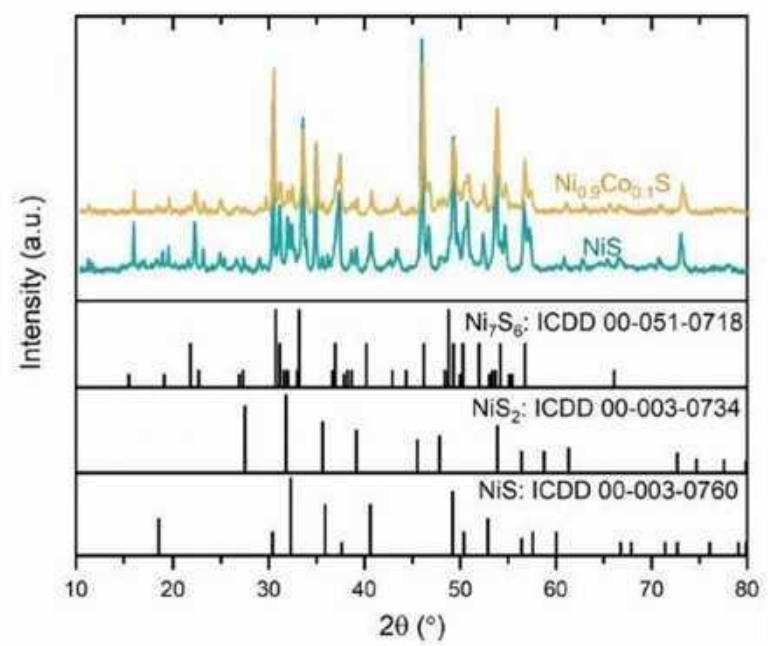


Figure 23. XRD patterns of the low Co content sample together with the NiS reference sample.

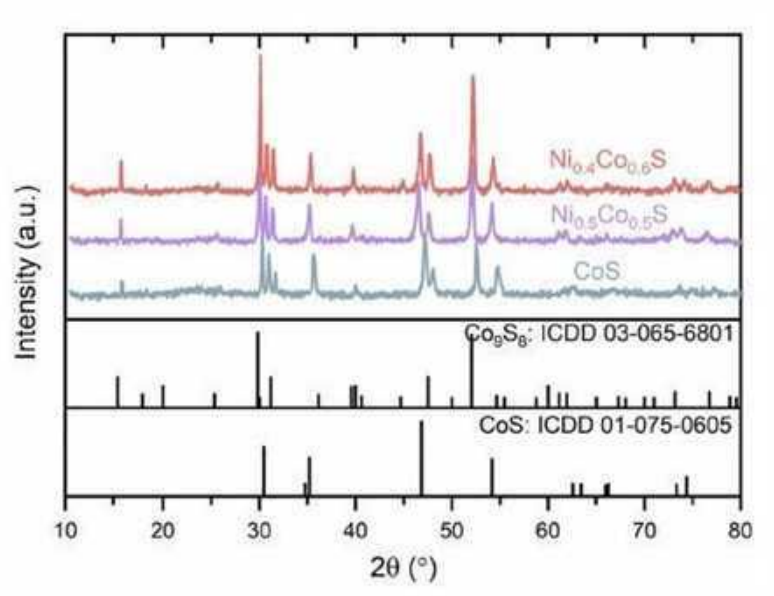


Figure 24. XRD patterns of the high Co content samples together with the CoS reference sample.

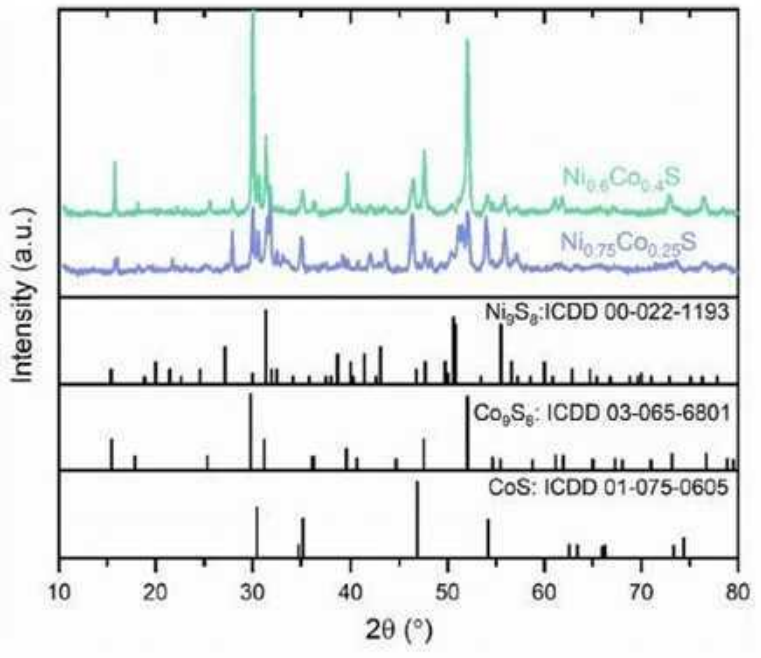


Figure 25. XRD patterns of the medium Co content samples.

The medium Co content samples displayed diffraction features characteristic of a multiphase mixture consisting of Co_9S_8, CoS, and Ni_9S_8 (ICDD 00-022-1193; orthorhombic; a = 9.18 Å, b = 11.26 Å, c = 9.46 Å phases). Based on the cation substitution behavior observed in both low and high Co content samples, it is reasonable to assume that these phases are also mixed Ni–Co sulfide phases rather than separated Co and Ni sulfides. The relative intensities of the characteristic reflections indicated that $Ni_{0.75}Co_{0.25}$ is predominantly composed of Ni_9S_8-type phases, whereas $Ni_{0.6}Co_{0.4}S$ predominantly contains Co_9S_8-type phases with a noticeable amount of CoS-type phases in both samples.

To exclude the possibility that the observed changes in phase composition arise from differences in Co particle size rather than from changes in Ni/Co ratio, additional control experiments were performed. Since the optimal $Ni_{0.4}Co_{0.6}S$ composition can only be ignited using fine cobalt, the $Ni_{0.9}Co_{0.1}S$ was selected as a control model because it can be successfully synthesized using both coarse and fine Co precursors.

TEM analysis was primarily performed on the $Ni_{0.4}Co_{0.6}S$ sample, which exhibited the best electrochemical performance, to confirm the phase composition inferred from XRD analysis. The TEM analysis revealed that it consists of grains from two phases, Co_9S_8 and CoS. This finding corroborates the results obtained from XRD analysis. Figure 26 displays the microstructure of the $Ni_{0.4}Co_{0.6}S$ sample, clearly showing grains of both phases. Phase identification was performed using SAED, initially at low magnification from a large number of grains of both phases simultaneously. The resulting ring diffraction pattern, following radial integration (1D diffraction profile shown as a white line), enabled distinction of both phases with no others present. Subsequent spot diffraction patterns, acquired from

individual grains of Co_9S_8 and CoS phases, provided more precise confirmation, supported by multiple spot diffraction patterns obtained along various zone axes.

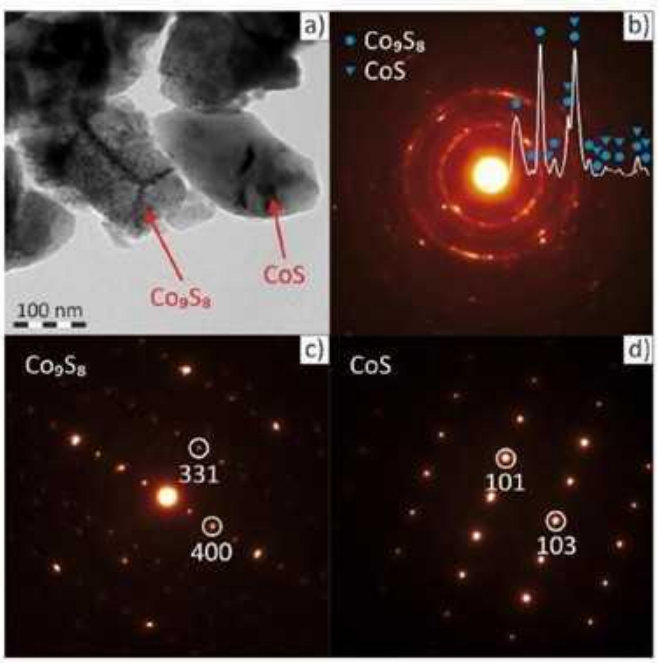


Figure 26. (a) TEM image of the $Ni_{0.4}Co_{0.6}S$ microstructure showing Co_9S_8 and CoS grains, (b) ring diffraction pattern obtained from a larger number of grains of both phases, (c) and (d) Spot diffraction patterns of the individual phases. XPS was employed to investigate the surface chemical states of the MSR-derived $Ni_{0.4}Co_{0.6}S$ catalyst, Figure 27.

XPS was employed to investigate the surface chemical states of the MSR-derived $Ni_{0.4}Co_{0.6}S$ catalyst, Figure 27.

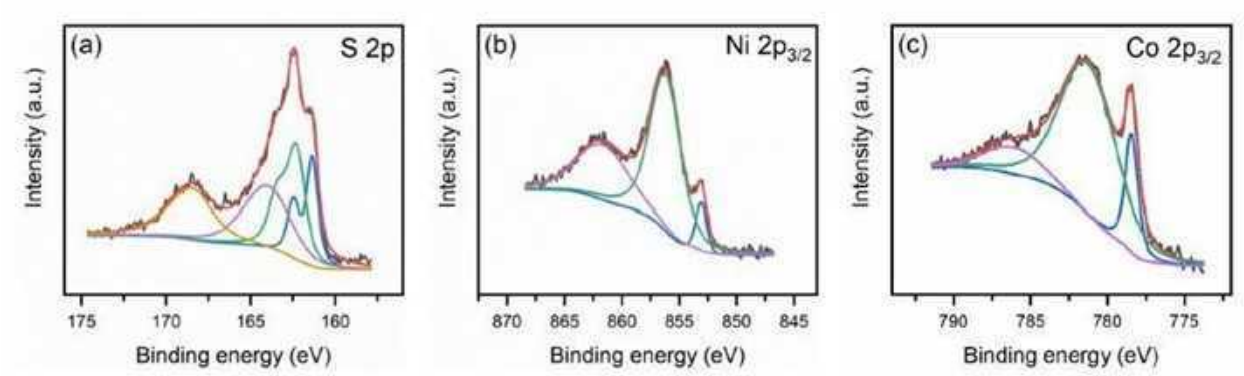


Figure 27. High-resolution XPS spectra of the $Ni_{0.4}Co_{0.6}S$ sample: (a) S 2p, (b) Ni $2p_{3/2}$, and (c) Co $2p_{3/2}$.

The S 2p spectrum (Figure 27a), with a pronounced peak at 162.4 eV characteristic for metal–sulfur bonding, confirmed that the synthesized sample is predominantly sulfide in nature. Only a weak contribution at higher binding energies at 168.5 eV, attributed to Sox species, indicated mild surface oxidation upon the exposiure to the air. Deconvolution of the main S 2p peak further revealed the coexistence of apical S^{2-} , bridging S_2^{2-}, and S^{2-} with low coordination, indicating the presence of defects.

High-resolution Ni and Co core-level regions (Ni $2p_{3/2}$ and Co $2p_{3/2}$) were analyzed to evaluate the oxidation state of metal centers.

In the Ni $2p_{3/2}$ spectrum (Figure 27b), the dominant peak at 856.2 eV is assigned to Ni^{2+} species, accompanied by a characteristic shake-up satellite at 861.7 eV. In addition, a weak contribution close to zerovalent binding energy at 853.1 eV is observed. Based on previous reports, this peak is attributed to Ni^0-like states modified by the surrounding sulfur environment rather than from residual metallic Ni.

The absence of elemental Ni is further confirmed by XRD analysis. Such Ni^0like states are observed in Ni-rich sulfides (e.g., Ni_3S_2) and are associated with Ni– Ni interaction within the sulfide lattice. The Co $2p_{3/2}$ spectrum (Figure 27c) exhibits two

main peaks at 775 and 781.6 eV, assigned to Co^{3+} and Co^{2+} species, respectively, along with a satellite peak at 786.6 eV characteristic of Co^{2+} ions.

Finally, quantitative analysis of the Ni 3p and Co 3p regions revealed a deviation of the surface Ni/Co ratio from the bulk composition determined by EDX, indicating a slight surface enrichment in nickel. This combination of a defect-rich sulfide surface and mixed oxidation states creates abundant active centers, which can promote enhanced electrocatalytic activity.